Studies of Metal Poor T Dwarfs in UKIDSS

David Murray
University of Hertfordshire

A thesis submitted in partial fulfillment of the requirements of the

University of Hertfordshire

for the degree of Doctor of Philosophy

December 2012

Studies of Metal Poor T Dwarfs in UKIDSS

David Murray
December 2012

University of Hertfordshire
Submitted for the degree of Doctor of Philosophy

Abstract

I have used blue near-infrared colours to select a group of UKIDSS T dwarfs with spectral types later than T4. From amongst these I identify two kinematic halo T-dwarf candidates. Blue near-infrared colours have been attributed to collisionally-induced hydrogen absorption, which is enhanced by either high surface gravity or low metallicity. Proper motions are measured and distances estimated, allowing the determination of tangential velocities. U and V components are estimated for our objects by assuming $V_{\rm rad} = 0$. From this, ULAS J0926+0835 is found to have $U = 62$ km s^{-1} and $V = -140$ km s^{-1} and ULAS J1319+1209 is found to have $U = 192$ km s^{-1} and $V = -92$ km s^{-1}. These values are consistent with potential halo membership. However, surprisingly, these are not the bluest objects in the selection. The bluest is ULAS J1233+1219, with $J-K = -1.16 \pm 0.07$, and surprisingly this object is found to have thin disc-like U and V. Our sample also contains Hip 73786B, which I find to be a companion to the star Hip 73786. Hip 73786 is a metal-poor star, with [Fe/H]$= -0.3 \pm 0.1$ and is located at a distance of 19±0.7 pc. U, V, W space velocity components are calculated for Hip 73786A and B, finding that $U = -48 \pm 7$ km s^{-1}, $V = -75 \pm 4$ km s^{-1} and $W = -44 \pm 8$ km s^{-1}. From the properties of the primary, Hip 73786B is found to be at least 1.6 Gyr old. As a metal poor object, Hip 73786B represents an important addition to the sample of known T dwarf benchmarks.

Using mid-infrared data from WISE, I also identify T dwarfs with abnormally-red $H - W2$ and consider possible causes for their extreme colours. In particular I examine three prominent examples of this phenomenon, ULAS J1416+1348B, 2MASS J0939-2448 and BD+01^o 2920B. A plot of spectral type against M_{W2}-magnitude suggests that ULAS J1416+1348B is potentially an unresolved binary, similar to 2MASS J0939-2448. However, the plot also indicates that BD+01^o 2920B is not an unresolved binary. I also present new FIRE spectroscopy for ULAS J1416+1348B and 2MASS J0939-2448. These data show that ULAS J1416+1348B has a similar shape to the Y-band spectrum to that of BD+01^o 2920B, thus suggesting that the two objects have a similar metallicity, whereas 2MASS J0939-2448 appears to be a more metal-rich object. Using a new parallactic distance, I derive a luminosity of $(6.9\pm0.7)\times10^{20}$ W for ULAS J1416+1348B. I also find a radial velocity of -39 ± 1 kms^{-1} for this object. The agreement between this and that of the L dwarf SDSS J1416+1348A confirms that these two objects are physically-associated. I also present a set of simulated unresolved binaries; the colours of these systems do not appear to redden significantly with the addition of cooler companions. From this, I suggest that the colours of ULAS J1416+1348B and BD+01^o 2920B cannot be solely attributed to any possible unresolved companions; for these two objects, composition and/or surface gravity must be playing a substantial role. Consideration of model predictions provides extra evidence for this argument, showing as it does that high $\log g$ and low metallicity can redden $H - W2$ colours by as much as $\sim$0.5 mag as compared to a high-metallicity and low $\log g$ object of the same effective temperature.

I also present kinematics and photometry for several more new candidate low-metallicity T dwarfs. Spectra are also presented, where available. In addition I provide new follow-up JHK spectroscopy for ULAS J0926+0835, ULAS J1233+1219 and ULAS J1319+1209. These new spectra allow full JHK-based spectral typing for these objects.

CONTENTS

LIST OF FIGURES

LIST OF TABLES

Acknowledgements

I would very much like to thank all of the many people who helped me in various ways with this work; I'd dearly like to list you all individually, but that would probably constitute a second thesis all by itself. So regrettably, I'll have to adopt this awkward cop-out instead!

That said, I would like to acknowledge a few people specifically.

First of all, I would like to thank my supervisors Hugh Jones and David Pinfield for their many efforts and advice over the past few years.

I would like to thank my office mates, past and present, for their support and friendship. STARLINK might be gone, but it hasn't been forgotten! I'd also like to particularly thank the new office for letting me get away with taking the window seat!

I'd like to thank John Atkinson for much help with various computer issues I've had over the last few years, some of which were embarrassingly self-inflicted.

I would never have been able to start any of this in the first place my grandfather, Maurice Lockwood, whose support made all of this possible to begin with.

I also wish to thank my parents, Judith and Louis Murray, for listening to me and supporting me through the highs and lows of the last few years.

My friend Daniel Pointon deserves a mention, for listening sympathetically and offering much sensible advice.

I'd also like to thank the LJ and DW crowds - your consideration and patient listening has been invaluable, and has helped me enormously.

Thank you to you all!

Chapter 1

Introduction

1.1 Motivation and Thesis Structure

The aim of this work is to uncover candidate metal-poor T dwarfs; these objects are of particular interest as it is from this group which one would expect to select galactic halo T dwarfs. In addition, I seek to use the observed properties of these objects to shed light on the likely properties of halo T dwarfs.

With these aims in mind, my thesis is split into the following sections:

Chapter 1, the Introduction, covers an introduction to T dwarfs, the galactic halo and observations of brown dwarfs in mid-infrared. It describes the stellar populations found in our galaxy, the structures and atmospheres of brown dwarfs and the formation mechanisms described in the literature.

Chapter 2, drawn from my 2011 paper, describes my initial search for metal-poor T dwarfs, the discoveries made as part of that search, and the kinematic and photometric properties of the objects in question. I also present spectra and conduct spectral typing for these objects.

Chapter 3, based on my 2012/13 draft paper, describes my studies of three T dwarfs with unusual mid-infrared colours. I investigate what role, if any, that composition and/or surface gravity may be having in these colours. (Halo stars have low metallicities, and thus by analogy it is expected that halo T dwarfs to have colours strongly-impacted by

Table 1.1: A summary of galactic populations.

Component	$\sigma_U/\mathrm{kms}^{-1}$	$\sigma_V/\mathrm{kms}^{-1}$	$\sigma_W/\mathrm{kms}^{-1}$	Scale height/pc
Thin disc	35	56	22	∼300
Thick disc	56	45	50	∼1000
Halo	141	106	94	∼3000

The U and V dispersions for the thin and thick discs are from the 3σ-limits given in Pauli *et al.* (2006); the halo UVW dispersions are from Chiba and Beers (2000). The W dispersions for the thin and thick discs are also from Haywood *et al.* (2013). The trend is clear; older populations have higher velocity dispersions and greater scale heights. The scale heights are from Jurić *et al.* (2008).

this. Studying analogous disc objects may shed light on what trends should be expected.)

Chapter 4 concerns my continuing search for new candidate-objects and also spectroscopic follow-up of several of my existing candidates.

Chapter 5, the Conclusions, summarises my findings.

Chapter 6 gives a list of both my published work and also the other papers in the literature to which this study has contributed.

1.2 Galactic Populations

The contents of the Milky Way can be sub-divided into several distinct populations. Stars can be divided up according to their kinematics and chemical structure. In particular, three overall groups have been identified; these are the Bulge, the galactic disk and the halo. The disk can further be subdivided into the thin and thick disks. In the following sections, the properties of the thin disc, the thick disc and the stellar halo will be described in turn.

The kinematic properties of the halo, thick and thin discs are also summarised in Table 1.1.

1.2.1 Thin disc

The thin disc is the current site of active star formation within the galaxy. Thin disc stars are concentrated closely around the mean galactic plane. The scale height of thin disc stars varies somewhat with spectral type, as cooler, smaller stars live much longer than short-lived OB stars, and consequently have more time in which to disperse away from their original star-forming regions.

Pauli *et al.* (2006) use a sample compiled from the spectroscopic investigations of Edvardsson *et al.* (1993), Fuhrmann (1998) and Fuhrmann (2004). Based on this sample, they report characteristics of the thin disc such that the mean velocities are $< U_{\rm ms} >=$ $3\,{\rm km\,s^{-1}}$ and $< V_{\rm ms} >=$ 215 $\rm km\,s^{-1}$, with dispersions of σ_U = 35 $\rm km\,s^{-1}$ and σ_V =56 $\rm km\,s^{-1}$.

The thin disc is the youngest component of the galaxy. del Peloso *et al.* (2005) measured the abundance ratios of [Th/Eu] for 20 giants and subdwarfs with spectral types of F5 to G5, and compared these to a model of galactic evolution and to stellar abundance data. From these, they dervied an estimated age of 8.3±1.8 Gyr. It should be noted that many objects within the thin disc are substantially younger than this age, as the thin disc is still active forming stars.

The thin disc averages the highest metallicity of the galaxy's components. Based on a sample of long-lived stars in the solar neighborhood, Pauli *et al.* (2006) find a range of $-0.4 <$[Fe/H]≤ 0.1, with a median that matches the solar abundances (Haywood 2001). The metallicity of the thin disc is higher than the other components as the thin disc is experiencing continued enrichment of its ISM by supernovae and red giants.

The thin disc has a scale height of $z \sim 100$ pc for OBAF stars and up to ~ 350 pc for later-type stars.

The existence of the galactic disc is a consequence of the Milky Way's formation from a collapsing, rotating gas cloud. This process will have tended to destroy motion that was oriented perpendicular to the direction of rotation, but preserve motion that was parallel to it. Consequently as the cloud collapsed, it tended to collapse into a disc-shaped structure.

1.2.2 Thick disc

The thick disc's existence was initially-identified by Gilmore and Reid (1983), who noted the presence of a change in slope of the vertical density distribution of disc stars at $z \sim 1.4$ kpc above the plane.

Thick disc stars are noted for having greater velocity dispersions and also lower mean velocities. Pauli *et al.* (2006) find $< U_{\rm ms} >= -32$ $\rm km\,s^{-1}$ (the negative value is an effect of the galactic bulge; see Fuhrmann 2004) , $< V_{\mathrm{ms}} >$=160 $\mathrm{km\,s^{-1}}$ and dispersions such that σ_U =56 $\mathrm{km\,s^{-1}}$ and σ_V = 45 $\mathrm{km\,s^{-1}}$.

As well as being distinct kinematically, thick disc stars also show differences in chemical composition to those of the thin disc.

Alpha elements are elements synthesized by alpha-particle capture, prior to the onset of silicon burning. The stars this process occurs in are stellar precursors to Type II supernovae (silicon fusion in turn produces iron as a byproduct, and iron fusion results in core collapse). Examples of alpha elements include oxygen, neon, magnesium, silicon, sulphur, argon, calcium and titanium. Stars in the thick disc show an enhancement of magnesium relative to iron ([Mg/Fe]) when compared to thin disc stars (strictly, this actually means that they contain rather less iron than thin disc stars, hence the apparent enhancement). This implies that star formation in the thick disc was heavily influed by Type II supernovae, whereas enrichment of the ISM for the thin disc has been dominated by Type I supernovae. For thick disc stars, Fuhrmann (1998) found a typical enhancement of 0.4 dex relative to the thin disc.

The thick disc has a lower average metallicity than the thin disc; Pauli *et al.* (2006) find a range of $-1.05 <$[Fe/H]< -0.3.

The thick disc may be an artifact of a major galactic merger event around 11 billion years ago (Robin *et al.* 1996). A major merger event would have been followed by a burst of star formation, which may have in turn blown out much of the remaining gas. This would then have ended star formation inside the thick disc, as well as puffing it up to its $\sim$ 1 kpc scale height. Star formation in the Milky Way would likely only have resumed once the thin disc re-formed. This model can also account for the thick disc's alpha-enrichment; by the time Type Ia supernovae could start to significantly-enrich the ISM with iron, star formation in the thick disk had already ended.

Based on evidence from stellar chemical abundances, Mashonkina and Gehren (2001) estimate that star formation within the thick disc occurred for a duration of less than 1 Gyr.

1.2.3 Halo

The halo is the oldest component-population of the galaxy, its formation having begun with the initial collapse of the protogalaxy. Estimates for its age suggest an age greater than 11 Gyr (Bensby *et al.* 2003). The bulk of star formation within the halo appears to have occurred in a single 1-2 Gyr burst. There is no evidence for ongoing star formation within the halo.

Halo stars possess orbits which attain high galactic latitudes. These orbits are often strongly-inclined relative to the plane of the galactic disc, and frequently are retrograde. The halo as a whole does not appear to exhibit much if any net rotation. This has a consequence for the position of the halo region on V, U plots. The Local Standard of Rest (LSR) is defined as the average motion of stars in the solar neighborhood. The vast majority of these stars belong to the thin disc, consequently 'zero velocity' with respect to the LSR is actually a velocity centred around 220 $\mathrm{km\,s^{-1}}$ (Carroll and Ostlie 1996) with respect to the galaxy's centre of mass. As the halo has no net rotation relative to the galaxy as a whole, its stars therefore appear to lag behind those of the disc in the VU plot. This axisymmetric drift is of around 220 $\mathrm{km\,s^{-1}}$ in magnitude, exactly as one would expect given the disc's rotation.

In terms of composition, the halo has the lowest metallicity of all three populations, with [Fe/H] < -1.05 (Pauli *et al.* 2006). Metallicities are often much lower than this. An extreme example of this is HE 1327-2326, which has [Fe/H]≤ -5.0 (Frebel *et al.* 2008). These low metallicities are consistent with the halo's great age; the original gas from which it formed had not experienced much enrichment by supernovae or red giants prior to the onset of halo star formation. As the burst of star formation within the halo was comparatively-brief, resulting in a metal-poor and α-enhanced population of stars.

1.2.4 Dark matter

It has been known for some time that the rotation curves of many galaxies are not Keplerian (Rubin *et al.* 1978); rather than falling off radially as one would expect from an R^{-2} law, instead stellar velocities remain largely flat all the way to the edges of the observable discs. This also appears to be true for our own galaxy as well as others. One suggestion that could account for this phenomenon would be non-luminous matter distributed in a near-spherical structure around the galactic disc; (Ostriker and Peebles 1973) call this the 'heavy-halo'. As this hypothetical dark matter is non-luminous, we do not observe it directly and consequently our stellar-based estimates for the masses of galaxies are too low.

In the case of the Milky Way, (Alcock *et al.* 2000) estimate that as little as 10% of the galaxy's mass is in the form of stars, gas and dust within the disc, bulge and halo.

Various ideas have been advanced for the composition of the remaining nine tenths. These range from relatively-mundane suggestions such as clouds of cold molecular gas and faint, evolved white dwarfs to a veritable zoo of proposed exotic particles. As of the time of writing, direct detection of dark matter has proved elusive. Some theorists have even proposed that there is actually no such thing as dark matter, and that the apparent non-Keplerian behaviour of galactic discs is in fact down to gravity being stronger than expected at large distances. (These so-called 'MOND' - Modified Newtonian Dynamics - theories in turn run into trouble due to the absence of a clear candidate for a relativistic MOND and also their inconsistency with observational results such as those for the Bullet Cluster; see Markevitch *et al.* 2004).

The Alpha Magnetic Spectrometer (AMS; see Aguilar *et al.* 2013) experiment onboard the International Space Station, and particle physics-based efforts at facilities such as CERN, may provide some clarity as to the identity of the missing mass over the next few years. Given previous negative results, though, the possibility also exists that they may not supply the scientific and wider communities with much more clarity than is currently enjoyed.

Although the composition and nature of dark matter itself remains something of a mystery, there are several possibilities that have been largely eliminated. At one point brown dwarfs were suggested as a candidate for dark matter (such as Tarter 1975; Bahcall 1984). Subsequent searches for so-called 'Massive Compact Halo Objects' (MACHOs) have not revealed anything like enough possible candidates to account for the sheer mass of the Milky Way's dark matter halo (Reid *et al.* 2002). Recent results from the Widefield Infrared Survey Explorer satellite (WISE) support this; whilst still incomplete, particularly at very low $T_{\rm eff}$s, nonetheless the WISE results demonstrate that brown dwarfs are far rarer than stars. The estimated ratio is around 6:1 in the stars' favour (Kirkpatrick *et al.* 2011). Given that brown dwarfs are expected to be less massive than even the smallest red dwarfs, this leaves little room for the brown dwarfs to account for more than a tiny fraction of the galaxy's associated dark matter!

1.2.5 The Besançon galaxy

The Besançon models (see for instance Robin *et al.* 2003, 2004) is an attempt to reproduce the stellar content of the galaxy. It does so by assuming that the stars belong to one of four populations, the thin disc, the thick disc, the bulge and the halo. The modeling of each population is based on a set of evolutionary tracks and assumptions on density distributions. These are constrained either through dynamical considerations or by observational data.

In the solar neighborhood, the Besançon model suggests a stellar density of around $\sim$0.1 stars per cubic parsec for the thin disc population, 2.83×10^{-3} stars/pc^3 for the thick disc and 8.19×10^{-5} stars/pc^3 for the stellar halo. In percentage terms, thick disc stars account for $\sim$ 2.07% of the thin disc tally and halo stars account for 0.06%.

The Brown Dwarf Archive[1], maintained by J. Davy Kirkpatrick and Adam Burgasser, has been maintaining a census of total numbers of discovered brown dwarfs. As of the most recent update (November 2012), this census stands at 1281 objects of spectral types L, T and Y. If we were to (rather naively) assume that this census splits according to the percentages above, then we would have an expectation value of $\sim$1254 thin disc brown dwarfs, $\sim$27 thick disc brown dwarfs and $\sim$1 halo brown dwarf. (The numbers have been rounded to one significant figure, hence adding up to 1282 rather than 1281.)

1.2.6 The substellar population

The initial mass function (hereafter, IMF) is defined as the total number of stars created per unit mass (Miller and Scalo 1979) in star formation events. The IMF is a quantity that describes the star formation process and accounts for its results, and is consequently of great importance for studies of the galaxy's stellar content and the distribution of those stars. Salpeter (1955) found that the IMF in the solar neighborhood follows a power law of form M^α with an exponent of ~ -2.35. This result still stands today for stars with masses $\sim$0.5 to a few solar masses.

Brown dwarfs constitute the low-mass extension of the stellar population. They are notable in that they lack a sufficient mass to sustain nuclear fusion in their cores, and thus they cannot stabilize onto the Main Sequence. A straightforward extrapolation of the Salpeter IMF leads to around twice as much mass present in the form of brown dwarfs than in the form of stars, which suggests that they should be quite numerous. However, the stellar number counts for M dwarfs show a tendency to flatten out at around 0.3-0.5 solar masses (Sandage 1957; Schmidt 1959; Miller and Scalo 1979).

For masses below $0.5\,\mathrm{M_{Sun}}$ (Kroupa *et al.* 1990, 1993) find an IMF with $\alpha \sim 1.3$, thus indicating that in this regime, the IMF does indeed flatten somewhat. Their method involved comparing dwarf stars within 5.2 pc of the Sun to a smoothed version of the

---

[1] See http://spider.ipac.caltech.edu/staff/davy/ARCHIVE/index.shtml

luminosity function of Wielen *et al.* (1983); it is possible that some of the flattening may be due to any incompletenesses in this luminosity function. However, the existence of at least a degree of flattening at low masses does seem clear.

Measuring the IMF for brown dwarfs includes additional difficulties compared to that for stars. These include uncertainties in what luminosity function to adopt, the lack of data in some wavelengths and the presence of biases in sky surveys. (It is easier for surveys to identify relatively-bright brown dwarfs, which means that surveys are better at finding earlier spectral types, and thus will systematically identify more of them.) Consequently any work that seeks to measure the brown dwarf IMF has to be regarded as somewhat-provisional. However, there have been some attempts. As one example, Reid *et al.* (1999) conducted an analysis of surface densities of L dwarfs as seen in 2MASS. They concluded that the observations were broadly consistent with an IMF such that $1.0 < \alpha < 1.5$, which seems consistent with the results for M dwarfs.

If this trend for the IMF flatenning does indeed continue into the substellar regime, then one would expect to see rather less total mass in the form of brown dwarfs than there is as stars. There has consequently been considerable interest in the brown dwarf mass function, and efforts have been made to simulate it.

Burgasser (2004) conducted a series of MonteCarlo simulations of the substellar mass function, based on the COND and Burrows evolutionary model sets. It was found that the distributions tended to have fewer objects in the L-type temperature regime and more objects in the cooler T-type classification. This was ascribed to the relatively-higher speed with which brown dwarfs evolve through the L classification. L dwarfs have higher temperatures, and consequently as $L \propto T^4$, much higher luminosities than T dwarfs. Consequently L dwarfs emit their store of heat at a much faster rate.

Burgasser (2004) found that their substellar luminosity function did not depend sensitively on the choices of galactic birth rate, substellar evolutionary models and age- and mass-ranges. However, there was one notable exception. Halo-type objects (those in the simulations with assumed ages greater than 9 Gyr) were found to show a substantial depletion in objects with temperatures between 1200 and 2000 K. Thus, the simulations predict that the halo brown dwarf population should be strongly-biased toward the T- and later-typed objects at the expense of the Ls.

Allen *et al.* (2005) sought to constrain the substellar mass function through Bayesian inference. They adopted a wide range of assumptions regarding the rate of star formation in the Milky Way. As with Burgasser (2004), Allen et al. found that these parameters seemed to have little effect on the resulting substellar distributions. They also computed age distributions for objects of spectral classes M, L and T. They found that L dwarfs were systemically younger than the other objects, with an average age of 3 Gyr. In particular, later-type L dwarfs tended to be younger than any other group; this is because the proportion of hydrogen-burning stars declines to nothing through the L spectral sequence. As some early-L dwarfs will in fact be very low-mass stars, these objects will stabilize onto the Main Sequence and thus remain in their spectral type for extended periods of time. Later-type L dwarfs, objects too low-mass to be stars, do not have this option.

For T dwarfs, Allen *et al.* (2005) found that the constant birth rate of brown dwarfs in general and the slower cooling rate of objects in the T-type temperature range meant that the T dwarfs have an approximately constant space density as a function of age.

More recently, Day-Jones *et al.* (2013) compared various substellar birth rates to a large sample of brown dwarfs selected from near-infrared surveys. On the basis of this, they were able to definitively rule out a halo-like birth rate for all brown dwarfs, demonstrating that the majority of observed objects must belong to the disc populations.

1.3 Structure of brown dwarfs

Unlike normal stars, the evolution of brown dwarfs is not dominated by hydrogen fusion (Burrows *et al.* 2001). Instead, brown dwarfs shine through residual heat left over from their formation. This in turn influences their structure and evolution. In this section we will consider brown dwarf structure.

1.3.1 Brown dwarf mass and its observability

In most cases, the mass of a field brown dwarf is not directly-observable. The quantity that is directly-measured, through spectral type and luminosity, is an object's effective temperature. As effective temperature is related to both age and mass, a wide range of differing objects may exhibit the same temperature. (An old but high-mass object can show the same temperature as a young but lower-mass object.) However, it stands to reason that we would expect the observable halo and thick disc populations to be dominated by higher-mass brown dwarfs, as these objects will have retained enough internal heat to still be reasonably-bright even now, ∼10 Gyr after their formation. It also follows logically that the highest-mass objects will be the halo and thick disc L dwarfs.

The existence of brown dwarfs was first predicted by Kumar (1963), who noted that there is a minimum mass limit on hydrogen burning in stars. This is imposed by the pressures and temperatures within an object's core; below a certain mass-level, they simply are not high enough for hydrogen fusion to occur.

Normal stars are supported by thermal pressure, the heat for which is supplied by the nuclear reactions in their cores. This outward pressure holds them up against the inward pull of their own gravity.

Brown dwarfs are instead supported against collapse by electron degeneracy pressure. Electrons follow Fermi statistics, and consequently no two electrons can have the same set of quantum numbers. This effectively creates a floor on how densely they can be packed, as compressing them any further would require duplication of quantum numbers (Reid and Hawley 2005). This also has the implication that mature brown dwarfs are all expected to be roughly the same size, around a Jupiter radius or so, with a $\sim 30\%$ range around that median (Burrows *et al.* 2001).

1.3.2 Convection, deuterium and lithium

Hot stars have differentiated interiors, with nuclear fusion taking place within the star's core. Above this is the radiative zone, in which energy is transported through radiation rather than conduction or convection. In stars like the Sun, the opacity becomes high enough in the envelope to inhibit the transport of energy by radiation (above 0.71 $\mathrm{R_{Sun}}$ for the Sun). From this point, energy is transported through convection of hot gas; this region is the convective zone. The top of the convective zone represents the photosphere.

This model is not true for very low mass stars and brown dwarfs. Limber (1958) showed that stars of spectral type M4 and later are convective all the way through. Consequently these stars have access to their entire supply of hydrogen, as opposed to merely the volume available in the core.

Low-mass stars have to collapse to smaller radii than higher-mass ones to reach the critical temperature for ignition of hydrogen fusion. However, as the core contracts, electron degeneracy begins to supply an extra source of pressure. Eventually, this pressure will be sufficient to stabilize the object without any input from heat from fusion. This is why brown dwarfs cannot contract far enough to initialize hydrogen fusion; electron degeneracy will stabilize their radii at $\sim$0.1 $\mathrm{R_{Sun}}$.

A subtlety is introduced into this picture by deuterium. For objects with masses greater than 0.012 M_{Sun}, the objects will experience a period during which they burn deuterium, thus bringing their luminosity evolution to a standstill for this time. This period is fairly short, lasting perhaps a hundred thousand years to a few million years (Grossman 1970). Due to its short duration, the deuterium-burning period does not have a very significant effect on subsequent brown dwarf evolution.

As low-mass stars are fully-convective, they have access to all of their nuclear fuel. Lithium fuses at a temperature of 2.5×10^6 K, lower than that for hydrogen. Consequently, if a fully-convective object is observed to retain its lithium, then it follows logically that hydrogen burning can not be occurring either. This is the so-called 'lithium test', which can be used to establish observationally whether or not an object is substellar. This technique was first used successfully by Basri *et al.* (1996) to establish the substellar nature of PPL 15. (In practice this test is difficult to apply to T dwarfs, as features such as the 670.8 nm lithium line occur in regions of the spectrum where the T dwarf supplies very little flux; see for instance Burgasser *et al.* 2006a)

A further subtlety must briefly be noted. Stars that are too hot to be fully-convective can also show lithium features in their spectra; in this case this is because the lithium is present in the outer envelope, where it is not being burnt away in nuclear reactions. The presence of lithium in these objects's spectra does not imply that they are of substellar mass.

1.3.3 Equation of state

Stellar structure rests on four fundamental equations (see for instance Chandrasekhar 1939; Schwarzschild 1958). The equation of continuity of mass describes the distribution of mass within a spherical body:

$$\frac{dM(r)}{dr} = 4\pi r^2 \rho(r) \tag{1.1}$$

in which $M(r)$ is the mass distribution and $\rho(r)$ is the density distribution.

The equation of hydrostatic equilibrium describes the balance between the inward force of the object's weight due to its self-gravitation and the outward force supplied by its internal pressure support:

$$\frac{dP(r)}{dr} = -\frac{GM(r)}{r^2}\rho(r) = -g(r)\rho(r) \tag{1.2}$$

where $P(r)$ is the pressure distribution and $g(r)$ is the gravitational acceleration.

The equation of thermal equilibrium describes the balance between energy production and energy emission from the object:

$$\frac{dL(r)}{dr} = 4\pi r^2 \rho(r)\varepsilon(r) \tag{1.3}$$

where in this case $L(r)$ is the luminosity and $\varepsilon(r)$ represents the rate at which the object generates energy.

The fourth equation describes the distribution of temperature throughout the object, as a function of radius. This means that it is related to the mode of energy transport through the object, whether radiative or convective. Consequently it has two different forms. The radiative transport form is:

$$\frac{dT(r)}{dr} = \frac{-3}{4ac}\frac{\kappa}{T^3}F(r) \tag{1.4}$$

where a is the radiation constant, c is the speed of light, κ is the opacity and $F(r)$ is the flux as a function of radius. The convective transport form is:

$$\frac{dT(r)}{dr} = \left(1 - \frac{1}{\gamma}\right)\frac{T}{P}\frac{dP}{dr} \tag{1.5}$$

where γ represents the ratio of specific heats across the convection region.

To model a stellar interior, as well as these four underlying equations, relations are needed to define three further parameters. These are pressure, energy generation and opacity (Reid and Hawley 2005). The first of these, the equation of state, describes the pressure within the object. It takes the components:

$P = P(T, \rho, composition)$

The equation of energy generation takes the form

$\varepsilon = \varepsilon(T, \rho, composition)$

and lastly, the opacity equation takes the form,

$\kappa = \kappa(T, \rho, composition)$

In the specific case of fully-convective low-mass dwarfs, Burrows and Liebert (1993) find that the equation of state takes the specific form that:

$$P_c \sim 0.77\frac{GM^2}{R} \propto M^{10/3} \tag{1.6}$$

where P_c represents the central pressure and M and R represent the mass and radius respectively.

1.3.4 Cooling and luminosity

Figure 1.1 shows the theoretical cooling tracks for a range of objects of different masses, ranging from 0.3 to 211 M_J, as shown in Burrows *et al.* (2001). Stars are shown in blue, brown dwarfs between 13 and 79 M_J are shown in green. Objects with masses below the deuterium-burning limit are shown in red. The stellar tracks eventually flatten out as the objects stabilize onto the Main Sequence after the onset of nuclear burning.

Deuterium-burning brown dwarfs enjoy a slowdown in their cooling, but this period is short. As can be seen, they quickly resume the cooling behaviour shared by non-fusing brown dwarfs once the deuterium is exhausted.

Brown dwarfs as a whole have shine through the residual heat from their formation, and consequently cool and fade as this heat is radiated away. This tendency can be seen clearly in the figure.

Higher-mass brown dwarfs start with a larger supply of residual heat, and consequently will take a longer time to evolve to the same temperature as a lower-mass object. Consequently, for a given surface temperature, it is expected that a higher-mass object will be older than a lower-mass object. From this fact, it is expected that each spectral type bin for halo brown dwarfs will be systematically older than that for thin-disc brown dwarfs.

1.3.5 Masses and gravity

The work of Bate (2005), which consists of simulations of star and brown dwarf formation, suggests that brown dwarfs do not form below masses of $\sim$9 M_J in low-metallicity environments. (This will be returned to in Section 1.5, which is on brown dwarf formation.) If we make the working assumption that this is an accurate prediction for the brown dwarf mass distribution, then it may place some limits on the halo surface gravity ranges.

The COND models (Baraffe *et al.* 2003) present calculated brown dwarf properties for a range of masses and a range of ages. The model grid includes ages of 10 Gyr, 5 Gyr, 1 Gyr and shorter intervals from 5 to 500 million years. The 10 Gyr age range is certainly younger than the estimated ages for the halo, however it does allow a limiting case. For an object with M= 0.009 solar masses (9 $M_J = 0.00858\ M_{\mathrm{Sun}}$), they find a surface gravity of $\log g = 4.393$. The highest gravity is found for a 0.075 M_{Sun} object, for which $\log g = 5.415$ is found. Consequently, it is not predicted that the surface gravity for a halo brown dwarf

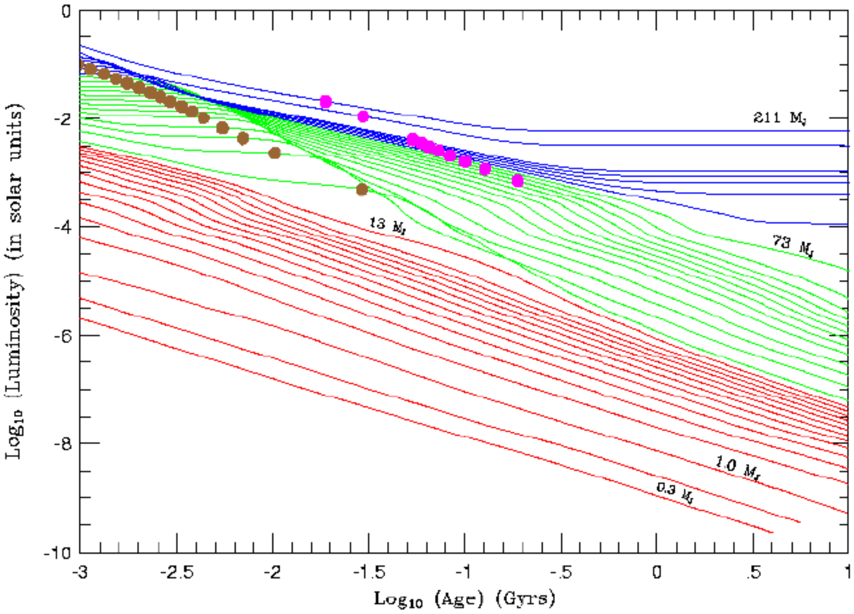

Figure 1.1: A plot showing the evolution of luminosity with age, for brown dwarfs and low mass stars; this plot appears as Figure 1 in (Burrows *et al.* 2001). The stellar tracks are shown in blue, the brown dwarfs above the deuterium-burning limit in green and the objects of lower masses in red.

will be less than ∼5.42.

By contrast, objects of 1.0 Gyr in age and the same mas range have gravities of 4.331 to 5.334. Consequently, although halo objects are expected to generally be higher-gravity, for most of the likely range they may in fact overlap with disc objects.

The highest surface gravity predicted by the COND models is for a $T_{\rm eff} = 1300\,K$ object with an age of 10 Gyr (the numerical value of its gravity is 5.503). The effective temperature of this object is within the L-T transition area, suggesting it would have a spectral type of somewhere between L8 to T2. Consequently, theory predicts that we would expect to observe the maximum gravities amongst L-T transition objects in the halo.

1.4 Atmospheres of brown dwarfs

1.4.1 Spectral types of brown dwarfs

Brown dwarfs appear in four spectral classes, M, L, T and Y. M-type brown dwarfs are the youngest and hottest, and overlap in their observed properties with normal red dwarfs. L-type brown dwarfs are cooler and fainter, although some earlier-L objects are still actual, hydrogen-burning stars. Everything in types T and Y is substellar in mass. The properties of each type will be summarised in turn.

M-type brown dwarfs have relatively-hot effective temperatures, with $T_{\rm eff} \sim 3000\,K$ to 2200 K. Their spectra show significant absorption from metal oxides such as TiO and VO, just as normal red dwarfs do. Also, metal hydride features such as MgH and FeH start to become observable at late-M.

L-type brown dwarfs occupy a cooler range of temperatures, from 2200 K to 1400 K. Across the M to L transition, TiO absorption weakens and then largely fades. VO is observable in types L0 and L1, but in the L2 dwarf Kelu 1 it is almost undetectable and it is not seen in later-type objects. Rather than oxide lines, the dominant absorbers in L-dwarf atmospheres are metal hydrides such as CaH, FeH, CrH and also MgH. The reason for the disappearance of TiO and VO features is that these absorbers are forming into condensate dust clouds within the L dwarf's atmosphere. L dwarf spectra peak in the near-infrared rather than the optical and they start to show distinctly non-blackbody shapes, particularly toward the end of the L regime. Due to their coolness relative to actual stars, L dwarfs have very red near-infrared and optical colours.

The T spectral type constitutes objects with effective temperatures below 1400 K. At these levels, almost all of the object's flux is now in the near-infrared. Across the L to T transition, the condensate clouds drop below the objects' photospheres. T dwarf spectra are dominated by molecular features, in particular CH_4 and H_2O; these are in fact used as the basis of T dwarf spectral classification (Burgasser *et al.* 2006b). Only in T dwarfs are temperatures attained that are low enough to support such relatively-large and relatively-fragile molecules (methane in particular is not stable above 1400 K). The absorption features created by these molecules are significant in size, and also have the effect of redistributing some flux bluewards. Consequently, T dwarfs' SEDs look nothing like blackbodies; rather they have a characteristic shape that can be described as 'three spikes and a bump'. The truncation of the K-band peak - the 'bump' at the end of the sequence - is partly down to collisionally-induced hydrogen absorption.

Lastly, a recent development is the beginnings of the characterization of the Y spectral type. These very cold objects lie beyond the end of the T regime, with temperatures below 500 K. These objects have spectra that are beginning to be influenced by ammonia absorption. Their flux peaks are probably in the mid-infrared rather than the near. However, classification has so far been somewhat limited by small-number statistics and the limited distribution of objects currently available, as well as faint magnitudes and poor signal-to-noise ratios in observed spectra (Kirkpatrick *et al.* 2012). The full characterization of spectral class Y will likely occur over the next few years, possibly assisted by new instruments such as E-ELT.

1.4.2 Collisionally-induced hydrogen absorption

Collisionally-induced hydrogen absorption (Hereafter, CIA H_2) was first described by Linsky (1969). The effects of this source of absorption were further quantified for the context of cool, zero-metallicity stellar atmospheres by (Saumon *et al.* 1994). Borysow *et al.* (1997) considered the effect of CIA H_2 on stellar spectra, and found that it is a significant source of absorption up to temperatures as high as 4000 K, and metallicities as high as 0.1 Z_{Solar}.

The hydrogen molecule possesses no intrinsic dipole moment. However, a collision between hydrogen molecules can induce a dipole moment between the colliding partners. This allows the rotational and vibrational transitions associated with the dipole moment, thus in turn allowing for this collisional absorption of photons. The absorption will be stronger in environments where more collisions occur; raising the pressure of hydrogen will increase the amount of observed CIA H_2. (The opacity is proportional to the square of the partial pressure of molecular hydrogen; see Linsky 1969)

Consequently, if one object has a higher surface gravity than another, the higher-gravity object will display more CIA H_2 due to the increased pressure in its atmosphere.

Pressures can also vary for constant gravity, if the metallicity is different between objects. A reduction in metallicity means a reduction of the availability of metals in the stellar atmosphere, and thus of the metal-based opacity. This will enhance the H_2-H_2 absorption (Borysow *et al.* 1997).

The effects of CIA H_2 are felt between wavelengths of 1 and 10 μm; it is particularly strong around 2μm (see Mould and Hyland 1976; Leggett *et al.* 2000). In the case of the T dwarfs, this corresponds to the K-band region, leading to the characteristic 'bump' shape seen for that peak.

1.4.3 Metallicity and gravity - the impact on atmospheres

This section will consider the effect of metallicity on infrared spectra. This will be done using the Burrows *et al.* (2006) and Allard and Freytag (2010) BTSettl model sets.

Figure 1.2 shows BTSettl model spectra for a temperature of 900 K and a surface gravity of 5.0, with metallicities ranging from $[m/H]= -0.3$ to $+0.5$. Figure 1.3 shows Burrows models for the same temperature and gravity, and the same metallicity range. As can be seen, the principle effects of reducing the metallicity on the overall spectral energy distribution is a depression of the K-band peak and also an increase of the left shoulder of the Y-band peak. These features are predicted by both model sets, although they seem stronger in the Burrows plots.

Figure 1.4 shows BTSettl model spectra for a temperature of 900 K and solar metallicity, with surface gravities ranging from $\log g = 4.5$ to 5.5. Figure 1.5 shows Burrows models for the same temperature and metallicity, and the same gravity range. Increasing the surface gravity also causes the K-band peak to flatten and also increases the overall height of the Y-band peak. However, the overall shape of the Y-band peak does not change much (a slight broadening is apparent in the BTSettl set, but not in the Burrows models), and certainly far less than is apparent for changes in metallicity.

The models all predict that increasing metallicity and/or decreasing surface gravity will have the effect of redistributing flux from the mid-infrared to the near-infrared. In particular, in the above scenario, an increase in metallicity will result in less flux in the

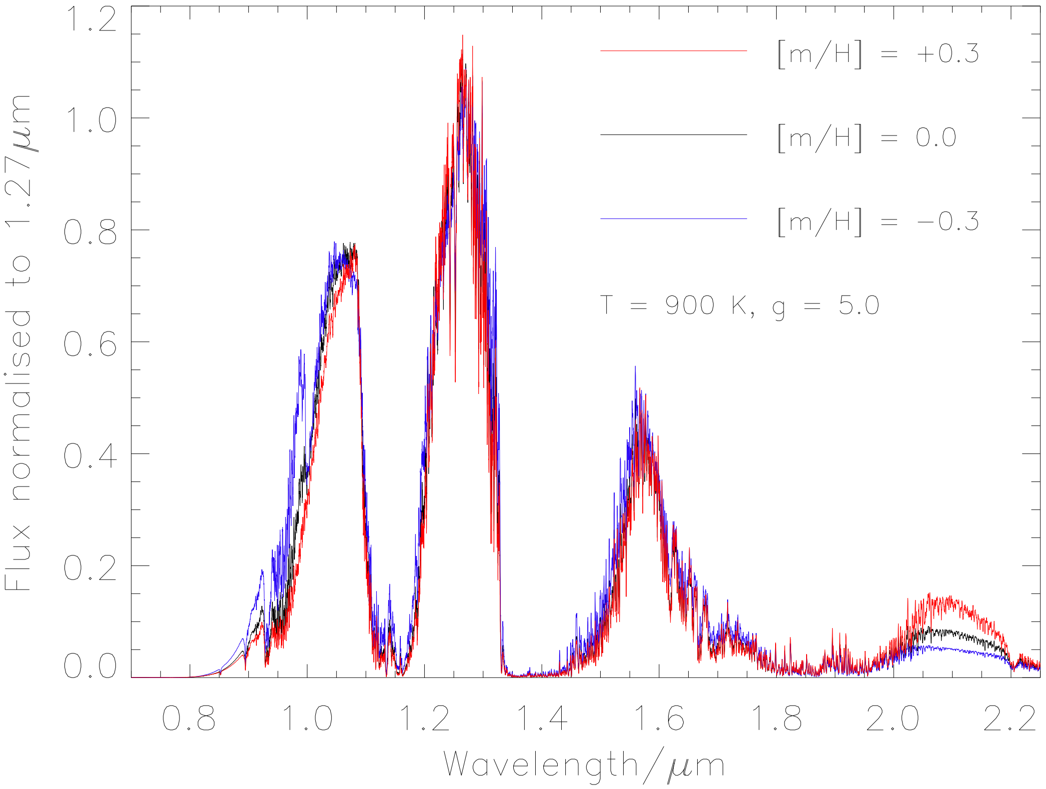

Figure 1.2: BTSettl model spectra for constant temperature and surface gravity. The metallicity range is from −0.3 (blue) to +0.3 (red). The spectra have been smoothed on a factor of 10 for clarity. The MKO Y filter covers the range 0.97-1.07 μm and the K-band filter covers the region 2.03-2.07 μm.

WISE $W2$ ~4.5 μm band and more flux in the near-infrared K-band (Leggett *et al.* 2009).

1.4.4 Dust formation and condensation

Dust formation in cool atmospheres depletes many important metals, most notably titanium. Double-metal molecules such as TiO and VO are particularly affected by dust formation, hence their depletion across the M/L transition relative to single-metal features such as the hydride lines. In L dwarfs, the removal of TiO and VO features in the optical regions of their spectra lead to enhanced features due to alkali metals such as caesium, rubidium and also lithium.

Dust formation across the M/L transition also has consequences for the near-infrared spectra of L dwarfs. The opacity of the dust grains adds continuum absorption in the infrared, trapping outgoing radiation and so leading to enhanced atmospheric temperatures.

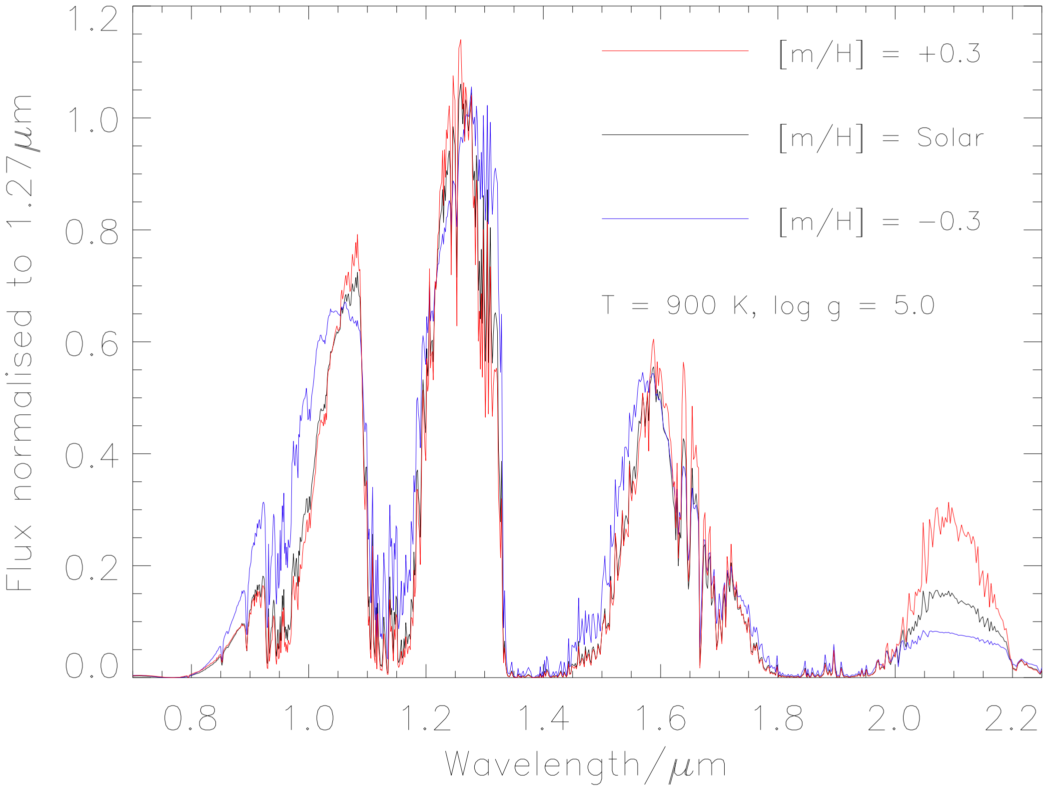

Figure 1.3: Burrows model spectra for constant temperature and surface gravity. The metallicity range is from −0.3 (blue) to +0.3(red).

This results in dissociation of H_2O, so dusty model atmospheres show weaker steam bands than others.

Fegley and Lodders (1996) and Burrows and Sharp (1999) both consider dust formation in low-temperature atmospheres. (The latter considered atmospheres containing more than one hundred different condensate species, over a temperature regime from 2200 K to 100 K.) TiO is predicted to condense into grains of perovskite ($CaTiO_3$) at a temperature of between 2300 and 2000K. Vanadium oxide is expected to transition to solid VO at temperatures between 1900 K and 1700 K. CrH is predicted to be in its metallic phase by 1400K and all of the alkali features are depleted by the formation of chlorides below 1200 K.

Lastly, carbon exists pre-dominantly in the form of CO in L dwarfs. However, between temperatures of 1500 to 1200K, carbon preferentially forms methane instead. The emergence of methane in brown dwarf spectra marks the transition between the L and T spectral types.

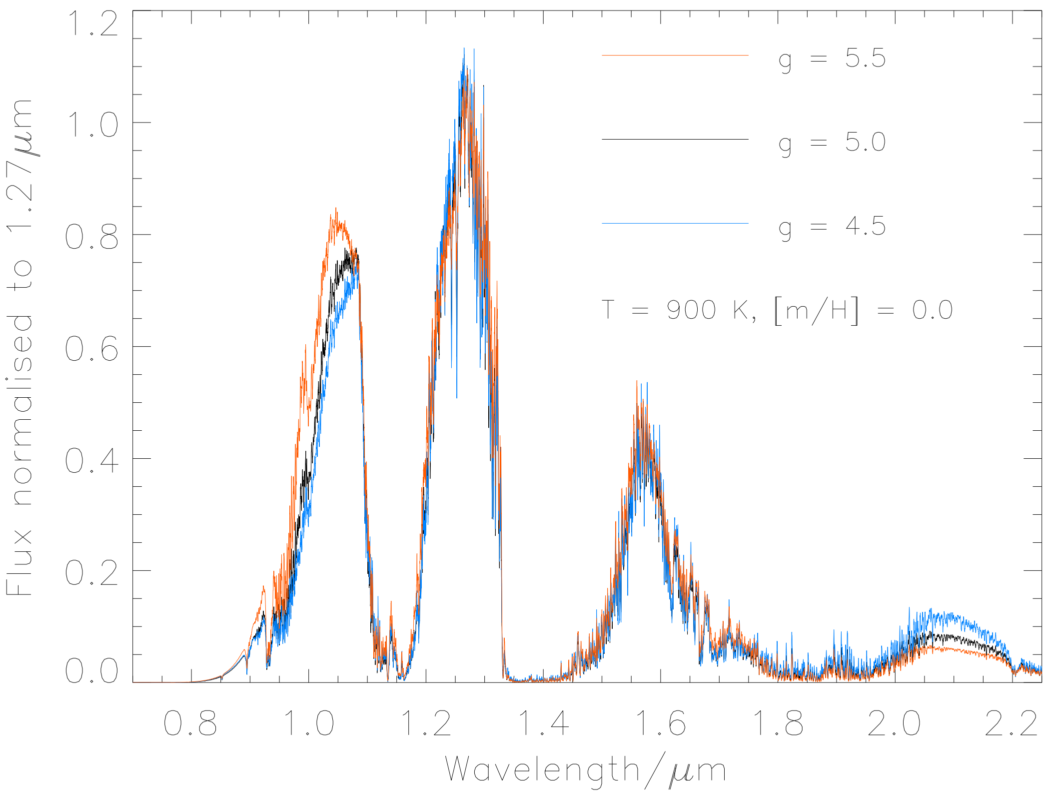

Figure 1.4: BTSettl model spectra for constant temperature and metallicity. The surface gravity range is from 4.5 (light blue) to 5.5 (orange). The spectra have been smoothed on a factor of 10 for clarity.

1.4.5 Model limitations

Several factors may affect the validity and the applicability of spectral and evolutionary models of brown dwarfs.

First of all, if dust absorption is improperly-modeled, then this may in turn result in an incorrect near-infrared continuum opacity.

However, a potentially greater limitation comes in the form of molecular absorption, particularly for late-type objects. Leggett *et al.* (2007) note that the commonly-used NH_3 and CH_4 line lists are incomplete. The ammonia line lists do not include any absorption at $\lambda \leq 1.4\,\mu$m and have gaps at $\lambda \geq 1.9\,\mu$m. The methane line list is incomplete in the H-band, which is a particular issue for T dwarfs as this is where one of their flux peaks is located.

A further, somewhat more subtle, issue is that of abundances. Most brown dwarf models assume solar abundances as the default position (this is the case for the Bur-

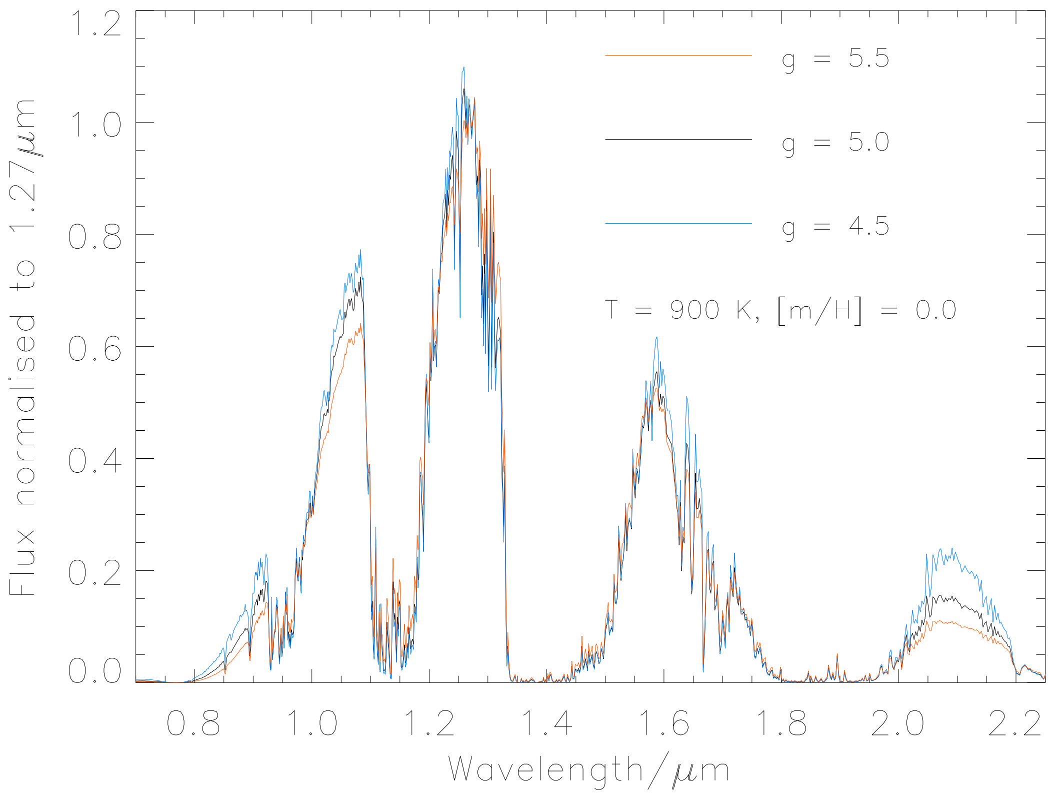

Figure 1.5: Burrows model spectra for constant temperature and metallicity. The surface gravity range is from 4.5 (light blue) to 5.5 (orange).

rows models), although it is perhaps likely that many real objects will diverge from this condition, particularly for halo and thick disc brown dwarfs.

There is a partial exception to this rule. The BTSettl models Allard *et al.* (2011) base their abundances on those of Asplund *et al.* (2009). In the BTSettl models, α-enhancement is applied for subsolar metallicity models. The [m/H]$= -0.5$ set uses [α/H]$= +0.2$; the [m/H]< -0.5 sets use [α/H]$= +0.4$. However, the brown dwarf temperature range is only modeled for $+0.5 \geq$ [m/H] ≥ -0.5, i.e. not for metal-poor halo objects.

1.5 Formation of brown dwarfs

Several possible formation mechanisms have been proposed for brown dwarfs. All of them have their advantages and their limitations. Whilst it is clear that their very existence proves that brown dwarfs definitely do form, and that this also seems to take place within star-forming regions (see for instance Aller *et al.* 2013), the exact mechanism or mechanisms remain subject to a substantial degree of debate.

The first hypothesis is that brown dwarfs form in the same manner as stars, through the collapse of molecular clouds. However, Jeans mass fragmentation would require very cold, high-density environments to be able to form the lowest-mass brown dwarfs. Such environments are very scarce amongst star-forming regions (Reid and Hawley 2005). Also, if brown dwarfs followed the formation patterns of stars, one would expect to see a similar distribution of binary parameters and frequency. However, there exists a 'brown dwarf desert'; very few such objects have been detected as close-in companions of stars, a phenomenon to which attention was initially drawn by Marcy and Butler (2000). By contrast, stars orbit each other at a wide variety of separations.

Another model is disc fragmentation (Boffin *et al.* 1998). In this scenario, interactions between nearby stars in star-forming regions and discs causes the discs to fragment into smaller chunks. These chunks are sometimes below the hydrogen-burning limit, hence forming brown dwarfs. However, Stamatellos *et al.* (2011) find that not all discs will be large enough for such gravitational fragmentation to occur; the disc needs a radius of at least 100 AU. Furthermore, they note that very few observed star-forming discs are large enough to exhibit this behaviour, although it is possible that a proportion of them could have been larger in the past.

Reipurth and Clarke (2001) propose the embryo ejection model. In this case, brown dwarfs are formed from pre-stellar cores which are ejected from newly-formed multiple systems. The cores are expelled through dynamical encounters with other objects in the multiple system. Their expulsion truncates their accretion, preventing them from reaching the hydrogen-burning limit. However, embryo ejection would also imply a very low binarity rate below 5%; the observed rate is $15 \pm 5\%$ (see Gizis *et al.* 2003). Also, embryo ejection would imply that brown dwarfs will have a greater velocity dispersion than the clusters from which they form. However, any such increase must be quite small. In the case of the Pleiades star-forming region, even an increase as small as $3\,\mathrm{km\,s^{-1}}$ would be enough to remove all brown dwarfs from the region (Reid and Hawley 2005). Observational evidence shows that this has not happened.

Padoan and Nordlund (2002) propose a model of turbulent fragmentation. In this case, the high densities required for brown dwarf formation are achieved through the convergence of turbulent flows within a star-forming region. However, the turbulent fragmentation model struggles to reproduce the observed binarity distribution of brown dwarfs (Reggiani and Meyer 2011).

Whitworth and Zinnecker (2004) propose formation based on photo-erosion. In this scenario, substellar objects form in the presence of a high-mass star embedded in a H II region. The high-energy ultraviolet photons from the high-mass star 'erode' the protostellar core by heating and removing its outer layers. Consequently, the core cannot accrete enough mass to reach the hydrogen-burning limit, and instead results in a brown dwarf. However, this mechanism would be quite inefficient in practice; it would require a large pre-stellar core as the erosion would leave little of that core behind, and also this process can only occur in close proximity to OB stars (Stamatellos 2013).

It can be seen that there is currently little consensus on which, if any, of the above models is correct for brown dwarf formation. It may also be possible that there is in fact more than one pathway to brown dwarf formation. With such a lack of basic clarity regarding the actual mechanism of action, it is difficult to draw any definitive conclusions about the impact of metallicity. However, some insight into this issue may be suggested through theoretical simulations.

Depending on which channels are most important, the expected metallicity dependence of brown dwarf formation will differ. Some scenarios, such as the embryo ejection mechanism, can be expected to be fairly insensitive to metallicity. Low metallicity makes it more difficult for a gas to cool via emission in molecular and atomic lines. This has an impact on the Jeans mass in the fragmentation scenario, because higher temperatures increase the Jeans mass.

Abel *et al.* (2002) consider simulations of the very first generation of stars in the Universe, the so-called Population III stars. These objects would have possessed zero metallicity, there having been no previous generations of star formation in which any heavy elements could have formed. Abel *et al.* (2002) find that the masses of these objects would have to have been extremely high, perhaps greater than $\sim$100 solar masses; no smaller objects could have formed in this epoch. Consequently, it can be suggested that there is no such thing as a zero-metallicity brown dwarf.

Furthermore, Bate (2005) conducted simulations of the star formation process through fragmentation. In particular, they considered the effect that metallicity has on the opacity limit for the fragmentation process. In this simulation they also consider a low-metallicity case (corresponding to an ISM with an enrichment of $\sim 5\times10^{-4}$ of the solar level). In the low-metallicity case, the minimum mass found is around 3 times higher, a value of

$\sim$9 Jupiter masses compared to $\sim 3\,\mathrm{M}_J$ for the solar case. However, apart from this shift of the low-mass cutoff, the brown dwarf mass functions of the two simulations were very similar, even having similar median masses.

If the Bate (2005) result is an accurate depiction of brown dwarf formation, then we can assume that halo brown dwarf formation will have a higher low mass cutoff than that of the thin disc, but otherwise the mass distributions of objects will be broadly similar.

Thus, depending on the dominant formation channels, the minimum mass of brown dwarfs may depend on metallicity. However, the IMF for higher-mass brown dwarfs can be assumed to be fairly insensitive to metallicity.

Chapter 2

Blue T dwarfs in UKIDSS

2.1 Blue T dwarfs

Blue near-infrared colours are a sign of CIA H2-absorption. CIA H2 is enhanced by high surface gravity and/or low metallicity. As halo objects will be expected to be metal-poor in composition, halo T dwarfs are thus expected to show blue near-infrared colours. Consequently, I sought to undertake a search for objects with such colours. The first step in this work was to identify a region of colour-space to select from.

2.2 Identifying candidates

The volume probed for T dwarfs by the UKIRT Infrared Deep Sky Survey (UKIDSS; Lawrence *et al.* 2007) Large Area Survey (LAS) is much larger than previously available, making feasible the identification of the T subdwarf population. Many T dwarfs have now been published as part of an ongoing program to spectroscopically confirm many T dwarfs in the UKIDSS LAS, as reported in Burningham *et al.* (2010a) and references therein, and it is from this group that that targets investigated in this work were first identified.

The UKIDSS sample of T dwarfs were themselves selected through a set of colour cuts, requiring $J - H < 0.1$ and $J - K < 0.1$. Then, after cross-matching with SDSS, an object would be required either to have $z - J > 3.0$ or to be undetected in in z. Potential metal-poor T dwarfs were identified from amongst these spectroscopically-confirmed objects using a $H - K$ vs. spectral type plot (shown in Figure 2.1). The UKIDSS sample is most

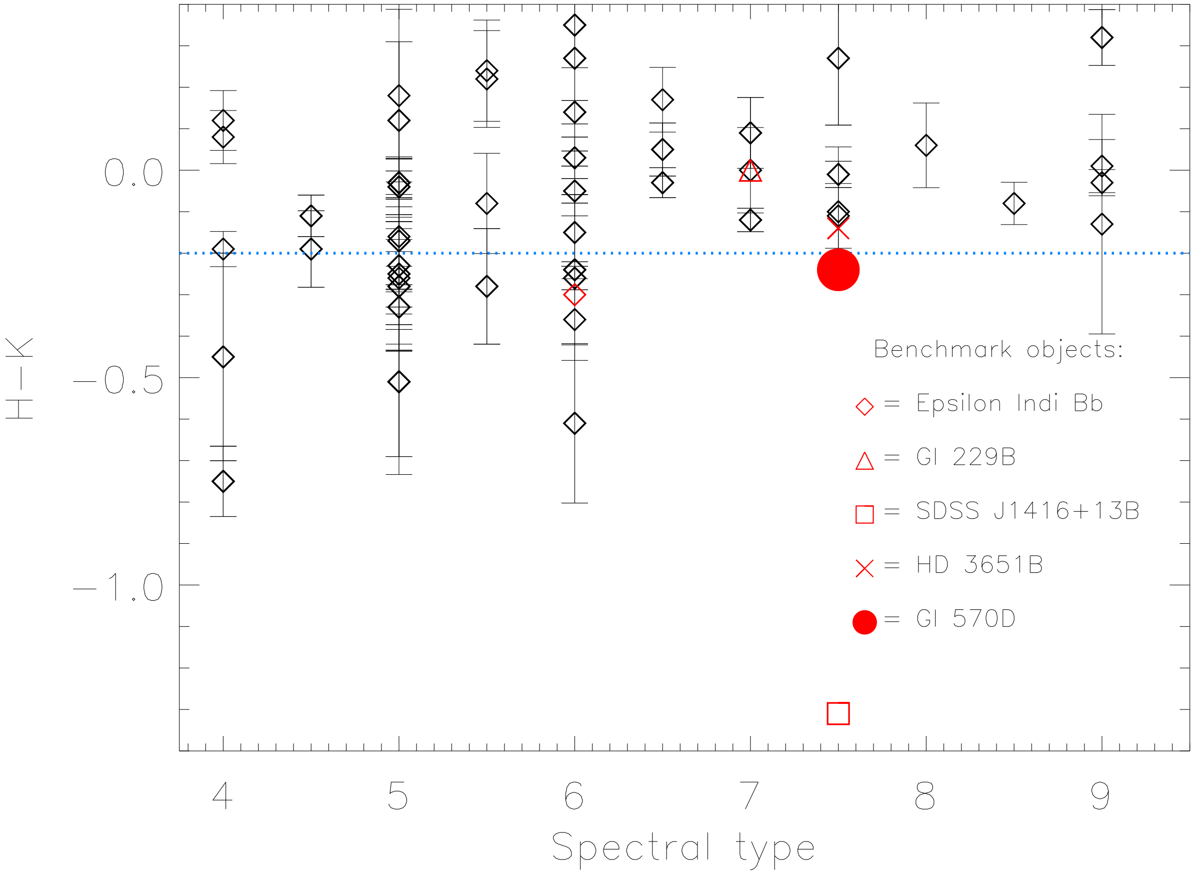

Figure 2.1: A plot showing $H-K$ plotted against spectral type. Black diamonds represent UKIDSS T dwarfs (see Burningham *et al.* 2010a; Pinfield *et al.* 2008; Lodieu *et al.* 2007), with the error bars showing the uncertainty in $H-K$. The other symbols, in red, represent binary-benchmark T dwarfs. Also included as a further point of comparison is SDSS J1416+1348B, from Burningham *et al.* (2010b). The blue dashed line represents the $H-K=-0.2$ selection criterion.

complete for targets later than a spectral type of T4, so a type later than T4 was required along with the $H-K<-0.2$ cut.

The $H-K$ cut is intended to select blue outliers relative to the population, as the K-band is expected to be the most strongly-affected by CIA H_2 absorption, and this colour selection should thus prefer a set of objects showing suppressed K-band flux. Comparisons to T dwarfs from binary systems, whose primary stars' provide fiducial constraints on metallicity, support the criteria. HD 3651B, with an [Fe/H]$=0.12\pm0.04$ (Santos *et al.* 2004) also lies outside of the selection area. Gliese 570D, with an essentially solar metallicity of [Fe/H]$=0.04\pm0.06$ (Feltzing and Gustafsson 1998), lies on the boundary, whereas the metal-poor T6 Epsilon Indi Bb, with [Fe/H]$= -0.23 \pm 0.06$ (Santos *et al.* 2004), lies within the selection area.

I also note that K-band flux is sensitive to surface gravity as well as metallicity. The opacity of CIA H_2 absorption varies with the square of the local gas number density (Saumon *et al.* 1994). For a given $T_{\rm eff}$, higher-gravity T dwarfs will have higher gas pressures and thus tend to have larger H_2 opacity. As such they will be fainter in the K-band, leading to bluer $H-K$ colours than comparable lower-gravity objects. This surface gravity-related CIA H_2 absorption will be strongest at late-T objects (see Burgasser *et al.* 2002; Knapp *et al.* 2004). In practice, for many objects blue $H-K$ colours may well be due to a combination of gravity and metallicity (Knapp *et al.* 2004). This degeneracy means that caution must be exercised before any attempt is made to infer a T dwarf's metallicity solely on the basis of its near-infrared colours. For instance, Liu *et al.* (2007) show that for a $T_{\rm eff} = 900\,{\rm K}$ object, increasing $\log g$ from 5.0 to 5.5 dex changes the K/H flux ratio by $\sim$0.25, while reducing metallicity from [m/H]= 0.0 to -0.5 changes the ratio by $\sim$0.45. Halo objects, however, may well have far lower [m/H] values (see Gizis 1997), so for these objects depression of the K band flux may come to be dominated by metallicity effects. The model trend suggests that the bulk of colour variation may be due to metallicity for halo objects. Although surface gravity will certainly play a role, the bulk of radius evolution is expected to occur by ages of $\sim$ 1 Gyr for brown dwarfs (Burrows *et al.* 2001). This implies a maximum surface gravity for brown dwarfs. Saumon and Marley (2008) find this to be $\log g = 5.366$ in the case of a $T_{\rm eff} = 1380\,{\rm K}$ and $0.068{\rm M}_{\odot}$ brown dwarf. This further suggests that the largest source in variation of H and K-band colours in halo T dwarfs is likely to be from metallicity.

In addition to the previously-published DR4 LAS T dwarfs a more recently-identified object from DR5, ULAS J1504+0538, was also included in the $H-K$ selection. Since the spectroscopic confirmation of ULAS J1504+0538 (see Section 2.4), it has been identified by Scholz (2010a) as a common proper motion binary companion to Hip 73786. As such, from here on I will refer to this object as Hip 73786B. The colour-type selection yielded a total of twelve candidates. The sample is shown in Figure 2.1, with $H-K$ plotted in relation to spectral type. The candidates lie below the dashed line. As can be seen, most of the candidates cluster at spectral types $<$ T5.5, with none later than T6.

Table 2.1: Summary of the $YJHK$ photometric colours of each object.

Object	Disc.	J mag	$Y - J$	$J - H$	$H - K$	$J - K$
ULAS J084211.68+093611.78	3	18.38±0.02	1.2±0.2	-0.46±0.03	-0.2±0.2	-0.7±0.2
ULAS J092605.47+083517.00	3	18.57±0.02	1.3±0.2	-0.12±0.02	-0.5±0.3	-0.6±0.3
ULAS J095829.86-003932.0	1	18.95±0.06	0.9±0.2	-0.5±0.1	-0.3±0.2	-0.5±0.1
ULAS J101243.54+102101.70	3	16.87±0.01	1.13±0.02	-0.34±0.02	-0.33±0.05	-0.68±0.05
ULAS J101821.78+072547.10	2	17.71±0.04	1.19±0.09	-0.16±0.08	-0.3±0.2	-0.41±0.2
ULAS J123327.45+121952.20	3	17.87±0.03	1.35±0.07	-0.41±0.07	-0.75±0.08	-1.16±0.07
ULAS J130303.54+001627.70	1	19.02±0.03	1.2±0.2	-0.47±0.09	-0.6±0.2	-1.1±0.2
ULAS J131943.77+120900.20	3	18.90±0.05	1.49±0.07	-0.27±0.2	-0.24±0.2	-0.5±0.1
ULAS J132048.12+102910.60	3	17.82±0.02	1.15±0.06	-0.07±0.05	-0.3±0.1	-0.4±0.13
ULAS J150135.33+082215.20	1	18.32±0.02	1.4±0.2	0.02±0.03	-0.23±0.06	-0.21±0.06
ULAS J150457.66+053800.80	-	16.59±0.02	1.05±0.03	-0.46±0.04	-0.4±0.1	-0.82±0.09
ULAS J232035.28+144829.80	-	16.79±0.02	1.35±0.03	-0.35±0.03	-0.26±0.03	-0.61±0.03

The data is all presented on the MKO filter system. Discovery paper references: 1) Pinfield *et al.* (2008); 2) Lodieu *et al.* (2007); 3) Burningham *et al.* (2010a). A '-' indicates a spectrum published for the first time here. A J-band spectrum for ULAS J2320+1448 was published in Burningham *et al.* (2010a), however the full JHK spectrum shown in Figure 2.3 is new data. The values after the numbers are the magnitude errors.

These are: 1) Pinfield *et al.* (2008); 2) Lodieu *et al.* (2007); 3) also known as Hip 73786B, the spectrum is new data; 4) indicates Burningham *et al.* (2010a).

2.3 Near-infrared photometry

The near infrared photometry for the selected objects is summarised in Table 2.1, the bulk of the which has been published in Burningham *et al.* (2010a) and references therein, where exposure times and observing conditions may also be found. All photometry is presented on the Mauna Kea Observatories (MKO) system (Tokunaga *et al.* 2002). The full co-ordinates of all objects are show in Table 2.1, along with references to their discovery papers.

The photometry for Hip 73786B is derived from the newly-presented spectrum. Hip 73786B was observed using the Wide Field CAMera (WFCAM; Casali *et al.* 2007) on UKIRT, on 12 July 2009(UT), with a seeing of ∼1.2 arcseconds. The object was imaged in Y and J using a 3-point jitter-pattern with 2x2 microstepping. Each individual exposure was 10 seconds. The object was observed in H and K with two sets of 5-point jitter patterns at an individual exposure of 10 seconds, with 2x2 microstepping. This led to a total exposure in each band of 400 seconds. The data were processed using the WFCAM pipeline by the Cambridge Astronomical Surveys Unit (Irwin *et al.* 2004), and archived at the WFCAM Science Archive (Hambly *et al.* 2008).

2.4 Spectroscopy

2.4.1 New spectra

Hip 73786B and ULAS J2320+1448 represent previously-unpublished spectra. The sources for previously published spectroscopy are summarised in Table 2.1.

ULAS J2320+1448 was observed on the Near InfraRed Imager and Spectrometer (NIRI; see Hodapp *et al.* 2003) on the Gemini-North telescope to obtain deeper J, H and K band spectra on 22 August 2008, 12 October 2008 and 14 October 2008 (UT) respectively. These data were reduced using standard NIRI IRAF packages. The images were flat fielded, masked for bad pixels and median stacked. A dispersion solution was fitted using the arc spectra. The method used was in common with that used in Burningham *et al.* (2010a).The target was observed at an airmass of 1.01, with an integration time of 750s. The resulting spectrum has an average resolution of $R \sim 460$.

To gain a higher signal-to-noise ratio, the short J-band discovery spectrum was combined with the new deep J-band spectrum, using a weighted average. The J, H and K-band spectra were then scaled by photometry to place them on a common flux scale before combining them to produce a flux-calibrated JHK spectrum.

Hip 73786B was observed on the InfraRed Camera and Spectrograph (IRCS; Kobayashi *et al.* 2000) on the Subaru telescope on Mauna Kea to obtain R$\sim$ 100 JH and HK spectra on the nights of 7^{th} May 2009 and 30^{th} December 2009 respectively. The data were sky subtracted using generic IRAF tools, and median stacked. An arc frame was used to fit a dispersion solution. The spectra were then extracted and cosmic rays and bad pixels were removed using a sigma-clipping algorithm.

Telluric correction was achieved by dividing each extracted target spectrum by that of an F4V star, which was observed just after the target and at a similar airmass. Prior to division, hydrogen lines were removed from the standard star spectrum by interpolating the stellar continuum. Relative flux calibration was then achieved by multiplying through by a blackbody spectrum of the appropriate $T_{\rm eff}$. The JH and HK spectra were then joined using the overlap region between 1.43μm and 1.63μm in the H-band to place the spectra on a common flux scale. The overlap region covers a wide range and includes the H-band peak. As a test of the merger, spectrophotometric colours were computed from the merged spectrum, and these were found to be entirely in agreement with the photometry.

2.4.2 Spectral types

Objects were assigned types using their indices and comparisons to template spectra, following the general procedures set out in Burgasser *et al.* (2006b). The indices used in the Burgasser system are shown in Table 2.2. The indices themselves are shown in Figure 2.2, from Burgasser *et al.* (2006b).

In brief, these indices target absorption bands of H_2O and CH_4 in the J-, H- and K-bands, which have been found to correlate with near-infrared spectral type. The template spectra used here are those indicated in Burgasser *et al.* (2006b) and references therein. Typing was conducted through a two-stage process. First, an index-based type was arrived at, using the J and (where available) the H-band indices, by taking the median of these values. Then, independently, a type was arrived at by plotting the object spectrum against an appropriate range of standard spectra, and visually inspecting the plot to see which the object matches most closely. Figure 2.3 show the closest-matching template spectra for each object. A type is derived from the index values by taking their median. This is then averaged with the template spectrum type; the advantage of this process is that it

Table 2.2: Indices used in spectral typing

Index	Numerator	Denominator	Feature
H_2O-J	1.140-1.165	1.260-1.285	1.15μm H_2O
CH_4-J	1.315-1.340	1.260-1.285	1.32μm CH_4
H_2O-H	1.480-1.520	1.560-1.600	1.4μm H_2O
CH_4-K	1.635-1.675	1.560-1.600	1.65μm CH_4
H_2O-K	1.975-1.995	2.080-2.100	1.9μm H_2O
CH_4-K	2.215-2.255	2.080-2.100	2.2μm CH_4

A summary of the wavelength ranges and the features used in the Burgasser *et al.* (2006b) spectral typing system.

accounts for both broad spectral structure and also for index-based measurements.

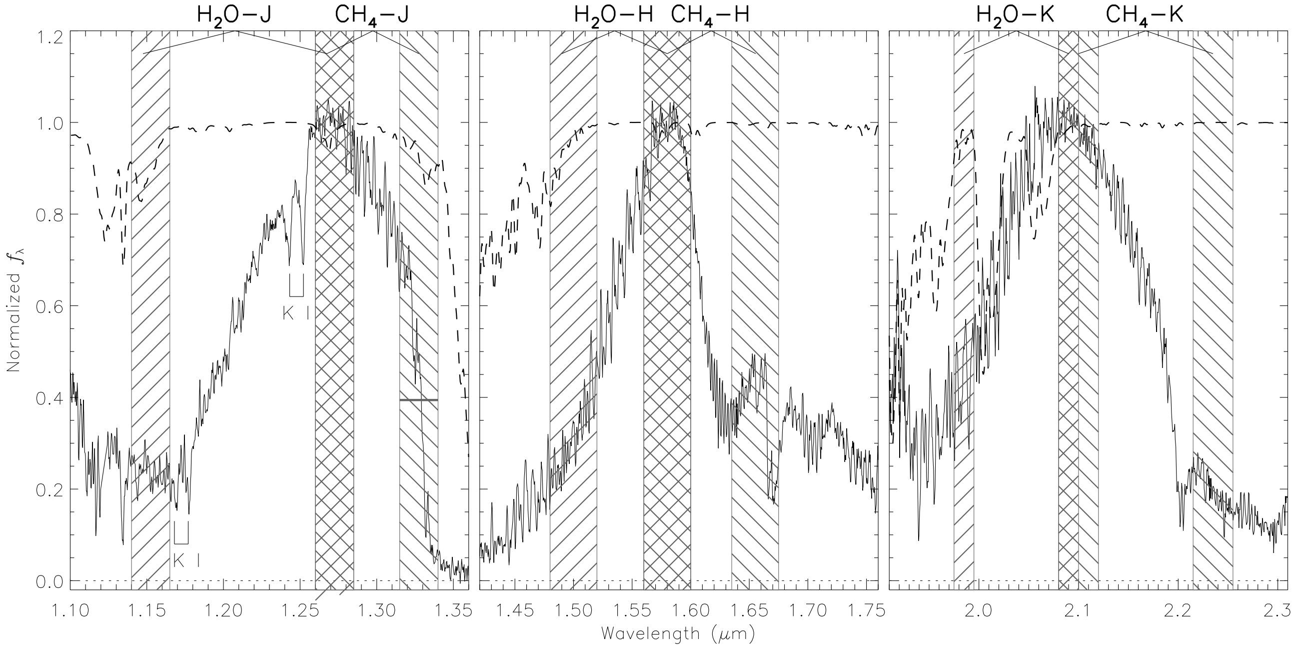

Figure 2.2: The Burgasser *et al.* (2006b) spectral indices, shown with 2MASS J1503+2525.

Only the indices in the J- and H-bands have been used for the purpose of typing the T dwarfs in this study, as unusual K-band spectroscopic morphology is one of the defining characteristics by which they were selected, potentially invalidating the use of this spectral region as a means of obtaining spectral types consistent with those for normal T dwarfs. In addition, not all objects have K-band spectra. Therefore it was felt acceptable to neglect the K-bands for spectral-typing purposes. However the index values are shown in Table 2.3 for reference. This table also summarises the bands used in the typing and the template spectra that were selected. Figure 2.3 shows the spectra for all candidates, and their comparison to the relevant spectral standards.

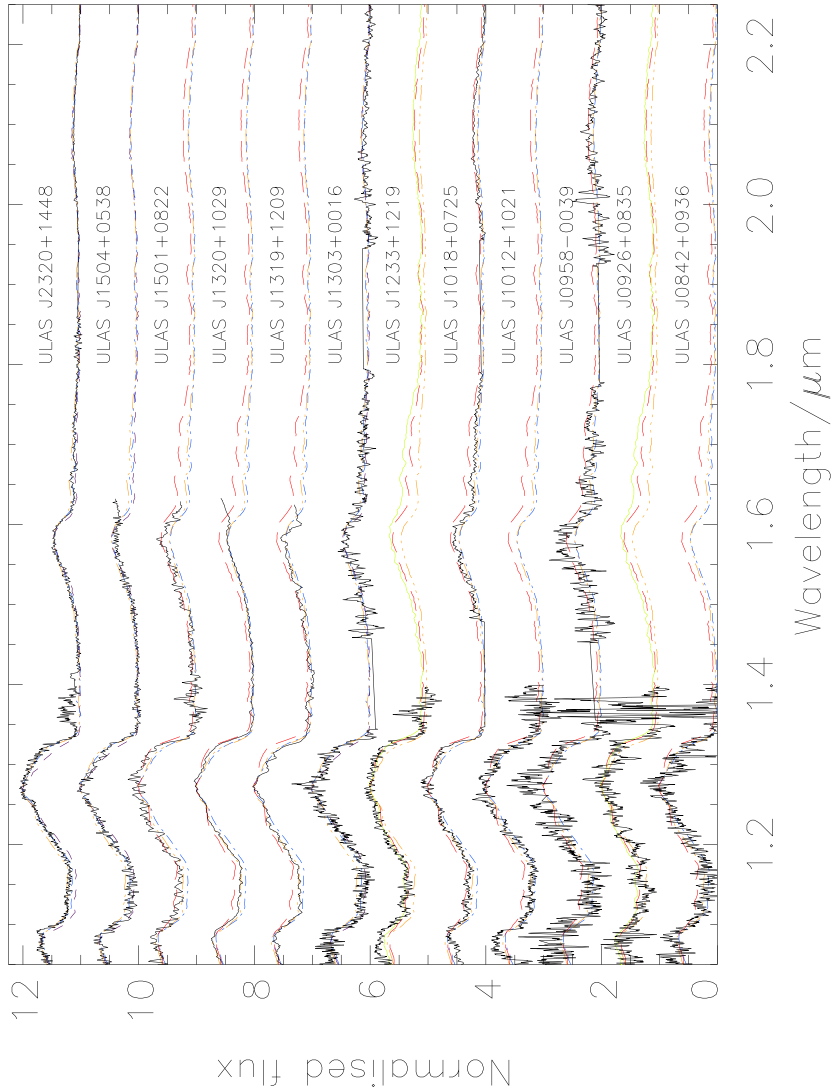

Figure 2.3: Spectra for all six candidates. In each figure, the object spectrum is shown as a solid black line. The objects are all shown in comparison to T dwarf standards. These are represented by the lines on each plot, marked with the respective spectral types. The T3 to T7 spectral standards are from Burgasser *et al.* (2006a) and references therein. The object and standard spectra in each plot have been normalised against their mean fluxes around 1.27μm. Each spectrum has been labeled with the name of the object it is for. The T7 standard is shown in purple, the T6 in blue, the T5 in orange, the T4 in red and the T3 in green. Standard spectra are shown as various dashed lines, to help distinguish them from the object spectra.

In cases where spectroscopy is available over the full JHK region, the uncertainties in types are ±0.5 subtypes. However, for some objects there are only J-band data or JH-data. Also, the comparison template spectra allow us to type an object to ±1 subtype accuracy, not ±0.5. Therefore accuracies have been rounded to ±1 subtype, although index types themselves are generally more accurate.

Table 2.3: Spectral typing summary for the candidates.

Object	H_2O-J	CH_4-J	H_2O-H	CH_4-H	CH_4-K	Median type	Template spectrum	Adopted type
ULAS J0842+0936	0.17±0.02 (T5/T6)	0.35±0.02 (T5/T6)				T5.5	T6	T6±1
ULAS J0926+0835	0.32±0.02 (T4/T5)	0.53±0.02 (T3/T4)				T4	T4	T4±1
ULAS J0958-0039	0.16 (T6)	0.34 (T6)	0.39 (T4)	0.41 (T5)	0.14 (T6)	T6	T6	T6p±1
ULAS J1012+1021	0.202±0.008 (T5)	0.366±0.009 (T5)				T5	T6	T5.5±1
ULAS J1018+0725	0.36 (T4)	0.44 (T5)	0.38 (T4)	0.45 (T5)	0.15 (T6)	T5	T5	T5±1
ULAS J1233+1219	0.365±0.007 (T4)	0.528±0.007 (T3)				T3.5	T4	T4±1
ULAS J1303+0016	0.11 (T7)	0.32 (T6)	0.34 (T5)	0.37 (T5)	0.03 (T7)	T6	T6	T6p±1
ULAS J1319+1209	0.233±0.009 (T5)	0.322±0.006 (T6)	0.45±0.02 (T3/T4)			T5	T5	T5±1
ULAS J1320+1029	0.247±0.003 (T5)	0.479±0.004 (T4)	0.318±0.004 (T6)			T5	T5	T5±1
ULAS J1501+0822	0.29 (T5)	0.43 (T5)	0.41 (T5)			T5	T4	T4.5±1
Hip 73786B	0.127±0.004 (T6/T7)	0.383±0.003 (T5)	0.307±0.006 (T6)	0.355±0.009 (T5/T6)	0.45±0.03 (T3)	T5.5	T6	T6p±1
ULAS J2320+1448	0.206±0.004 (T5)	0.396±0.004 (T5)	0.303±0.006 (T6)	0.292±0.003 (T6)	0.172±0.004 (T6)	T6	T6	T6±1

Summary of the objects' spectral type indices, as per Burgasser *et al.* (2006a). The spectral types assigned from those indices are shown in parentheses after the number. Where the error on an index is consistent with more than one type, this is shown with a slash, for instance T4/T5 would indicate an object whose relevant index could be consistent with either value. Uncertainties in typing are assigned based on the types from different indices. The Template Spectrum column refers to the type of the spectral standard that best matches the shape of the spectrum. The Adopted Type column refers to the spectral type that was derived for each object. Errors are shown where error spectra are available. Error spectra are not available for ULAS J0958-0039, ULAS J1018+0725, ULAS J1303+0016 or ULAS J1501+0822. Final spectral types are arrived at by averaging the median of the J, H-band indices with the type from the template comparison. This is done to give equal weighting to broad structure and numerical indices.
In all cases, the H_2O-J and CH_4-J indices were used. Where H and K-band spectra were available, H_2O-H, CH_4-H and CH_4-K indices were also used.

2.4.3 Notes on unusual objects

Some objects show a large scatter in their indices, sometimes varying by as much as three subtypes between indices. This can be seen in Table 2.3, where the type inferred from each index is shown in parentheses after the value.

Objects with $H_2O - H$-early peculiarity (Burningham *et al.* 2010a) have a $H_2O - H$ index at least 2 subtypes earlier than the $H_2O - J$ index. Amongst the objects, ULAS J0958-0039 displays this behaviour, with an assigned type of T6 and a $H_2O - H$ type of T4 and a $H_2O - J$ type of T6. ULAS J1303+0016 also shows this behaviour. There is an additional borderline case, ULAS J1319+1209, which has a $H_2O - J$ type of T5 and a $H_2O - H$ type of T3/T4.

It is possible that the cause for these peculiarities may lie in the physics of low-metallicity or high surface gravity atmospheres. However this behaviour is not consistent across the sample, and anyway without derived metallicities or surface gravities for the objects it is not currently possible to evaluate this idea. Binarity has been ruled out as possible cause, however (Burningham *et al.* 2010a).

Lastly, ULAS J1018+0725 shows some differences both from the standards and from the rest of the sample. Its Y-band peak is narrower relative to the standards and there is less flux bluewards of 1.1μm. Also, its K-band peak actually appears enhanced relative to the standards. These may in fact be evidence of high metallicity and/or low gravity, as suggested in Lodieu *et al.* (2007). Its $H - K = -0.3 \pm 0.2$, which is not particularly blue relative to the rest of the sample. Given the error on its colours, it may be a higher-metallicity object that has scattered into the colour-selection area.

2.5 Distance estimates

The distances of the candidates were estimated using the relationships between spectral types and absolute magnitudes from Marocco *et al.* (2010). The J-band was used for distance estimates, as it is considered least affected by gravity or metallicity. The results are summarised in Table 2.6. The relationship used is not based on metal-poor T dwarfs. Metallicity effects may change the absolute magnitudes of T dwarfs in the J-band. However, I continue to use the Marocco *et al.* (2010) relationships, making the working assumption that they are applicable. Errors on the distances were estimated using the uncertainties in spectral type, the uncertainties in J-band magnitude and the scatter in the relation.

Table 2.4: Follow-up sources and epoch data.

Object	UKIDSS date	Epoch diff (yr)	Follow-up source	n_{ref}
ULAS J0842+0936	2007/02/16	0.90603	UFTI	11
ULAS J0926+0835	2007/01/22	1.02155	EMMI	17
ULAS J0958-0016	2005/12/30	2.08705	EMMI	15
ULAS J1012+1021	2007/12/02	0.61579	WFCAM	23
ULAS J1018+0725	2005/12/28	1.05775	UKIDSS	26
ULAS J1233+1219	2007/03/05	0.74209	EMMI	25
ULAS J1303+0016	2005/06/12	4.01232	UKIDSS	23
ULAS J1319+1209	2007/04/16	0.79740	EMMI	23
ULAS J1320+1029	2007/02/25	1.17975	EFOSC2	21
ULAS J1501+0822	2006/07/23	0.61084	LIRIS	12
Hip 73786B	2008/04/17	1.23460	WFCAM	45
ULAS J2320+1448	2008/06/27	7.83025	SDSS	14

Dates and epochs used in proper motions. UKIDSS date is the date of the *J*-band LAS image. n_{ref} refers to the number of reference stars used for each object. The SNR for the T dwarf from UKIDSS is shown first, followed by the SNR from the second epoch. X, Y RMS refers to the RMS scatter about the co-ordinate transforms. The next two columns show the calculated proper motions for RA and declination, in $\mathrm{mas\,yr^{-1}}$. S1 is the seeing in the LAS image, S2 the seeing in the follow-up image. Coordinates are transformed from the second-epoch image to the UKIDSS *J*-band image for each object. The UKIDSS *J*-band pixel scale is 0.2 arcseconds per pixel.

Table 2.5: SNRs, RMSs and proper motions for objects.

Object	T dwarf SNR	X,Y RMS (pixels)	$\mu_{\alpha cos\delta}$, μ_δ ($\mathrm{mas\,yr^{-1}}$)	S1, S2 (pixels)
ULAS J0842+0936	9.0, 33.3	0.111, 0.306	-176±209, +36±218	5.1, 8.3
ULAS J0926+0835	6.6, 13.7	0.107, 0.156	-472±144, -438±146	7.7, 8.4
ULAS J0958-0016	7.2, 17.9	0.148, 0.174	+43±99, +31±100	4.1, 5.0
ULAS J1012+1021	32.3, 43.5	0.085, 0.093	-234±87, -631±87	4.4, 5.3
ULAS J1018+0725	18.2, 18.5	0.104, 0.120	+181±48, +60±50	3.2, 3.2
ULAS J1233+1219	11.9, 22.2	0.105, 0.134	+198±189, +168±190	3.0, 6.7
ULAS J1303+0016	4.9, 3.5	0.130, 0.106	-18±138, -220±137	3.1, 4.2
ULAS J1319+1209	8.5, 12.9	0.089, 0.139	-525±72, +111±75	5.2, 8.0
ULAS J1320+1029	16.1, 8.3	0.151, 0.151	+9±242, -60±243	5.2, 11.8
ULAS J1501+0822	8.0, 12.5	0.310, 0.237	-136±180, -113±249	8.5, 4.2
Hip 73786B	27.8, 20.4	0.095, 0.093	-661±60, -510±59	4.8, 7.5
ULAS J2320+1448	18.9, 11.3	0.093, 0.104	+399±26, +122±26	4.7, 2.2

The first column is the SNR for the T dwarf image in UKIDSS, followed by the SNR from the second epoch. X, Y RMS refers to the RMS scatter about the co-ordinate transforms. The next two columns show the calculated proper motions for RA and declination, in $\mathrm{mas\,yr^{-1}}$. S1 is the seeing in the LAS image, S2 the seeing in the follow-up image. Coordinates are transformed from the second-epoch image to the UKIDSS *J*-band image for each object. The UKIDSS *J*-band pixel scale is 0.2 arcseconds per pixel.

2.6 Proper motions

The photometric follow-up observations that were carried out provided a second epoch of imaging data for each object. The Image Reduction and Analysis Facility (IRAF; see Tody 1986) task GEOMAP was used to derive spatial transformations into the UKIDSS LAS J-band image for each object, based on the positions of reference stars identified in the follow-up and UKIDSS images. Then the GEOMAP was used for the co-ordinate transformation. The fitting geometry used was general, with a polynomial function of order 3 in x and y. In every case the follow-up image was used as the reference image for the co-ordinate transform. Followup images were obtained from a variety of instruments, including the UKIRT Fast-Track Imager (UFTI; see Roche *et al.* 2003), the Long-slit Intermediate Resolution Infrared Spectrograph (LIRIS; see Manchado *et al.* 2003), the Wide Field Infrared Camera For UKIRT (WFCAM; see Casali *et al.* 2007), the ESO Multi-Mode Instrument (EMMI; see Dekker *et al.* 1986) and the ESO Faint Object Spectrograph and Camera (EFOSC2; see Buzzoni *et al.* 1984).

Then the pixel coordinates of the targets were transformed into the follow-up images into the LAS image, using GEOXYTRAN, and their change in position was calculated (relative to the reference stars) between the two epochs.

The uncertainties associated with the proper motion measurement primarily come from the spatial transformations, and the accuracy with which it has been possible to measure the position of the targets (by centroiding) in the image data. Then the instrument pixel scale was used in each case to convert the results into arcseconds. The UKIDSS J-band pixel scale is 0.2 arcseconds per pixel. The dates of the observations were then used to calculate a proper motion. These results are summarised in Table 2.4 and Table 2.5.

Errors on proper motions were calculated by summing in quadrature the centroiding uncertainty and the RMS about the fit of the co-ordinate transform and the epoch difference. The uncertainty in the centroiding was estimated by obtaining the scatter of the centroids for a large number of simulated stellar images constructed using the observed signal-to-noise and seeing for each target observation. Centroiding uncertainties were calculated through simulated data with a Gaussian PSF and with appropriate Poisson noise added. The availability and quality of the measured proper motions of the T dwarfs is affected by various factors including the time between epochs, the number of usable reference stars in the images and the S/N of both the T dwarf and the reference stars. The centroiding uncertainties (in pixels) varied between a minimum of 0.04 pixels

Table 2.6: Estimated distances, proper motions and kinematics.

Name	Distance (pc)	V_{tan} ($\mathrm{km\,s^{-1}}$)	U ($\mathrm{km\,s^{-1}}$)	V ($\mathrm{km\,s^{-1}}$)	l (deg)	b (deg)	Halo test ($\mathrm{km\,s^{-1}}$)
ULAS J0842+0936	50±9	43±40	38±36	-1±44	216.89	28.94	51
ULAS J0926+0835	70±11	213±59	62±40	-140±46	223.84	38.16	122
ULAS J0958-0039	65±9	16±22	3±27	-3±27	239.49	40.02	32
ULAS J1012+1021	28±5	89±20	-1±11	-87±17	229.37	49.09	52
ULAS J1018+0725	44±7	39±12	-16±10	5±9	234.27	48.75	43
ULAS J1233+1219	50±8	62±40	-11±45	45±45	286.16	74.61	81
ULAS J1303+0016	67±12	70±42	-20±44	-68±45	309.34	63.00	39
ULAS J1319+1209	75±12	192±40	183±37	-92±29	328.20	73.62	192
ULAS J1320+1029	46±7	13±37	0±51	-21±52	326.89	71.98	19
ULAS J1501+0822	60±10	51±49	12±52	-61±63	7.70	53.97	41
Hip 73786B	22±4	87±25	-48±7	-75±4	4.90	51.66	62
ULAS J2320+1448	24±5	48±10	55±10	-20±3	92.45	-42.62	57

This table shows object distances in parsecs, estimated by spectral type, using the relationships between J-band type and absolute magnitude from Marocco *et al.* (2010). The distance range shows the distances for the earliest and latest spectral types that are consistent with each object's spectral type range. It also shows the estimated tangential velocities, and their errors. With the exception of HIP 73786B, all objects are assumed to have $V_{\mathrm{rad}} = 0$ $\mathrm{km\,s^{-1}}$. The last column applies the halo-candidate test from Reid *et al.* (2001), namely that $[U^2 + (V + 35)^2]^{1/2} \geq 94\mathrm{km\,s^{-1}}$.

for ULAS J1233+1219 and a maximum of 2.38 pixels for ULAS J1320+1029. The mean value was 0.54 pixels.

ULAS J2320+1448 was measured with the method of Zhang *et al.* (2009), with its UKIDSS and SDSS images (SDSS; see York *et al.* 2000). Due to the much longer baseline, this has resulted in a lower error for this object's proper motion compared to the rest of the sample.

2.7 Kinematics

Tangential velocities have been estimated for the targets using the proper motion and distance estimates, listed in Table 2.6. Errors in tangential velocity and U and V were estimated using a Monte Carlo script, accounting for errors in proper motion and in the distance estimates. The Monte Carlo used 10000 loop iterations per object. In each iteration, the values for each object were offset from their measured ones by a randomization factor. This factor was calculated by multiplying the measured error by a random number (of value between 0.0 and 1.0) and adding the resulting number to the measured motion.

Two objects were found to have V_{tan} greater than 100 $\mathrm{km\,s^{-1}}$, suggestive of halo kinematics: ULAS J0926+0835 with $V_{\mathrm{tan}} = 213 \pm 59$ $\mathrm{km\,s^{-1}}$ and ULAS J1319+1209 with $V_{\mathrm{tan}} = 192 \pm 40$ $\mathrm{km\,s^{-1}}$.

As the LAS is oriented out of the galactic plane, some insight can be gained into the targets' U and V space velocity components. For targets at high galactic latitudes, the radial velocity will consist mostly of W motion, with small U and V components. Therefore, in such cases it is possible to assess U and V to some extent without having a radial velocity. So, for all objects, proper motions, distance and co-ordinates were transformed into UVW components. This was done assuming $V_{\rm rad} = 0$ for all objects except Hip 73786B, where the values for Hip 73786A were used. The results are summarised in Table 2.6. The results are also displayed in Figure 2.4. The co-ordinate system that has been used is a left-handed one, such that U is positive toward the galactic anti-centre and V positive in the direction of galactic rotation. To account for the possible effects of radial velocity, I have also calculated U and V for each object for the possibilities of $V_{\rm rad} = 100$ and -100 $\rm km\,s^{-1}$. This is shown in Figure 2.4 by the blue dot-dashed lines running through each object.

Four objects (ULAS J1233+1219, ULAS J1303+0016, ULAS J1319+1209 and ULAS J1320+1029) have $b > 60$ degrees, and their U and V values are the best constrained in the study. Of these, ULAS J1233+1219 displays kinematics most likely to be thin disc values, although its U,V error bars do extend beyond the outer disc ellipsoid. Unless its $V_{\rm rad}$ is outside the $\pm 100 \rm km\,s^{-1}$ indicated in Figure 2.4, these kinematics seem to argue against it being a halo object. If, it is not a halo object, then its blue near-infrared colours come as a surprise; ULAS J1233+1219 has the bluest $J - K$ in the entire sample ($J - K = -1.2 \pm 0.1$). This suggests a strongly-depressed K-band and is notable in light of its apparently disc-like tangential velocity (although no K-band spectrum has yet been obtained for this object). This situation is reminiscent of the only T dwarf known to be bluer in $J - K$, SDSS J1416+1348B (see Burningham *et al.* 2010b; Scholz 2010b), with $J - K = -1.67$. The SDSS J1416+13AB system has velocities consistent with the thin disc.

Reid *et al.* (2001) set the criterion that objects that satisfy

$$[U^2 + (V + 35)^2]^{1/2} > 94\,\rm km\,s^{-1} \tag{2.1}$$

are outside of the 2σ velocity region encompassing thin and thick-disc stars as described by Chiba and Beers (2000) and Reid *et al.* (2001). ULAS J0926+0835 and ULAS J1319+1209 satisfy this condition (see Table 2.6), further highlighting their likely halo membership.

Two objects stand out on Figure 2.4 as halo candidates. ULAS J1319+1209 has U and V ($U = 183 \pm 37$, $V = -92 \pm 29$ $\mathrm{km\,s^{-1}}$) that place it somewhat outside the 2σ disc ellipsoid. Also, due to its high galactic latitude, there is little contribution to these from radial velocity. ULAS J0926+0835 has a more poorly-constrained U and V, but may also be halo-like, with $U = 62 \pm 40$, $V = -140 \pm 46$ $\mathrm{km\,s^{-1}}$. The ± 100 $\mathrm{km\,s^{-1}}$ line for ULAS J0926+0835 intersects the disk rings, unlike ULAS J1319+1209. This means that ULAS J1319+1209 is the stronger halo candidate. The weaknesses associated with ULAS J0926+0835's candidature also highlights the need for radial velocities for these objects.

Of the remaining objects, the U and V components seem most likely to be within the thin disc range, including ULAS J1018+0725 (which supports its interpretation as a metal-rich object that has scattered into the sample). However, with the exception of Hip 73786B, the possibility of large radial velocity components for these objects prevents us from ruling them out as halo candidates.

It is interesting to note that the strongest halo candidates do not appear to be the bluest objects in the sample. In $J - K$, six other objects show a bluer colour but have more modest V_{tan} and apparently disc-like U and V. At any given spectral type, the combined effect of greater age (and thus higher gravity) and lower metallicity should result in bluer $J - K$ colours for substellar halo members than for the members of the younger disc population. Surprisingly, for both of the kinematic halo candidates several objects of similar spectral type are seen to be 2σ bluer in $J - K$. However, better photometry would be required to confirm this trend for the halo candidates.

2.8 ULAS J1504+0538, a binary companion to Hip 73786A

Scholz (2010a) identified Hip 73786B as a common proper motion companion to Hip 73786, a K5 dwarf at a distance of 19.2pc (Perryman *et al.* 1997). The selection for blue T dwarfs and kinematic analysis also independently identified this pair, and for completeness the analysis is described below.

The proper motion for the T dwarf was found to be $\mu_{\alpha cos\delta} = -627 \pm 160$ $\mathrm{mas\,yr^{-1}}$ and $\mu_{\delta} = -457 \pm 59$ $\mathrm{mas\,yr^{-1}}$. These values are consistent with both Scholz (2010a) and with Hip 73786. Thus this work supports the common association of these objects.

To control for the possibility of the objects being unassociated, but merely on the same portion of sky, a collaborator performed a random-alignment check; Day-Jones (priv.

Table 2.7: Properties of Hip 73786A.

Property	Value	Reference
R.A. (J2000.0)	15:04:53.5267	-
Dec. (J2000.0)	+05:38:17.150	-
Distance (pc)	19.2±0.7	a
Spectral type	K5	b
T_{eff}/K	4450±50	b
$\log g$	4.80±0.1	b
[Fe/H]	-0.30±0.1	b
B/mag	11.16±0.02	c
V/mag	9.85±0.02	d
R/mag	9.0±0.3	e
I/mag	8.2±0.3	e
J_{2MASS}/mag	7.26±0.02	f
H_{2MASS}/mag	6.66±0.02	f
K_{2MASS}/mag	6.47±0.02	f
$\mu_{\alpha cos\delta}/\mathrm{mas\,yr^{-1}}$	-606.8 ±1.8	a
$\mu_{\delta}/\mathrm{mas\,yr^{-1}}$	-507.6 ±1.8	a
$V_{\mathrm{rad}}/\mathrm{km\,s^{-1}}$	-68±10	g
$U/\mathrm{km\,s^{-1}}$	-48±7	-
$V/\mathrm{km\,s^{-1}}$	-75±7	-
$W/\mathrm{km\,s^{-1}}$	-44±8	-

[a]: Perryman *et al.* (1997)
[b]: Cenarro *et al.* (2007)
[c]: Weis (1993)
[d]: Evans (1967)
[e]: Monet *et al.* (2003)
[f]: Cutri *et al.* (2003) - 2MASS point-source catalog
[g]: Barbier-Brossat and Figon (2000)

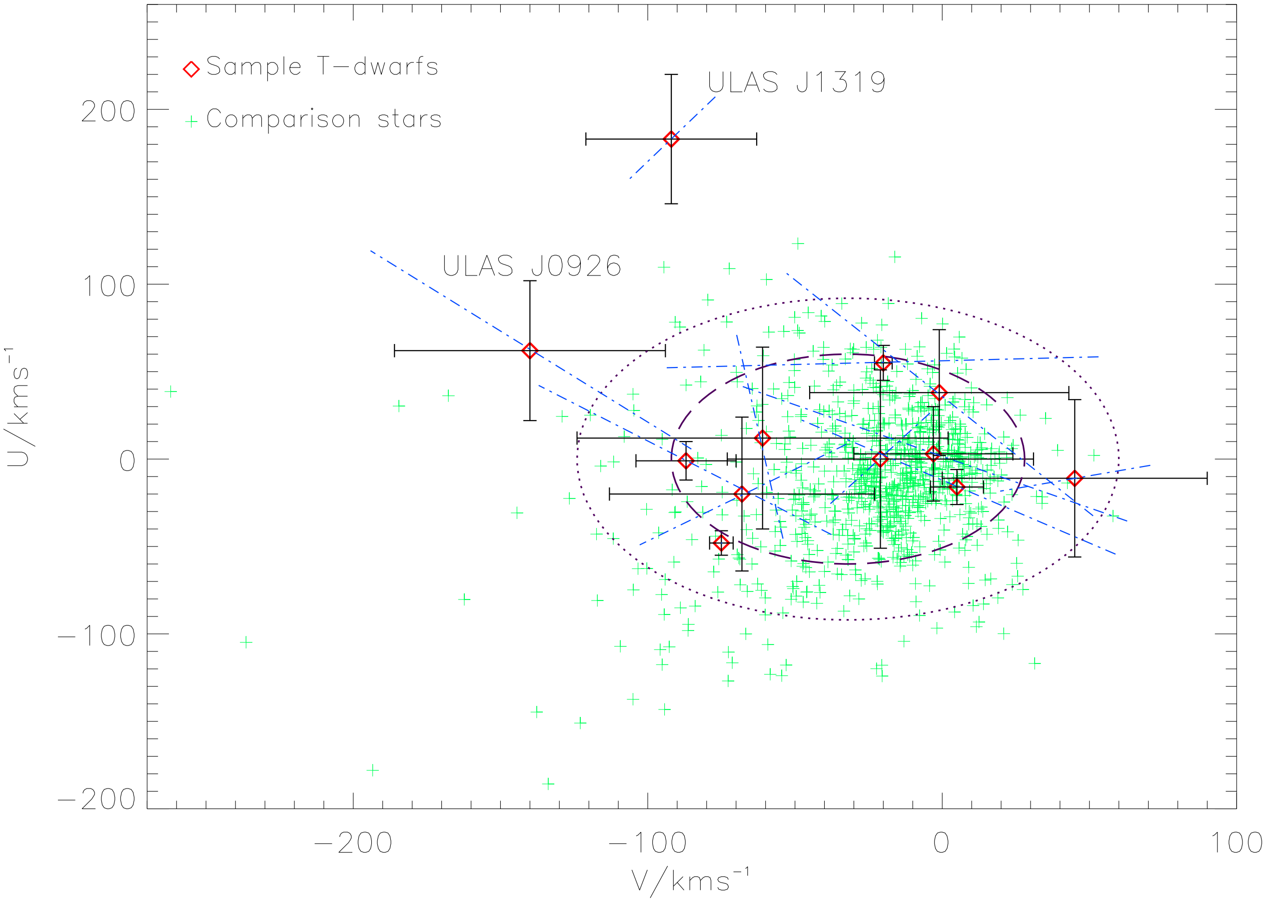

Figure 2.4: U and V components plotted for the sample (red diamonds) and a stellar background (green crosses). The stellar background is from Soubiran *et al.* (2008). Error bars are based on distance errors and proper motion errors. The purple dashed line marks the 1σ velocity ellipsoid for disc stars and the dotted line marks the 2σ disc ellipsoid (see Chiba and Beers 2000; Reid *et al.* 2001). The blue angled, dot-dashed lines represent U and V values in the cases that $V_{\mathrm{rad}} = \pm 100\ \mathrm{km\,s^{-1}}$ respectively.

comm.), published in Murray *et al.* (2011). For completeness, I summarise the method below:

The possibility is considered that the two components of Hip 73786B and Hip 73786A are simply randomly aligned on the sky with the same proper motions. To control for this, the method of Day-Jones *et al.* (2008) is used. This was begun by taking objects with proper motions ($>$10 $\mathrm{mas\,yr^{-1}}$) from SuperCOSMOS in a square degree of sky surrounding Hip 73786B. In this region of sky 29,249 objects had proper motions. These were then put onto a colour-magnitude diagram (B vs $B-R$) and selected only those with a consistent

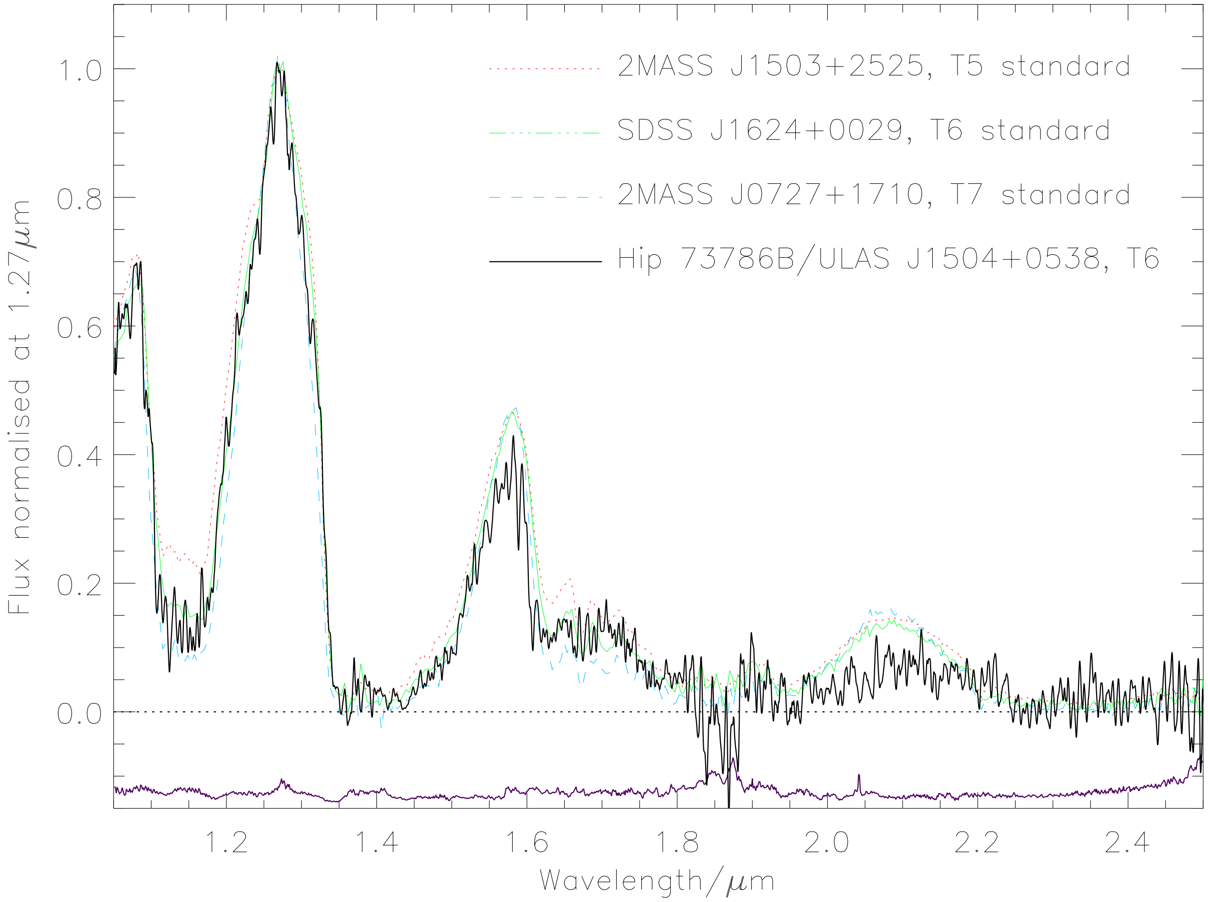

Figure 2.5: Spectrum for Hip 73786B, plotted along with T7, T6 and T5 standard spectra. The T7 and T6 spectra are from Burgasser *et al.* (2006a) and the T5 is from Burgasser *et al.* (2004). The thicker black line is the object spectrum. All spectra are normalised to 1.27μm and have been placed onto the object's wavelength scale. It can be seen that Hip 73786B's K-band is deeply depressed relative to the standards. Also, its H-band shows evidence for similar depression. The J-band shape is broadly similar to the standards, however. The error spectrum, the purple line at the bottom, has been offset by -0.15 for clarity.

magnitude to be at a common distance with Hip 73786B. Thirty-nine objects had colours and magnitudes consistent with being at the same distance as the T dwarf. These objects were then placed on a vector point diagram and compared their proper motion to that of Hip 73786B. None of the thirty-nine objects had proper motions consistent to within 2σ of the T dwarf, suggesting that the likely contamination of objects with the same distance and proper motion to Hip 73786B is <1/39.

Then the associated volume of space in which contaminant objects could be observed was calculated. Allowing for the possibility of unresolved binarity the range of plausible distances to the T dwarf is estimated as 18-31 pc. Considering the separation of $63.8''$, it is estimated that the pair of objects share a volume of $< 0.8\text{pc}^3$. As Hip 73786 is a K5 star, the number density of K type stars is considered; this is which is 0.0384 pc^{-3} (McCuskey 1983). Therefore it would be expected to observe $0.0384 \times 0.8 = 0.031$ K-type stars within this volume. Overall then, the chance of a spurious common proper motion main sequence companion to Hip 73786B is $< 7.9\times\ 10^{-4}$. Thus, < 0.15 such spurious companions are expected amongst the entire, ∼200 strong, sample of published T dwarfs. Therefore it seems reasonable to conclude that Hip 73786B and Hip 73786A are a genuinely-associated system of common origin, confirming the analysis of Scholz (2010a)

2.8.1 Composition, age and radial velocity of Hip 73786B

The two objects' apparent separation is 63.8". At a distance of 19.2 pc this corresponds to a projected separation of $\sim$ 1230 AU. Considering also the probabilities discussed above, I assume that the two objects share a common origin, being either a binary or a co-moving pair. I also posit the working assumption that common formation history implies a common composition between Hip 73786A and Hip 73786B, allowing for tighter constraints on the T dwarf's physical characteristics.

Hip 73786 is known to have a metallicity of $[\text{Fe/H}] = -0.3 \pm 0.1$ (Cenarro *et al.* 2007), clearly identifying it as a metal-poor star. Although this metallicity remains within the thin disc range of $[\text{Fe/H}] = -0.4$ to $+0.3$ (Nissen 1999), nonetheless this would suggest that Hip 73786B represents a new metal-poor T dwarf benchmark. The metallicities in Cenarro *et al.* (2007) were computed through a spectral synthesis method, by comparison to a large library of flux-calibrated stellar spectra.

As Hip 73786A has a radial velocity v_{rad} = -68±10 $\text{km}\,\text{s}^{-1}$ (Barbier-Brossat and Figon 2000), UVW space motion components were calculated. It is found that $U = -47.9 \pm 6.6$ $\text{km}\,\text{s}^{-1}$, $V = -74.7 \pm 6.5$ and $W = -43.9 \pm 8.4$.

Hip 73786A shows some evidence of chromospheric activity. Gray *et al.* (2003) list a value of $\log R'_{\text{hk}} = -4.76$ for the primary. Mamajek and Hillenbrand (2008) gives a relationship between $\log R'_{\text{hk}}$ and stellar age. Using this and the value from Gray *et al.* (2003), an age of 2.0 Gyr is estimated for Hip 73786A. However, several factors can affect $\log R'_{\text{hk}}$. Henry *et al.* (1996) list binarity as one such factor, and there is a suggestion in Luyten (1979) that Hip 73786A may itself be a close binary, although no other references exist to support this. Also, with regard to the Sun, the value of $\log R'_{\text{hk}}$ varies depending on the point in the solar cycle at which it is measured. The Sun can vary between an estimated extreme of -5.10 during solar minimum to a peak of -4.75 during solar maximum (Henry *et al.* 1996). These fluctuations correspond to an age in the range of 2.2 to 8.0 Gyr, as opposed to the actual value of 5 Gyr. With only one available measurement, it is unknown whether or not Hip 73786A presents a similar activity cycle. If it does, then the example of the Sun shows that the age of the Hip 73786 system may be different from the estimated value.

Another possible source of uncertainty here is that Jenkins *et al.* (2008) find an offset of ∼0.1 dex between their analysis of typical FGK dwarfs and those of Gray et al. Jenkins et al. also show this offset is present in cross-matched samples of FGK stars between Gray et al. and Henry et al. Since this appears to be a systematic offset this correction can be applied to the value of Hip 73786A found by Gray et al. Using this correction would suggest a $\log R'_{\rm hk} = -4.66$ for Hip 73786A, which in turn feeds through to an age estimate of $\sim$ 1.6 Gyr, slighter lower than the adopted age if the Gray *et al.* (2003) value is accepted as given.

Holmberg *et al.* (2009) find a mean [Fe/H]$= -0.24$ for stars older than 4.0 Gyr. The age-velocity relation they find would also suggest an age >8 Gyr for the Hip 73786 system. These factors may suggest an older age than the one derived through chromospheric activity. However, both of these relations are subject to a large amount of scatter and kinematic relations are best applied to populations, not individual objects. The metallicity could also be consistent with an age below 4.0 Gyr, which limits the usefulness of this property for age determination. Therefore it is suggested that the Hip 73786 system has a minimum age constraint of 1.6 Gyr, but I am currently unable to estimate an upper limit.

As a control for the possibility of unresolved binarity of Hip 73786A, high-resolution imaging was undertaken by Dr Nicholas Lodieu (Lodieu, priv. comm.; published in Murray *et al.* [2011]). As this has a bearing on the age-estimate results, I summarise details of the observations here. Observations were carried out with FastCam, the 'Lucky Imaging' facility (Oscoz *et al.* 2008) installed as a common-user instrument on the Carlos Sánchez Telescope in the Teide Observatory, Tenerife, Canary Islands. FastCam is equipped with a low read-out noise L3CCD Andor 512×512 camera with a pixel scale of 42.2 mas, yielding a field-of-view of approximately 21.6 by 21.6 arcsec.

Hip 73786 was observed on 24 July 2010 in the I-band filter under a natural seeing of 1.0 arcsec, clear conditions, and full moon. The total exposure time was divided up into 1000 images of 50ms repeated five times. The achieved resolution is of the order of 0.2 arcsec, corresponding to a projected physical separation of less than 4 AU, assuming a distance of 19 pc for the target (Perryman *et al.* 1997). The data reduction of the raw images was done with the automatic pipeline distributed by the FastCam team and developed by the Universidad Polytécnica de Cartagena[1]. This reduction involves bias and flat-field correction and the best 15% exposures were selected to achieve a near to diffraction-limited image. From this analysis no companion is found at the observed resolution around Hip 73786 down to 4-5 mag at a separation of 1 arcsec from the target.

---

[1] Details on FastCam at http //www.iac.es/proyecto/fastcam/

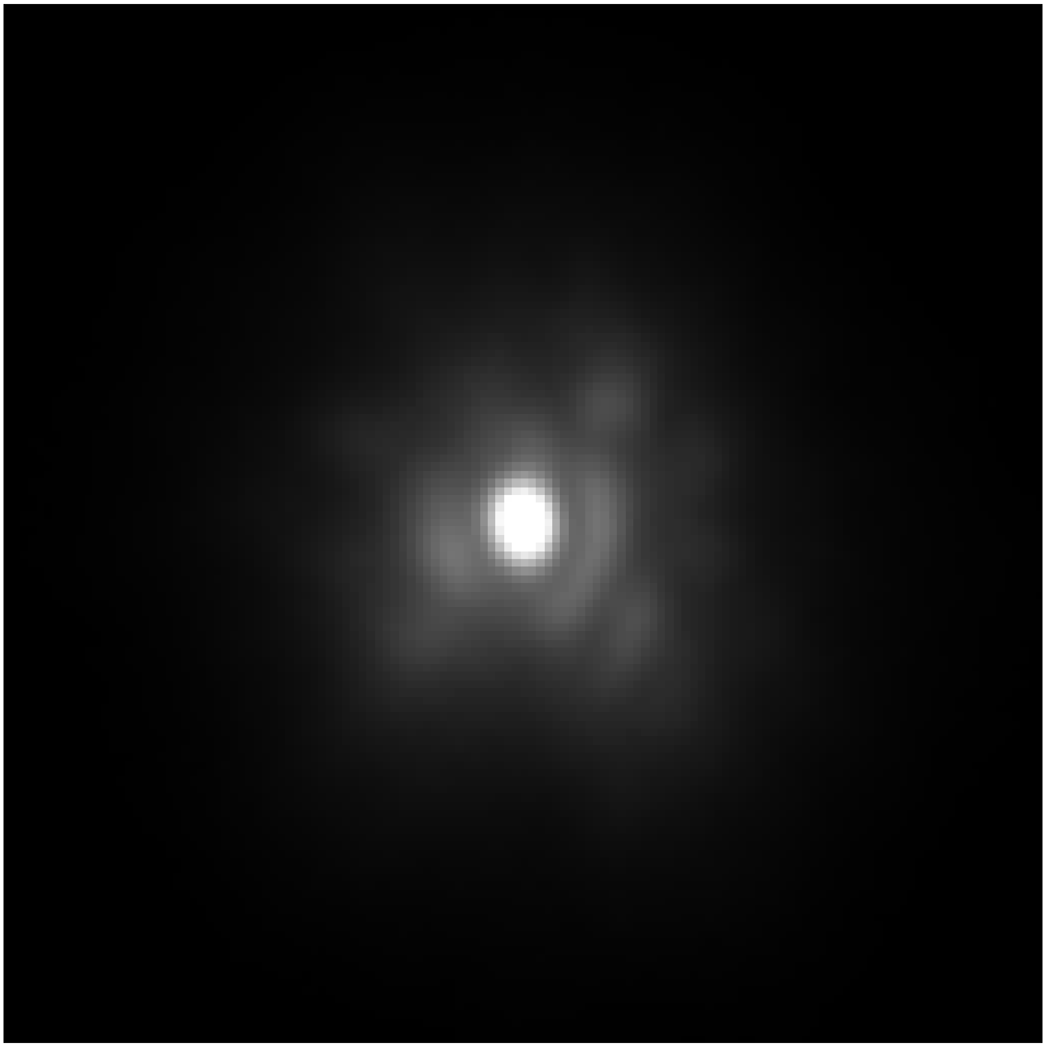

Figure 2.6: Image of HIP 73786A taken in the I-band filter with FastCam installed on the Carlos Sánchez Telescope in the Teide Observatory. The pixel scale 42.2 mas and the field-of-view is 2.7 by 2.7 arcsec aside. East is left and North is up. No companion is detected around HIP 73786 up to 10 arcsec from the primary using the 15% and 50% of the images.

2.9 Selections Summary

I present data for twelve UKIDSS T dwarfs, including 11 from DR4 and one object from DR5. I use follow-up data to compute proper motions and tangential velocities, and find a range of values, ULAS J0926+0835 and ULAS J1319+1209 with $V_{\rm tan} > 100$ km s^{-1}, which may be indicative of halo kinematics. Confirmation or definitive rejection of these objects will need measurements of $V_{\rm rad}$ and calculation of full UVW space motions.

Spectra are presented for all candidates. Spectral typing is undertaken on all of them using the scheme of Burgasser *et al.* (2006a). A ±2 subtype variance is noted on the indices of some of the objects.

Hip 73786B from UKIDSS DR5 is confirmed to be associated with the K5 dwarf Hip 73786A, and it is found to be a T6p dwarf. Hip 73786B is found to be at least 1.6 Gyr old, constrained by chromospheric activity in the primary. As Hip 73786A is known to be of low metallicity, this system represents and important addition to the sample of T dwarf benchmark systems. It is noted that one object (ULAS J1018+0725) appears to be a metal-rich or low-gravity, disc dwarf that has scattered into the sample. Of the rest, I find two objects with kinematic evidence suggestive of halo membership (ULAS J0926+0835 and ULAS J1319+1209). Most interestingly I note that our bluest objects are not the best halo candidates, although the current velocity and colour uncertainties means this observation is only suggestive and must be verified with more precise proper motion and radial velocity measurements.

Chapter 3

T dwarfs that are unusual in the mid-infrared

3.1 Red $H - W2$ outliers

In this chapter I look in particular at three T dwarfs with unusual mid-infrared properties. These objects are BD+01^o 2920B, 2MASS J0939-2448 and ULAS J1416+1348B. All of them have very red $H - W2$ colours; I investigate whether or not metallicity and/or surface gravity may be playing a role in these colours, and if so, whether it is the only factor. This chapter will form the basis for a paper that is to be submitted to *MNRAS* in January 2013.

3.2 New spectra for 2MASS J0939-2448 and ULAS J1416+1348B

3.2.1 Data reduction

2MASS J0939-2448 was observed on the Folded Infrared Echelleport Spectrograph (FIRE; see Simcoe *et al.* 2008) on the Baade 6.5 metre telescope, during February 2011. FIRE is an instrument with two modes, a longslit mode with low resolution ($R \sim 250 - 300$) and a cross-dispersed echellette mode with a medium resolution ($R \sim 6000$). Spectra are imaged via a HAWAII-2RG chip, which has continuous coverage between 0.85 to 2.5μm. When in echelle mode, the object spectrum is spread across 21 orders; these have some overlap in coverage at the ends of each order. Acquiry of targets is done using a second NIR imager and a $J_{\rm MKO}$-band filter focused on the entry slit. Eight 243-second exposures were obtained for 2MASS J0939-2448 using FIRE's echelle mode. The 0.60" slit was used, and the airmass was 1.053 at the time of the observations. The exposures were taken using an ABBA dither pattern. An AOV star, HIP 87727, was observed for telluric calibration. Quartz flat-fields and thorium-argon (ThAr) arcs were obtained along with the science data.

The data were reduced using the FIREHOSE pipeline, which is a package based on the MASE pipeline (Bochanski *et al.* 2009). FIREHOSE is intended to reduce cross-dispersed echelle spectra that have curved orders. Quartz lamp images were used to find the order boundaries and to derive illumination corrections and a flat-field file for the spectrum. The wavelength solution was determined using ThAr arc frames, and also the tilt of each order in the spatial direction. Telluric corrections were undertaken using the *xtellcor* tool from Spextool (see Cushing *et al.* 2004; Vacca *et al.* 2003). The telluric absorption was measured by comparing the telluric standard's spectrum to a Vega spectrum reddened with the $B - V$ color of the standard and broadened using the 1.005μm H I line as a line kernel. This step also flux-calibrated the science images; after this step, multiple science images were combined together. The resulting spectrum can be seen in Figure 3.1.

ULAS J1416+1348B was also observed on FIRE, during May 2012. Eight 243-second exposures were obtained for ULAS J1416+1348B using FIRE's echelle mode. The 0.60" slit was used, and the airmass was 1.36 at the time of the observations. The exposures were taken using an ABBA dither pattern. The A0V star HIP 68868 was used for telluric correction observations. Quartz flat-fields and thorium-argon (ThAr) arcs were obtained along with the science data

The data were reduced using the FIREHOSE pipeline, in the same manner as described for 2MASS J0939-2448. The resulting spectrum is shown in Figure 3.3. Both resultant spectra are of $R \sim 5000$; no smoothing has been applied to either plot.

3.2.2 Radial velocity of ULAS J1416+1348B

FIRE's intermediate resolution is adequate to allow the determination of radial velocities. With this in mind, I apply the method of Bochanski *et al.* (2011) to the spectrum for ULAS J1416+1348B. The object spectrum is cross-correlated against a set of models. Both model and object spectra are on vacuum wavelengths and heliocentric corrections have been applied as appropriate for the time and date of the observations. The model spectra are from the BTSettl grid (Allard and Freytag 2010), and have effective temperatures ranging from 500K to 1400K. All the model spectra used had solar metallicity and $\log g = 5.0$. The spectra were cross-correlated across the peak of the J-band, as this region

Table 3.1: Radial velocities for ULAS J1416+1348B.

Model T_{eff}	Radial velocity/km s^{-1}
500 K	-40.8
550 K	-40.9
600 K	-41.8
650 K	-39.8
700 K	-39.2
750 K	-38.7
800 K	-38.9
850 K	-39.6
900 K	-39.1
950 K	-38.9
1000 K	-38.9
1100 K	-38.3
1200 K	-38.3
1300 K	-40.9
1400 K	-41.1

Radial velocities as derived using a series of model spectra. All model spectra are for solar metallicity and $\log g = 5.0$.

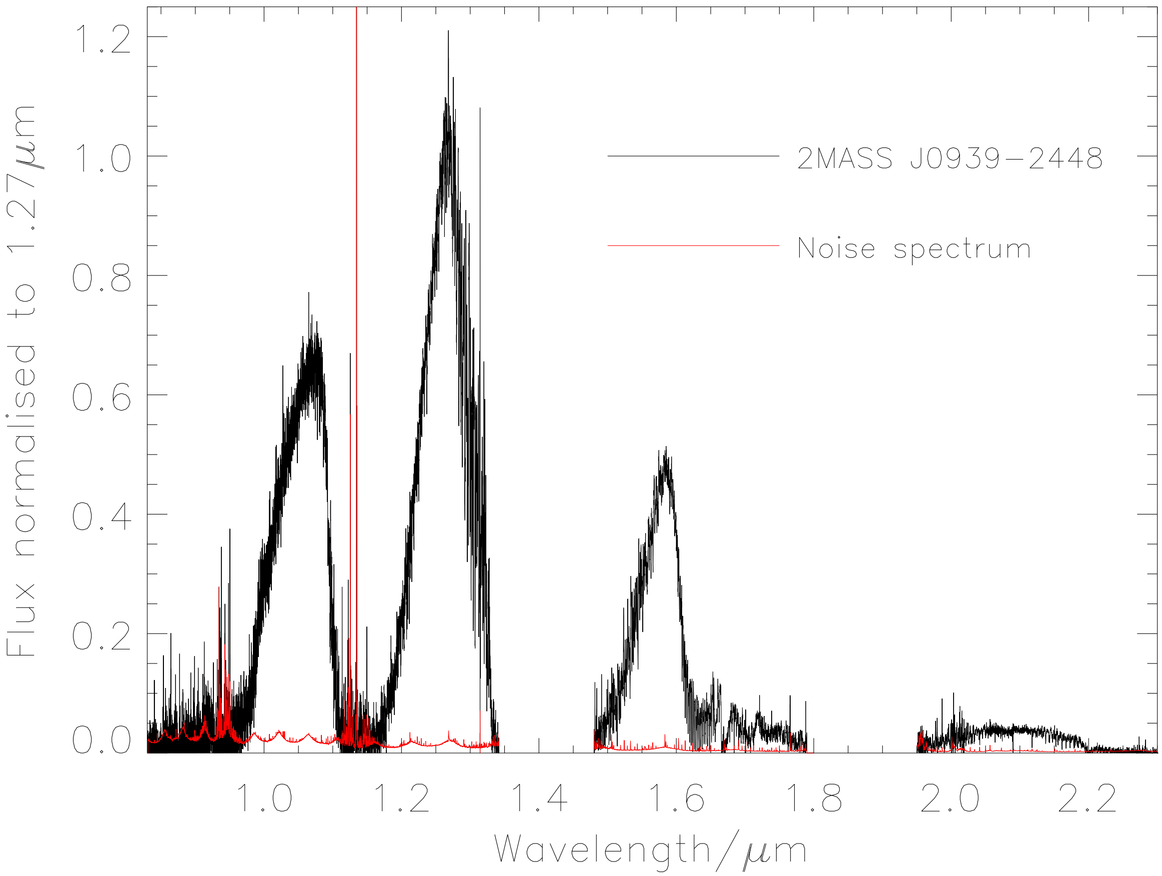

Figure 3.1: A FIRE medium-resolution spectrum for the T8 object 2MASS J0939-2448. The object is shown in black, the error spectrum in red.

contains lots of prominent molecular lines. The specific wavelength-region used was 1.27μm to 1.31μm. This region of the object and mode. The derived velocity was taken as the median of the returned set; see Table 3.1 for the individual results. The error was taken as the standard deviation of the set. From this, I find that the radial velocity for ULAS J1416+1348B is $-39 \pm 1\,\mathrm{kms}^{-1}$, which is consistent with the value derived by Bowler *et al.* (2010), $V_{\mathrm{rad}} = -38 \pm 10\mathrm{km\,s}^{-1}$, for the L-dwarf primary. The similarity of radial velocity confirms that the two objects are physically-associated. The radial velocity calculations are heliocentric.

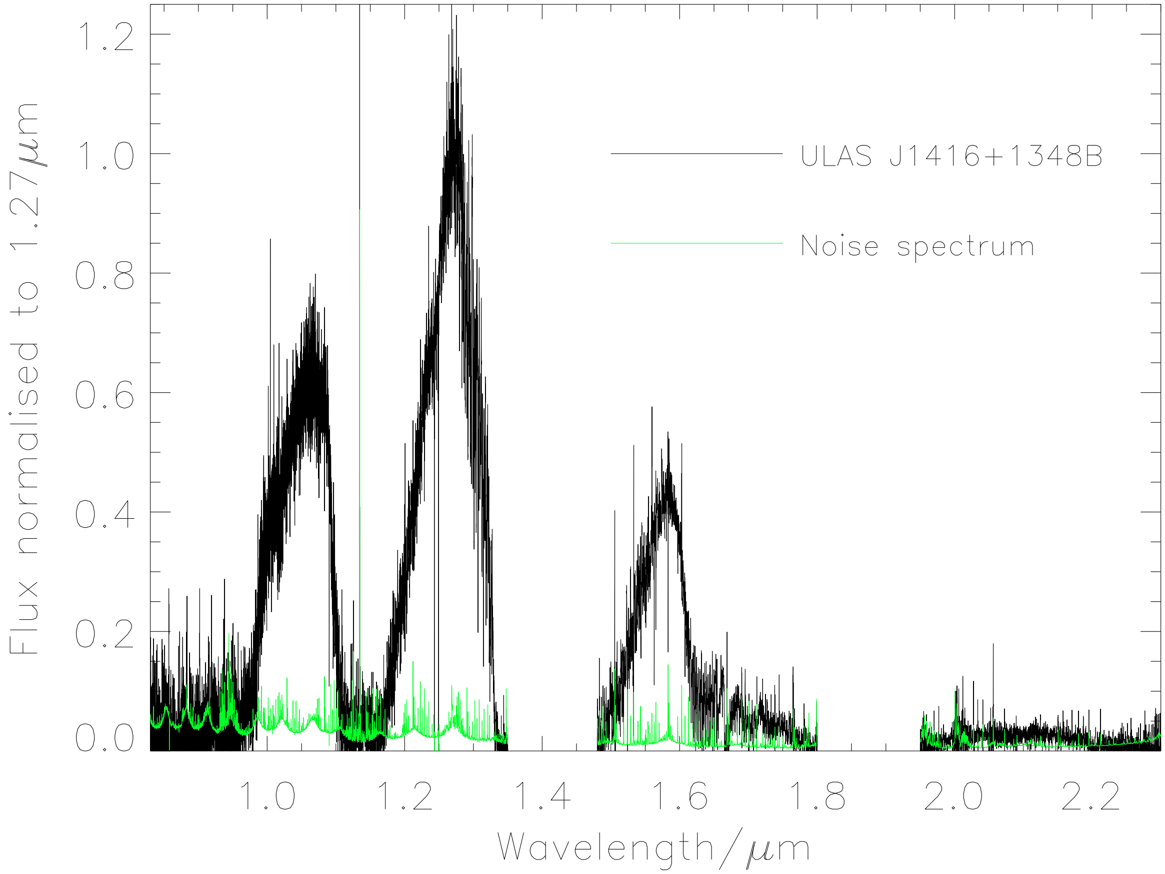

Figure 3.2: A FIRE medium-resolution spectrum for the T7.5 object ULAS J1416+1348B. The object is shown with flux normalised to the peak of the J-band and accompanied by an error spectrum, shown in green.

3.3 T dwarfs in $H - W2$

3.3.1 Mid-infrared Colours

Obtaining the photometry of T dwarfs in the mid-infrared is a crucial first step towards understanding their physical properties. Colour trends have been identified by previous work (see for instance Leggett *et al.* 2010). These works have identified $H - [4.5]$ as a $T_{\rm eff}$ proxy. While cross-matching a sample of UKIDSS T dwarfs against the WISE database, several objects were noted to have very red $H - W2$ colours as compared to their spectral types. Data quality did not appear to be the cause of this redness; these objects' $W2$ photometric errors are no greater than those of T dwarfs in general. This raises the possibility that composition or unresolved binarity could be a root cause. (Table 3.2

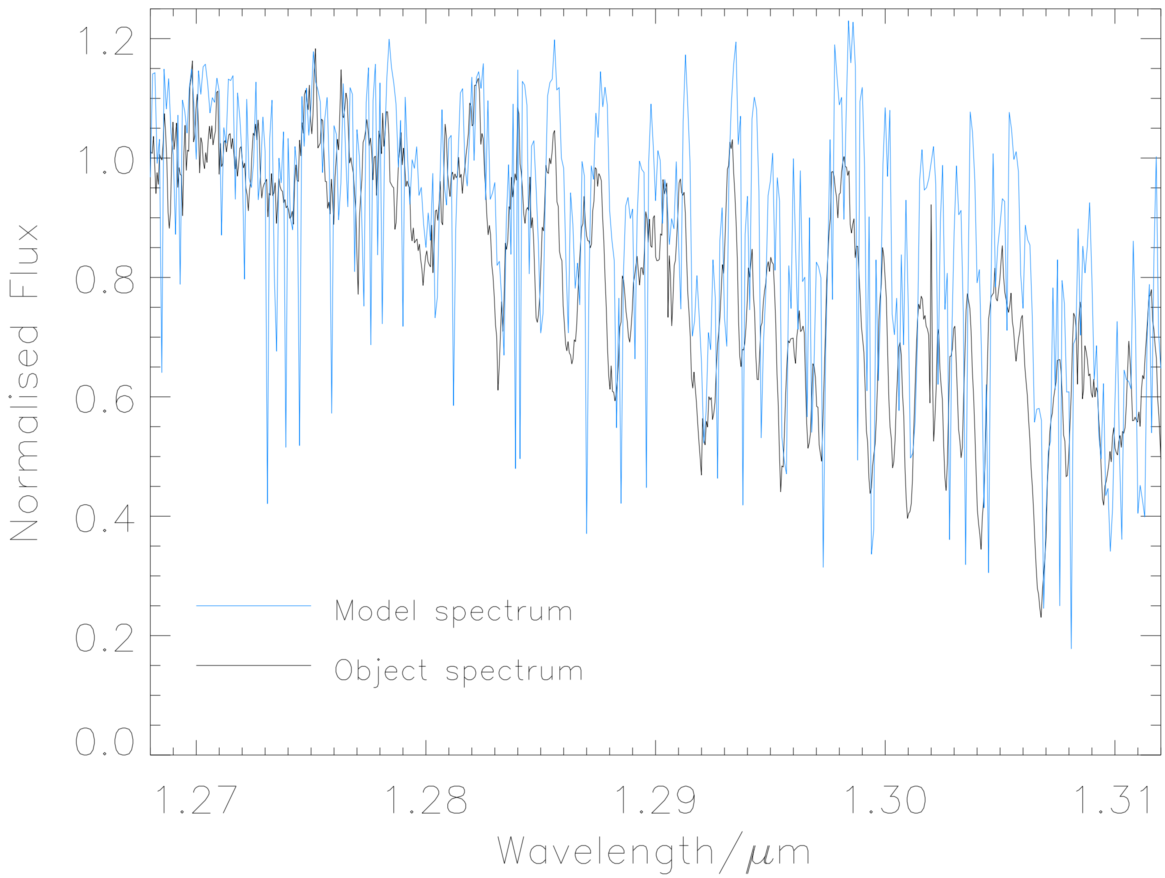

Figure 3.3: ULAS J1416+1348B, shown in black, across the 1.27μm to 1.31μm correlation region. Shown with the object is a BTSettl model spectrum for $T_{\rm eff} = 800\,$K, with $\log g = 5.0$ and [m/H]$= -0.3$.

shows the photometry for three red outliers - BD+01^o 2920B, 2MASS J0939-2448 and ULAS J1416+1348B - as compared to several known and suspected low-metallicity T dwarfs.)

3.3.2 Transform

ULAS J1416+1348B and 2MASS J0939-2448 have also shown very red $H - [4.5]$ colours, raising the possibility that they are akin to the red $W2$ outliers. ULAS J1416+1348B is in the area covered by the WISE data release, however it is unresolved from its L-dwarf companion in the survey images. Consequently, although the photometry tables return a $W2$ value for it, this magnitude will be subject to contamination from the L dwarf and will be unreliable. IRAC Channel 2 (4.5μm) is similar in wavelength and filter profile to

Table 3.2: $H - W2$ for blue and metal-poor T dwarfs.

Object	Type	H	$W2$	$H - W2$	Ref
HIP 38939b	T4.5	15.9±0.1	13.82±0.04	2.08±0.11	1, 9
ULAS J1501+0822	T5.0	18.32±0.02	15.95±0.23	2.37±0.23	2, 8
ULAS J0842+0936	T6.0	18.84±0.02	16.2±0.3	2.6±0.3	3, 8
HIP 73786b	T6.0	17.05±0.04	14.27±0.02	2.78±0.04	4, 9
ULAS J1416+1348B	T7.5	17.62±0.03	12.75±0.03	4.87±0.04	5, 8
BD+01^o 2920B	T8.0	19.1±0.20	14.76±0.09	4.34±0.22	6, 6
2MASS J0939-2448	T8.0	15.94±0.09	11.64±0.04	4.30±0.1	7, 9

Spectral type, H-band MKO magnitudes, $W2$ magnitudes and $H - W2$ for a selection of metal-poor benchmark T dwarfs and candidate metal-poor field dwarfs with $W2$-magnitudes. As can be seen, the red colours of the $H - W2$ outliers do not appear to be attributable solely to photometric scatter. In the references column, the first number refers to the discovery and near-infrared magnitudes and the second refers to the mid-infrared magnitude. 1) is Deacon *et al.* (2011), 2) is Pinfield *et al.* (2008), 3) is Burningham *et al.* (2010a), 4) is Scholz (2010a), 5) is Burningham *et al.* (2010b), 6) is Pinfield *et al.* (2012), 7) is Tinney *et al.* (2005), 8) is this work and 9) is Kirkpatrick *et al.* (2011).

$W2$, allowing the creation of a transform between the two magnitudes. This similarity can be seen in Figure 3.4, where the difference between $H - W2$ and $H - [4.5]$ is shown for a set of 21 T dwarfs, where all have both magnitudes.

From this set of T dwarfs (their individual colours are listed in Table 3.3) a linear relation was found such that:

$$W2 = [4.5] - (0.01 \pm 0.02) \tag{3.1}$$

The error on the constant reflects the standard deviation of the mean for the photometric errors in $W2 - [4.5]$.

From this transform, I find a $W2$ magnitude of 12.75±0.03 for ULAS J1416+1348B, not greatly different from its [4.5] value of 12.76±0.03 from Burningham *et al.* (2010b).

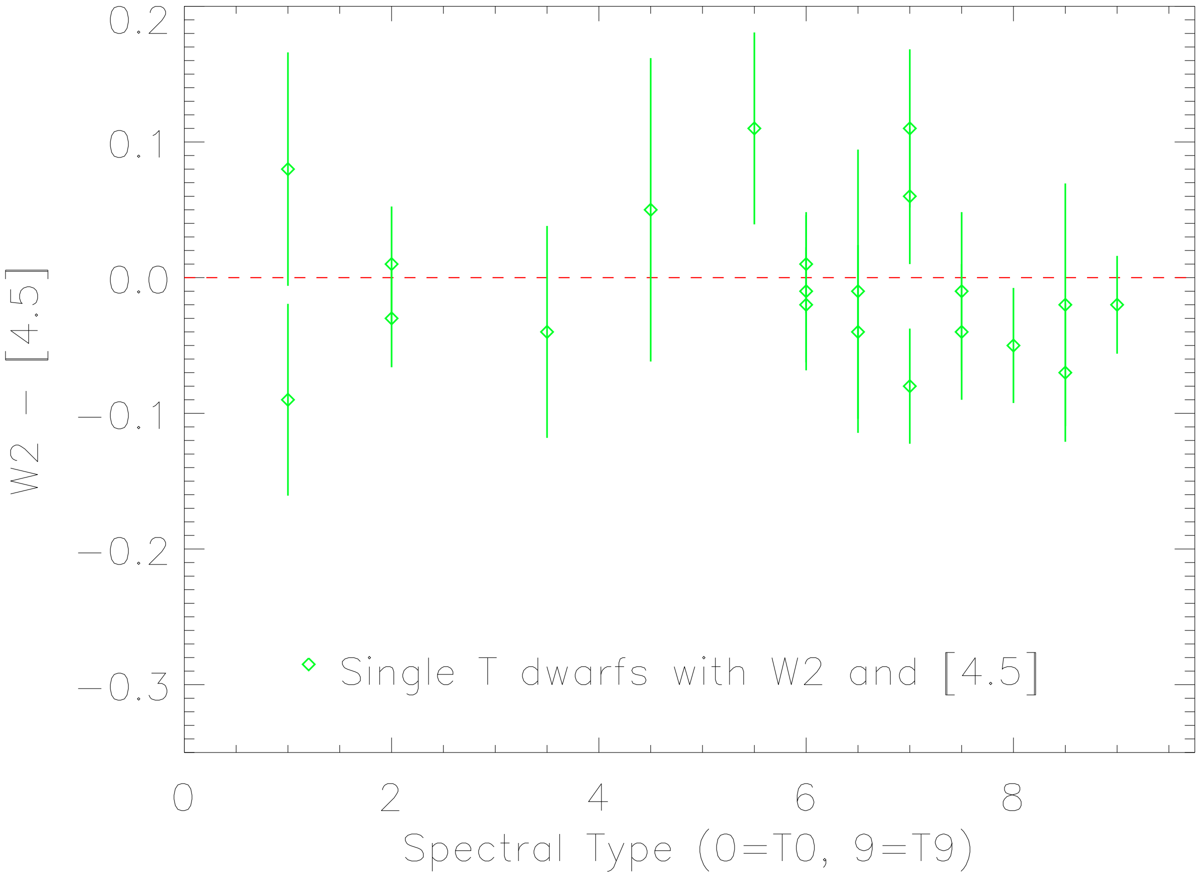

Figure 3.4: This plot shows the difference between $H - W2$ and $H - [4.5]$ for all 21 objects where both colours have been observationally-measured.

Table 3.3: Table showing spectral types, $H_{\rm mko}$ and $W2$ photometry for T dwarfs in WISE and UKIDSS.

Object Name	Type	$H_{\rm mko}$	$W2$	Ref (Disc., $W2$)
ULAS J003402.77-005206.7	T8.5	18.49±0.04	14.47±0.08	1, 23
ULAS J015024.37+135924.0	T7.5	18.11±0.02	15.2±0.1	2, 23
SDSS J015141.69+124429.6	T1.0	15.54±0.05	13.82±0.05	3, 23
2MASSI J0243137-245329	T6.0	15.39±0.03	12.93±0.03	4, 23
SDSS J020742.48+000056.2	T4.5	16.66±0.05	15.0±0.1	3, 23
SDSS J032553.17+042540.1	T5.5	16.25±0.03	13.78±0.05	5, 23
SDSS J035104.37+481046.8	T1.0	15.81±0.05	13.90±0.05	5, 23
2MASS J0415195-093506	T8.0	15.70±0.03	12.24±0.03	4, 23
SDSS J042348.57-041403.5AB	T0.0	13.51±0.03	11.57±0.02	3, 23
WISEPC J045853.89+643452.9	T9.0	17.4±0.3	13.02±0.03	6, 23
2MASS J05591914-1404488	T4.5	13.64±0.03	11.90±0.02	7, 23
UGPS J072227.51-054031.2	T9.5	16.90±0.00	12.20±0.03	8, 23
2MASSI J0727182+171001	T7.0	15.67±0.03	12.93±0.03	4, 23
SDSS J073922.26+661503.5	T1.5	16.31±0.03	14.53±0.06	5, 23
SDSS J074149.15+235127.5	T5.0	16.12±0.05	14.11±0.05	9, 23
SDSS J074201.41+205520.5	T5.0	15.95±0.03	13.71±0.04	9, 23
2MASS J0755480+221218	T5.0	15.70±0.03	13.50±0.04	10, 23
Hip 38398B	T4.5	16.03±0.08	13.82±0.04	11, 23
SDSS J075840.33+324723.4	T2.0	14.21±0.03	12.17±0.03	9, 23
SDSS J083048.80+012831.1	T4.5	16.17±0.03	14.05±0.05	9, 23
SDSSp J083717.22-000018.3	T1.0	16.21±0.05	14.68±0.07	12, 23
ULAS J0842+0936hb	T6.0	18.84±0.02	16.2±0.3	2, 23
SDSS J085834.42+325627.7	T1.0	15.45±0.03	13.46±0.04	5, 23
SDSS J090900.73+652527.2	T1.5	15.32±0.03	13.42±0.05	5, 23
SDSS J092615.38+584720.9	T4.5	15.42±0.03	13.66±0.04	3, 23
2MASSI J0937347+293142	T6.0	14.67±0.03	11.65±0.02	4, 23
2MASS J0939548-2448279	T8.0	15.94±0.09	11.64±0.02	13, 23
SDSS J111010.01+011613.1	T5.5	16.22±0.05	13.99±0.05	3, 23
2MASSI J1217110-031113	T7.5	15.97±0.03	13.19±0.04	14, 23
2MASS J12373919+6526148	T6.5	15.9±0.1	12.92±0.03	14, 23
SDSSp J125453.90-012247.4	T2.0	14.13±0.03	12.40±0.03	12, 23
ULAS J133553.45+113005.2	T8.5	18.25±0.01	13.84±0.05	15, 23
SDSSp J134646.45-003150.4	T6.5	15.84±0.05	13.56±0.04	16, 23
BD+01^{o} 2920B	T8.0	19.0±0.2	14.76±0.09	17, 17
SDSS J143553.25+112948.6	T2.0	16.52±0.04	14.17±0.06	5, 23
SDSS J143945.86+3042220.6	T2.5	16.53±0.03	14.70±0.08	5, 23
Gl 570D	T7.5	15.28±0.05	12.11±0.03	7, 23
ULAS J150135.33+082215.2	T4.5	18.30±0.04	15.9±0.2	18, 23
2MASS J15031961+2525196	T5.0	13.90±0.03	11.69±0.03	19, 23
Hip 73786B	T6.0	17.05±0.04	14.27±0.06	20, 23
SDSS J150411.63+102718.4	T7.0	16.92±0.03	14.12±0.05	5, 23
SDSS J151114.66+060742.9	T0.0	15.16±0.03	13.15±0.03	5, 23
SDSS J151603.03+025928.9	T0.0	16.07±0.05	14.03±0.06	9, 23
SDSS J151643.01+305344.4	T0.5	15.86±0.03	13.32±0.03	5, 23
SDSS J152039.82+354619.8	T0.0	14.56±0.03	12.89±0.03	5, 23
SDSS J152103.24+013142.7	T2.0	15.63±0.03	13.95±0.04	9, 23
SDSS J153417.05+161546.1AB	T3.5	16.37±0.03	14.41±0.05	5, 23
2MASS J1534498-295227AB	T5.5	14.74±0.03	12.56±0.03	4, 23
ULAS J154427.34+081926.6	T3.5	18.49±0.03	15.7±0.2	18, 23
2MASS J1553022+153236	T7.0	15.76±0.03	13.02±0.03	4, 23
WISEPC J161705.75+180714.3	T8.0	18.27±0.08	14.03±0.06	21, 23
SDSS J162414.37+002915.6	T6.0	15.48±0.05	13.07±0.03	22, 23
SDSS J162838.77+230821.1	T7.0	16.63±0.03	13.92±0.04	5, 23
SDSS J163022.92+081822.0	T5.5	16.35±0.03	14.34±0.06	5, 23
SDSS J163239.34+415004.3	T1.0	16.42±0.07	15.28±0.09	9, 23
SDSS J175024.01+422237.8	T2.0	15.57±0.03	13.97±0.04	9, 23
SDSS J175032.96+175903.9	T3.5	15.94±0.05	14.42±0.06	3, 23
SDSS J175805.46+463311.9	T6.5	16.20±0.03	13.79±0.03	9, 23
WISEPC J181210.85+272144.3	T8.5	18.87±0.06	14.15±0.05	21, 21
WISEPC J235941.07-733504.8	T5.5	16.11±0.04	13.26±0.04	21, 21

The objects are shown in order of R.A. In the references column, the first number refers to the discovery paper and the second number refers to the source for the $W2$-magnitude. The references for the numbers are as follows:
1) is Warren *et al.* (2007); 2) is Burningham *et al.* (2010a); 3) is Geballe *et al.* (2002);
4) is Burgasser *et al.* (2002); 5) is Chiu *et al.* (2006); 6) is Mainzer *et al.* (2011);
7) is Burgasser *et al.* (2000); ; 8) is Lucas *et al.* (2010); 9) is Knapp *et al.* (2004); 10) is Cushing *et al.* (2011);
11) is Deacon *et al.* (2011); 12) is Leggett *et al.* (2010); 13) is Tinney *et al.* (2005); 14) is Burgasser *et al.* (1999);
15) is Burningham *et al.* (2008); 16) is Tsvetanov *et al.* (2000); 17) is Pinfield *et al.* (2012); 18) is Pinfield *et al.* (2008);
19) is Burgasser *et al.* (2003); 20) is Scholz (2010a); 21) is Burgasser *et al.* (2011);
22) is Strauss *et al.* (1999); and 23) is Kirkpatrick *et al.* (2011)

3.3.3 Red outliers in $H - W2$

Figure 3.5 shows a plot of $H - W2$ against spectral type. The $H - W2$ colour remains roughly flat until around spectral type T4. After type T4, the colour displays a trend of reddening with spectral type through to T9.5. At later types, the dispersion in the colour appears greater than at earlier types. The red outliers are also marked on this plot. These are ULAS J1416+1348B (T7.5), 2MASS J0939-2448 (T8.0) and BD+01^{o} 2920B (T8; see

Pinfield *et al.* 2012) is very red, although it is not the most extreme T8 object.

BD+01^o 2920B is known to be metal-poor, due to its association with the companion star BD +01^o 2920A (Pinfield *et al.* 2012), with an estimated value of [Fe/H]= -0.38. It and ULAS J1416+1348B have been identified as metal-poor objects. The similarities of the two objects' Y-bands (see Figure 3.10) confirms that both objects are of subsolar metallicity. In their cases, it is possible that their $H-W2$ colours may be being reddened by metallicity and/or surface gravity effects.

However, it appears that metallicity is not the only factor to affect this plot. Also shown are the T6 benchmark Hip 73786B (Scholz 2010a) and the T4.5 benchmark Hip 38939B (Deacon *et al.* 2011). Both of these benchmarks are known to be metal-poor, as inferred from their companion stars. Hip 73786B has [Fe/H]= -0.3 ± 0.1 (Murray *et al.* 2011) and Hip 38939B has [Fe/H]= -0.24 ± 0.07 (Deacon *et al.* 2011). Despite this, these objects do not possess notably-red $H-W2$.

3.4 Distance of the ULAS and SDSS J1416+1348 system

For this work, I have used a new distance measurement for for SDSS J1416+1348A and ULAS J1416+1348B. This measurement, and the astrometric observations and image reduction procedures associated with it, were undertaken by Ricky Smart (Smart, priv. comm.). I include a description of the observations and analysis for the parallax here as the value is important to my later analysis.

The astrometric observations and image reduction procedures were identical to those described in Smart *et al.* (2010). The first UKIDSS images of SDSS J1416+1348A were taken on 2008/05/12 which also act as the discovery images for ULAS J1416+1348B. The parallax observations for these objects began on the 2009/06/17 but as the original observations had the objects very close to the edge of chip #2 it was decided it was better to change the pointing slightly to have a more uniform distribution of reference stars. This means the first frame is on a different system and the solution has been tested with and without the first frames. Using the first frame the solutions of the two objects are both smaller and differ by a larger amount even though the errors are smaller. As small field parallax determinations rely on the stability of the local astrometric system it has been preferred to use only observations with the same pointing. If it is possible to model the astrometric differences sufficiently the solution will be improved, with the final value which will come out at the end of the UKIRT parallax program currently scheduled for

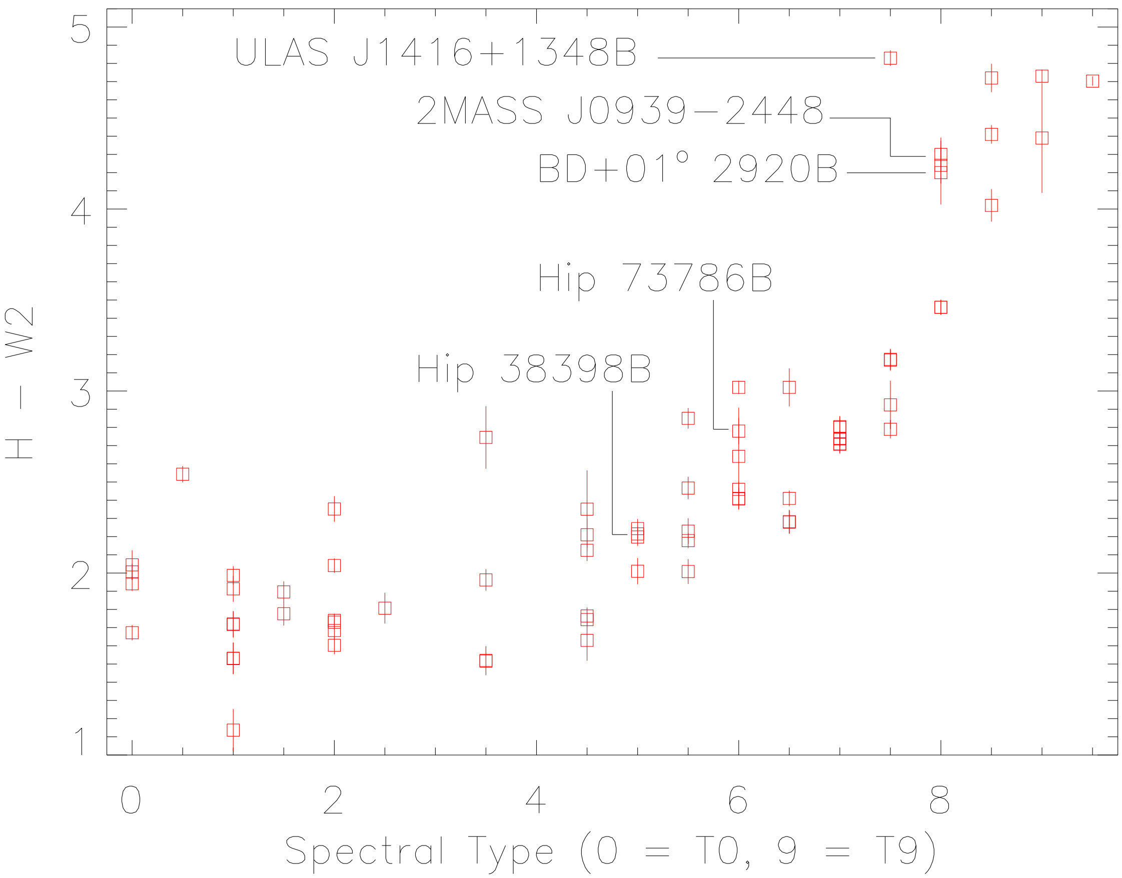

Figure 3.5: A plot showing spectral type against $H-W2$. T dwarfs that are either binary benchmarks or red outliers have been labeled. As can be seen, ULAS J1416+1348B and BD+01^o 2920B show very red $H-W2$, although BD+01^o 2920B may be less of an outlier relative to its spectral type. Both of these objects are metal-poor. However, at earlier spectral types, the benchmarks Hip 73786B and Hip 38939B are not particularly red in comparison to their types.

mid 2013.

The results from different solutions for the two objects are shown in Table 3.4. The distances are within the errors equal while the proper motions do not appear to be. This however is misleading as if we look at the proper motions in polar coordinates the amplitudes are almost equal what is different is the direction. If we assume the orbit of the objects is on the plane of the sky and circular the separation at the mean distance is 90AU which for an 80 and 40 Jupiter mass system equates to a period of ~2500 years or a annual motion of 24mas/yr. This difference found in the proper motions is consistent with this small orbital motion between the two objects.

Table 3.4: A table showing the proper motion data for SDSS J141624.08+134826.7 and ULAS J1416+1348.

Target	SDSS J141624.08+134826.7	ULAS J141623.94+134836.3
α, δ (J2000)	14:16:24.1, +13:48:27.8	14:16:23.9, +13:48:36.8
Epoch yr	2012.0940	2012.0940
Absolute parallax mas	106.1 ± 3.5	103.3 ± 3.5
$\mu_{\alpha cos\delta}$ mas/yr	94.6885 ± 2.5	57.3 ± 2.5
μ_{δ} mas/yr	131.0 ± 3.0	153.4 ± 2.9
Relative to absolute correction mas	0.88	0.80
Duration of observations, yrs	3.97	3.97
reference stars, no. of observations	33, 99	33, 99

Table 3.5: A summary of properties of ULAS J1416+1348B.

Property	Value
R.A. (J2000.0)	14h 16m 23.94s
Declination (J2000.0)	$+13^o$ 48m 36.3s
Parallax (mas)	103±3
Distance (pc)	9.7±0.3
Spectral type	T7.5±1[a]
$\mu_{\alpha cos\delta}$ (mas yr^{-1})	57.3±2.5
μ_{δ} (mas yr^{-1})	153.4±2.9
$\mu_{\rm overall}$ (mas yr^{-1})	163.7±3.8
Radial velocity	$-39\pm1\,{\rm km\,s^{-1}}$
Bolometric flux/Wm^{-2}	$(6.2 \pm 0.6) \times 10^{-16}$
Luminosity/W	$(6.9 \pm 0.7) \times 10^{20}$
$\log_{10}$ ($L_{\rm obj}/L_{\odot}$)	−5.74±0.04
$Y_{\rm MKO}$	18.13±0.02[a]
$J_{\rm MKO}$	17.35±0.02[a]
$H_{\rm MKO}$	17.62±0.02[a]
$K_{\rm MKO}$	18.9±0.2[a]
[3.6]	14.69±0.05[a]
[4.5]	12.76±0.03[a]
$W2$	12.75±0.03[b]
$M_{\rm Y}$	18.20±0.08[c]
$M_{\rm J}$	17.42±0.08[c]
$M_{\rm H}$	17.69±0.07[c]
$M_{\rm K}$	19.0±0.2[c]
$M_{[3.6]}$	14.76±0.09[c]
$M_{[4.5]}$	12.83±0.09[c]
$M_{\rm [W2]}$	12.82±0.08[c]

[a] indicates Burningham *et al.* (2010b), [b] is the transform as shown in this work and [c] indicates absolute magnitudes calculated using the parallactic distance.

I have used this distance to derive absolute magnitudes across $YJHK$ and [3.5], [4.5] and $W2$-bands for ULAS J1416+1348B. These and the individual parallax values and motion-components are listed in Table 3.5, along with the flux and luminosity of this object (see Section 3.5.1 for a discussion of the luminosity, temperature and radius of this object).

3.5 Absolute magnitudes, luminosities and binarity

3.5.1 Physical properties of ULAS J1416+1348B

I have calculated the bolometric flux of ULAS J1416-1348B, following the method of Burningham *et al.* (2009) and Pinfield *et al.* (2012). I combine our flux-calibrated $YJHK$ spectrum with model spectra, so as to account for regions outside of our spectral coverage. Our NIR spectrum runs from 0.6-2.48μm and consequently already contains the optical region within which T dwarfs have any significant amount of flux, thus no separate optical scaling is required. In the cases of Epsilon Indi Ba and Bb, where V-band magnitudes have been measured, those magnitudes are respectively 24.12$\pm$0.03 and $\geq$26.6 (King *et al.* 2010). As all of our red objects have later spectral types, there will be even less optical flux than for either of the Epsilon Indi T dwarfs, hence confirming that there is no need to scale the optical region separately. To account for the mid-infrared flux, I use the *Spitzer* [3.6]- and [4.5]-magnitudes to scale the 2.3-3.95μm and $\lambda >$ 3.95μm regions of the model spectrum. A set of BTSettl models with $T_{\rm eff}$ 500K - 1000K, $\log g = 4.0$ to 5.5 and [m/H]= -0.5 to $+0.5$ respectively are used for this purpose. I chose a range this broad so as to avoid introducing any potentially-unfounded assumptions into our choice of model spectrum, although I do note that this assumes $T_{\rm eff} < 1000$ K for the object. I use a Monte Carlo method to account for the uncertainty introduced into the flux by the errors on the Spitzer magnitudes and the noise on the observed spectrum. Within this method, the error spectrum and the magnitude-errors are offset from themselves by a randomly-generated factor, and added to the object spectrum and the magnitudes. This process is repeated 10000 times. Our $F_{\rm bol}$ is the median of the values found by the Monte Carlo routine, and the error returned is the standard deviation of the set.

I find that the bolometric flux for ULAS J1416-1348B is $(6.2 \pm 0.6) \times 10^{-16}$ Wm^{-2}. (Table 3.5 summarises these results, amongst others.)

With a bolometric flux and a parallactic distance, it is possible to derive an intrinsic

Table 3.6: Temperatures for ULAS J1416+1348B.

Radius (R_{Jupiter})	$\mathrm{T_{eff}}$/K
0.5	935
0.6	853
0.7	790
0.8	739
0.9	697
1.0	661
1.1	630
1.2	604
1.3	580
1.4	559
1.5	540
1.6	523
1.7	507

Temperatures as computed for a variety of possible radii;
these computations use the derived luminosity of $(6.9\pm0.7)\times10^{20}$ W.

luminosity. I use the distance of 9.7±0.3pc for ULAS J1416+1348B (this value is for the T dwarf itself, not the L dwarf companion). Assuming that the two objects are indeed physically-bound, and thus the distance applies to both, and taking into account the uncertainties associated with the bolometric flux, then I find that ULAS J1416-1348B has a luminosity of $(6.9 \pm 0.7) \times 10^{20}$ W, or $\log L/L_{\odot} = -5.74 \pm 0.04$.

By comparison, the luminosity of BD+01^{o} 2920B is -5.83 ± 0.05, different despite the similarities of the two objects' spectra. The luminosity for ULAS J1416+1348B is somewhat closer to the value found for 2MASS J0939-2448 in Burgasser *et al.* (2008a): $\log(L_{obj}/L_{\odot}) = -5.69 \pm 0.03$. As ULAS J1416+1348B is brighter than BD+01^{o} 2920B, this means unresolved binarity cannot be ruled out for this object based purely on its luminosity. However, the luminosity does not argue as strongly for binarity as that of 2MASS J0939-2448.

With a luminosity, it is possible to estimate an effective temperature by assuming a range of radii. Burrows *et al.* (2001) suggest a range of radii of 0.7-1.3 R_{Jupiter} is physically-plausible for mature brown dwarfs. In addition, Burrows *et al.* (2011) suggest radii of brown dwarfs increase $\sim 1.0\%$ to $\sim 2.5\%$ for each 0.1 dex decrease in metallicity. Consequently, as ULAS J1416+1348B shows spectral evidence of low metallicity, I broadened the range of radii considered to account for this possibility. These results are shown in Table 3.6.

The relations in Stephens *et al.* (2009) suggest a $\mathrm{T_{eff}}$ of 800K for a type T7.5 object;

for this effective temperature, I find that the luminosity of ULAS J1416+1348B demands a radius of 0.6-0.7 $R_{\rm Jupiter}$, which seems unusually-small. In fact, this would be rather small even for solar metallicity, and seems even less plausible for a substellar metallicity object in light of the predictions from Burrows *et al.* (2011). This would suggest that ULAS J1416+1348B is larger than this radius and cooler than this temperature. Burningham *et al.* (2010b) found a best-fit temperature of 500K for this object; given our luminosity, this would require a radius of more than 1.7 $R_{\rm Jupiter}$, or $\sim$0.17 $R_{\rm Sun}$. The radius required, however, is sufficiently large that this would seem difficult to achieve even with unresolved binarity. It therefore seems plausible to suggest that ULAS J1416+1348B is warmer than 500 K.

Pinfield *et al.* (2012) found a $T_{\rm eff} = 680 \pm 55$K for BD+01^o 2920B; if it were assumed that there is a similar temperature for ULAS J1416+1348B, then this would imply a radius in the range of 0.8-1.1 $R_{\rm Jupiter}$, which would be consistent with current theories of brown dwarf structure.

Also, 2MASS J0939-2448 is strongly-suspected of unresolved binarity, and this object has a luminosity of $\log{(L_{\rm bol}/L_{\odot})}$ = -5.69±0.03, which is substantially-brighter than BD+01^o 2920B. Figure 3.7 compares the absolute J-band magnitudes for 2MASS J0939-2448 , ULAS J1416+1348B and BD+01^o 2920B against their $J-[4.5]$ colour. BD+01^o 2920B is fainter than 2MASS J0939-2448, while ULAS J1416+1348B is closer to the first object in luminosity (in fact their error-ranges almost overlap). This supports the argument that 2MASS J0939-2448 is an unresolved binary, whilst also suggesting that ULAS J1416+1348B could be unresolved binary as well. However, the remaining red $H-[4.5]$ outlier, BD+01^o 2920B, most likely is not an unresolved system.

Figure 3.8 plots T dwarfs with luminosities and mid-infrared photometry, from Dupuy and Liu (2012) and Golimowski *et al.* (2004); the spectral types of the Golimowski objects have been updated to those of the Burgasser *et al.* (2006a) system, so as to maintain consistency with the other objects. The $J-[4.5]$ colour is sensitive to spectral shape across the near- and mid-infrared range. On this plot, 2MASS J0939-2448 , ULAS J1416-1348B and BD+01^o 2920B are all low luminosity and very red in colour. However, ULAS J1416-1348B is appreciably-redder in $J-[4.5]$ than the other two objects. As both ULAS J1416-1348B and BD+01^o 2920B are likely of comparable metallicity, and 2MASS J0939-2448 is likely higher-metallicity, this would seem to suggest that ULAS J1416+1348B's extra redness in $J-[4.5]$ may be due to higher surface gravity than the other two objects. (For

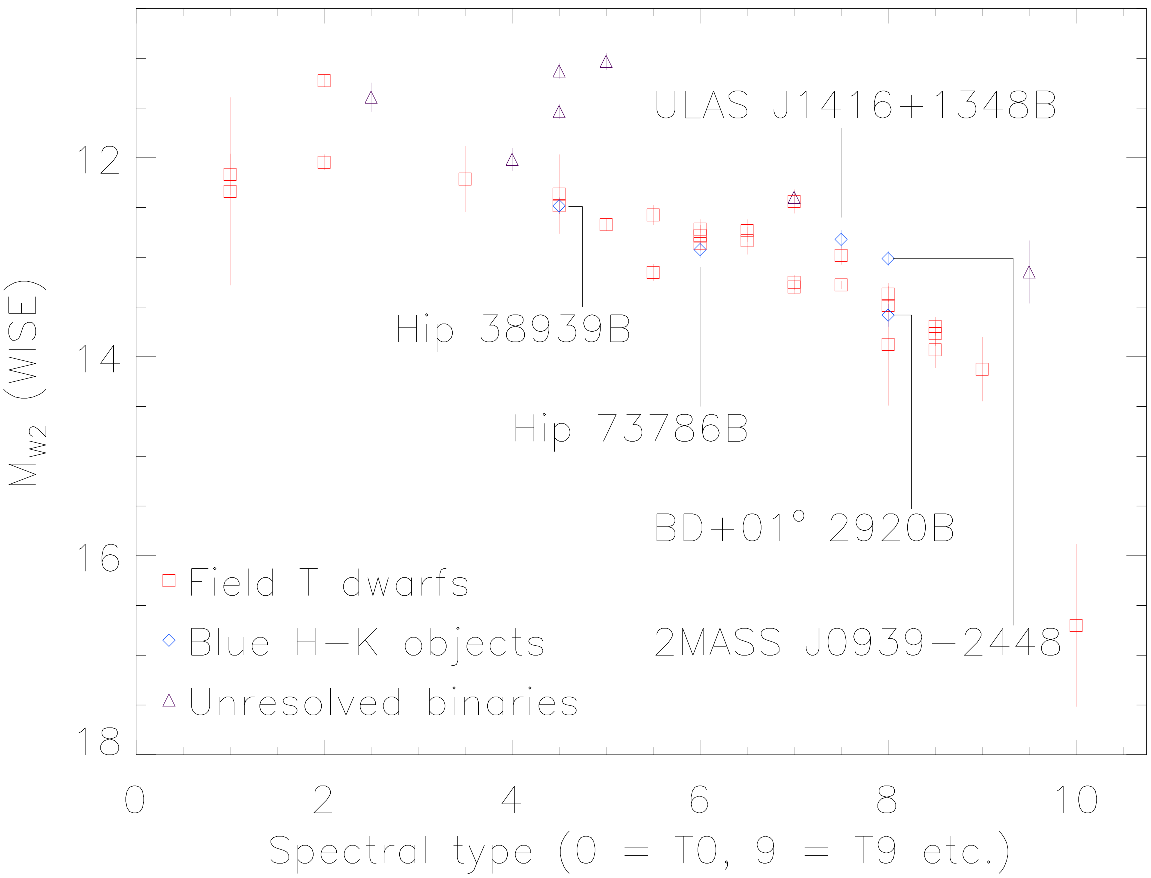

Figure 3.6: A plot showing absolute $W2$-magnitude plotted against spectral type. The background objects are T dwarfs from Dupuy and Liu (2012); in addition, various possible low-metallicity T dwarfs have been indicated with labels and blue diamond symbols. The error bars represent the error in absolute magnitude due to parallax and photometry uncertainties. ULAS J1416+1348B and 2MASS J0939-2448 appear somewhat overwrought in $W2$, whereas BD+01^o 2920B does not. This suggests that ULAS J1416+1348B and 2MASS J0939-2448 can be unresolved binaries, whereas the other object isn't.

a discussion of evidence for higher surface gravity in this object, see Section 3.5.5.)

Figure 3.9 compares a set of objects with mid-infrared colours and luminosities, from Dupuy and Liu (2012) and Golimowski *et al.* (2004). None of the three objects appear to be bright relative to their type; see Figure 3.9. In fact, all three are amongst some of the faintest objects on the plot. However, 2MASS J0939-2448 is more luminous than the other two, although it still remains faint for its type.

3.5.2 Binarity

Burgasser *et al.* (2008b) find a luminosity of $\log L_{\rm obj}/L_\odot = -5.69 \pm 0.03$ for 2MASS J0939-

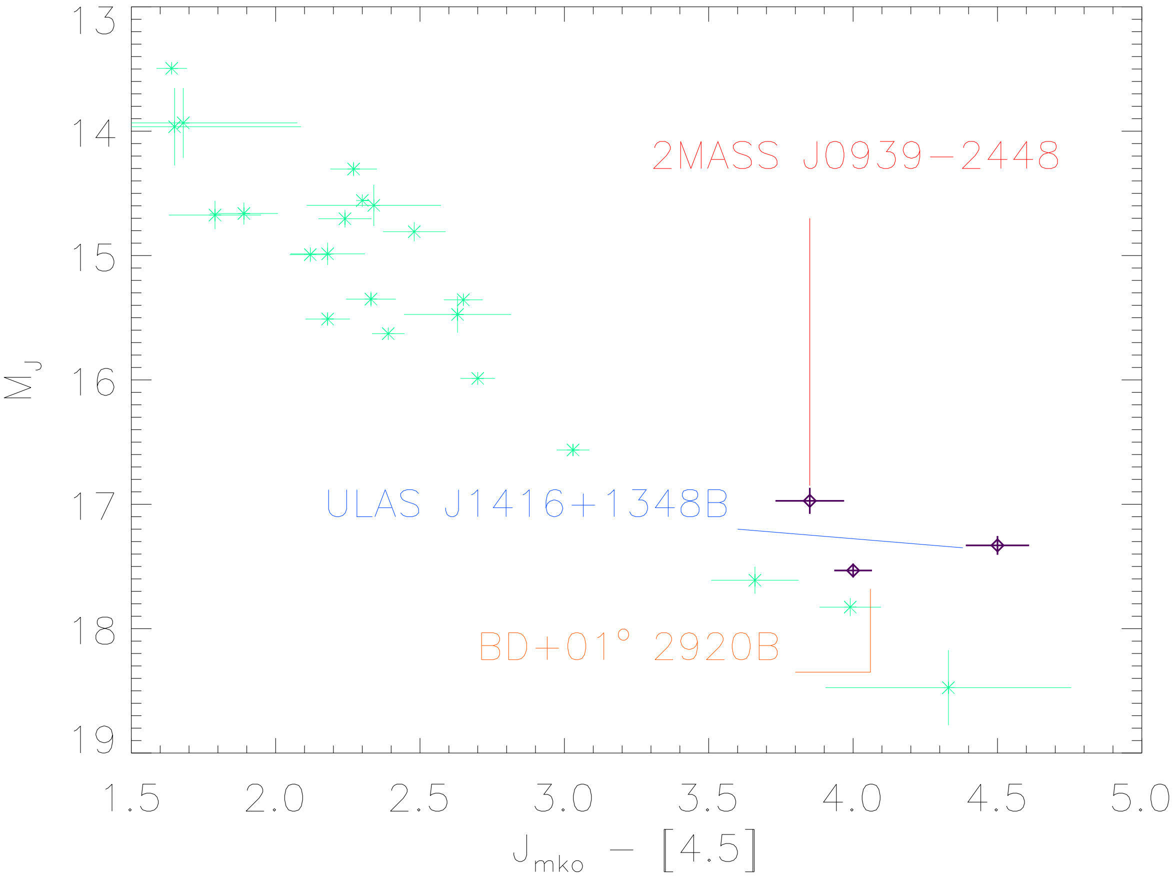

Figure 3.7: Absolute J-band magnitude is compared against $J - [4.5]$ for single T dwarfs from Dupuy and Liu (2012). 2MASS J0939-2448 has an appreciably-brighter M_J than either ULAS J1416+1348B or BD+01^o 2920B.

2448. Although faint, given the object's estimated temperature, this would require a highly-inflated radius of $\sim 0.13 R_{\mathrm{Sun}}$. As this seems implausible in light of models of brown dwarf structure and evolution, Burgasser *et al.* (2008b) suggest that 2MASS J0939-2448 may be an unresolved binary.

This interpretation is supported by 2MASS J0939-2448's position in Figure 3.6, where the object shows some evidence of over-brightness. ULAS J1416+1348B shows similar behaviour.

2MASS J0939-2448's luminosity with respect to its type, as seen in Figure 3.8, makes it brighter than BD+01^o 2920B, and the other comparison T8 object. This is consistent with a binary interpretation. A similar situation is apparent for ULAS J1416+1348B.

Figure 3.7 also shows that both ULAS J1416+1348B and BD+01^o 2920B have somewhat-

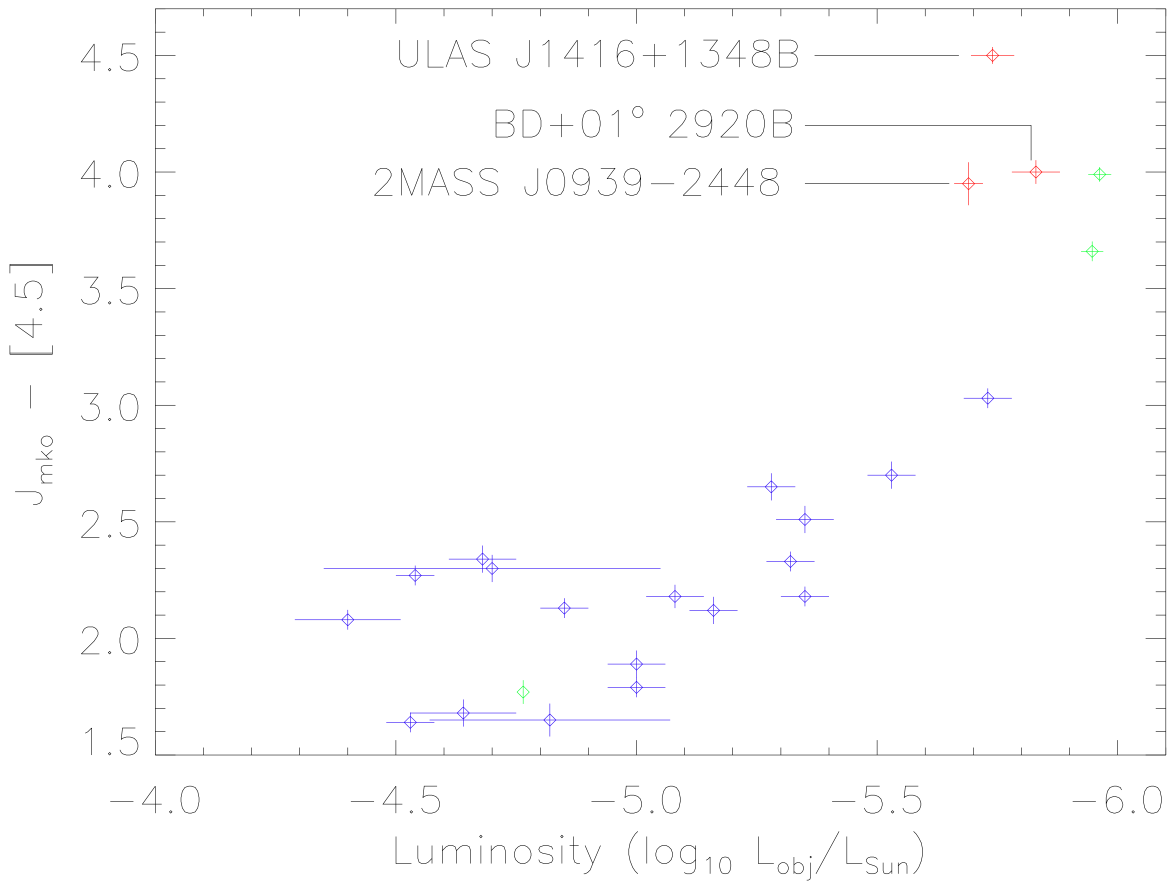

Figure 3.8: Luminosity is compared against $J - [4.5]$ for T dwarfs from Marocco *et al.* (2010) (green symbols), and Golimowski *et al.* (2004) (blue symbols) and for 2MASS J0939-2448 , ULAS J1416+1348B and BD+01^o 2920B (red; labeled). 2MASS J0939-2448 is appreciably more luminous than either ULAS J1416+1348B or BD+01^o 2920B. The spectral types of the Golimowski *et al.* (2004) objects have been updated to those of the Burgasser *et al.* (2006a) system, so as to maintain consistency with the other objects.

similar M_J magnitudes; 2MASS J0939-2448 is brighter than both of them.

3.5.3 Metallicity

The Y-band spectra of BD+01^o 2920B and ULAS J1416+1348B are similar in shape; see Figure 3.10. Given the similarities and the presence of CIA H_2 absorption in the K-bands, it seems very likely that both are low-metallicity. However, 2MASS J0939-2448 displays a steeper blueward slope, which suggests that it is a higher-metallicity object than ULAS J1416+1348B.

Figure 3.11 shows BTSettl model spectra plotted along with the filter profile for $W2$.

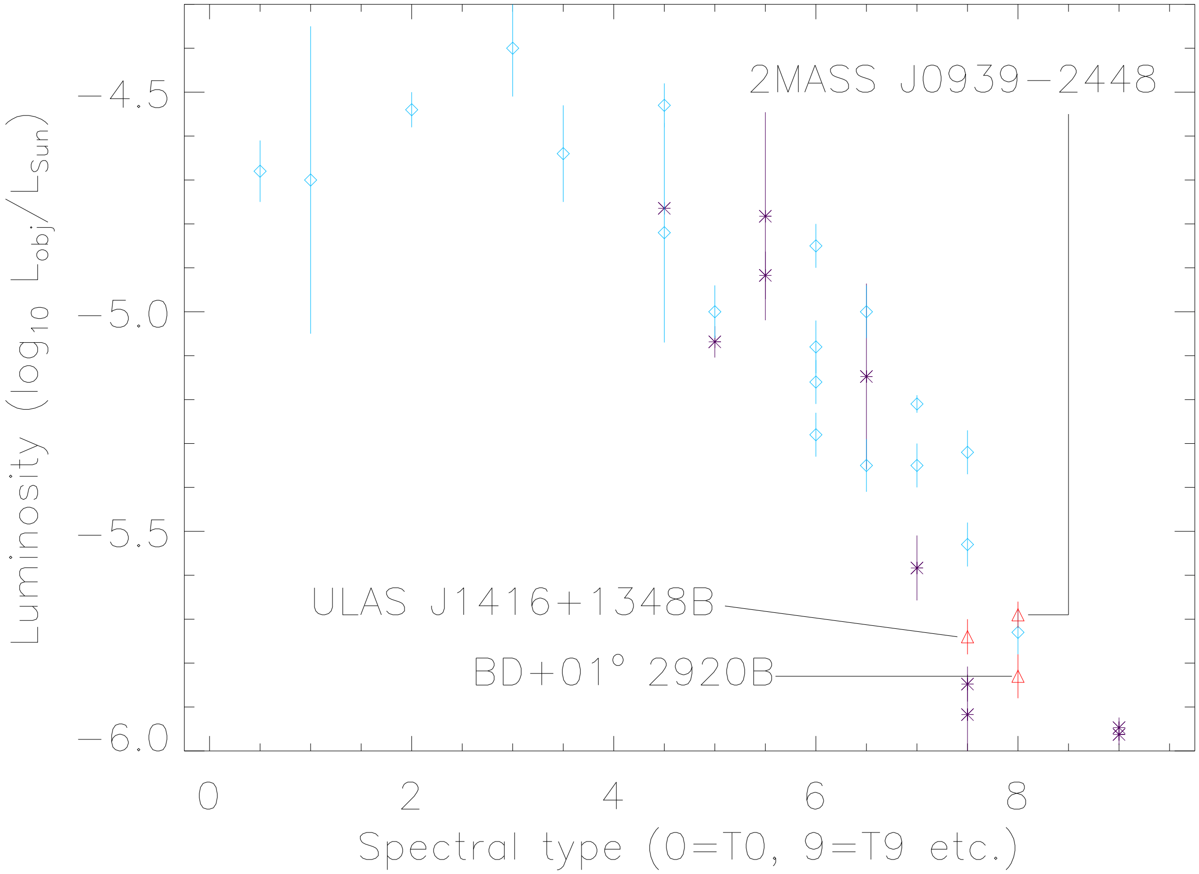

Figure 3.9: Luminosity is compared against spectral type for T dwarfs from Marocco *et al.* (2010) (purple stars), and Golimowski *et al.* (2004) (blue diamonds) and for 2MASS J0939-2448 , ULAS J1416+1348B and BD+01^o 2920B (red; labeled). Although faint relative to the whole population, 2MASS J0939-2448 is still brighter than either ULAS J1416+1348B or BD+01^o 2920B, despite being later in type than ULAS J1416+1348B. The spectral types of the Golimowski *et al.* (2004) objects have been updated to those of the Burgasser *et al.* (2006a) system, so as to maintain consistency with the other objects.

The models are both for $T_{\rm eff} = 650\,{\rm K}$ and $\log g = 5.0$, differing only in metallicity (one is for solar, the other for $[m/H]$=-0.5). The models have been normalised to the J-band peak; the filter profile is shown normalised to its point of maximum transmission. As can be seen, there is a clear theoretical prediction that metallicity can influence $W2$ flux; the subsolar-metallicity spectrum has enhanced flux around the $\sim$4.0μm peak. This means that decreasing metallicity is expected to redden mid-infrared colours.

The $W2$ filter profile (Wright *et al.* 2010) is over-plotted (the black, dotted line) and from this, it can be seen that $W2$ is most sensitive to the red tail beyond the $\sim$4.0μm peak. Consequently, $W2$-based colours will be strongly affected by absorption within this

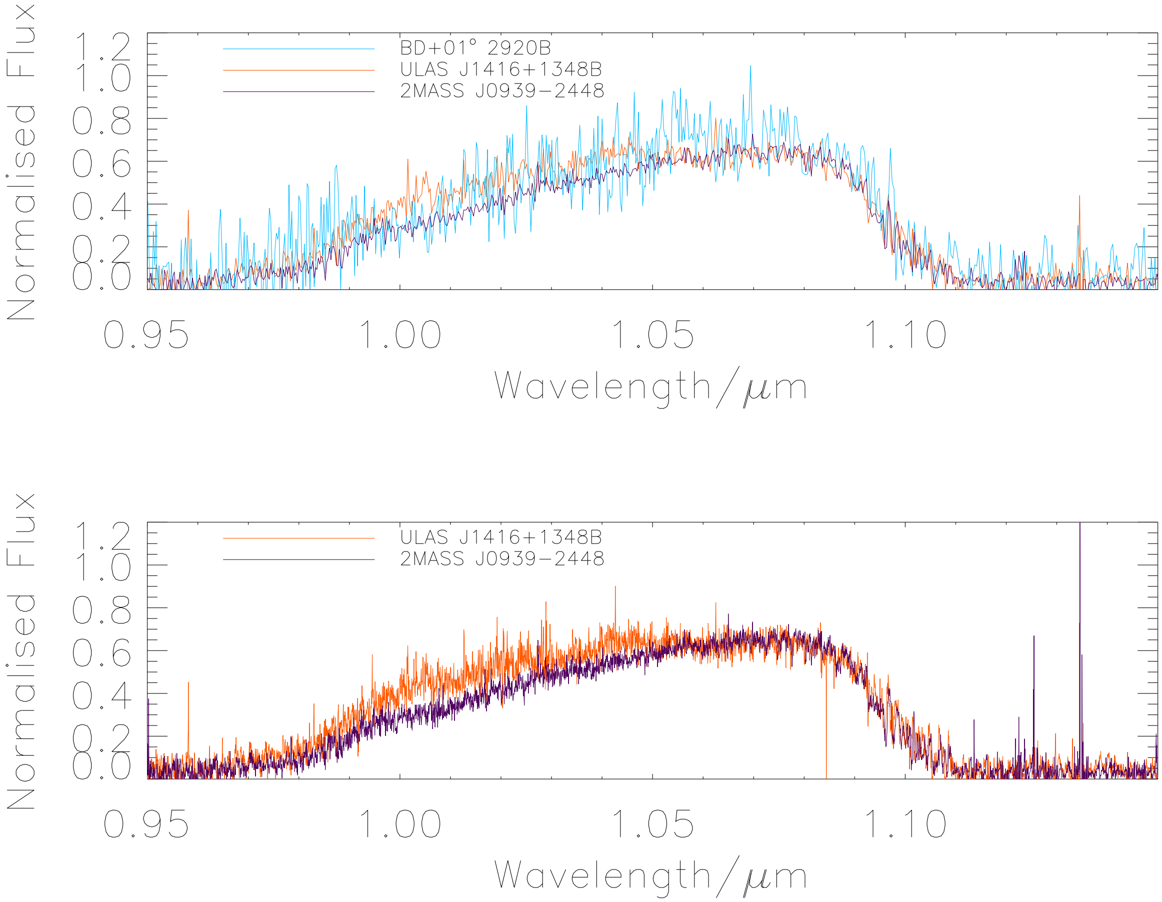

Figure 3.10: The top plot shows the Y-bands for BD+01^o 2920B, ULAS J1416+1348B and 2MASS J0939-2448 plotted against each other. The BD+01^o 2920B spectrum is that of Pinfield *et al.* (2012); the other two are the FIRE spectra that we present in this paper. The FIRE Y-bands have been put on the same wavelength scale as BD+01^o 2920B. All spectra have been normalised to their J-band peaks for ease of comparison. As can be seen, the Y-band of ULAS J1416+1348B is somewhat more similar in shape to BD+01^o 2920B than that of 2MASS J0939-2448. As the blueward Y-band slope is strongly influenced by metallicity (see Allard and Freytag 2010; Burgasser *et al.* 2006a; Burrows and Volobuyev 2003; Allard *et al.* 2003), due to the pressure-broaded red wing of the 0.77μm-potassium doublet. This absorption would be expected to be weaker in low-metallicity objects, and hence this behaviour implies that the two objects have broadly similar metallicity. The bottom plot compares the Y-band slopes of ULAS J1416+1348B and 2MASS J0939-2448; as can be seen, the band is broader for ULAS J1416+1348B, implying that it is a lower-metallicity object than 2MASS J0939-2448.

region.

In Figure 3.7, ULAS J1416+1348B and BD+01^o 2920B are both redder than 2MASS J0939-2448, and indeed most other T dwarfs. Furthermore, ULAS J1416+1348B is redder even than BD+01^o 2920B. In Figure 3.8 is the reddest object for its luminosity.

These factors suggest that there is an additional input to the colours of this object as well as unresolved binarity. Given its status as a low metallicity object, metallicity and/or surface gravity seem a likely candidate for this extra redness.

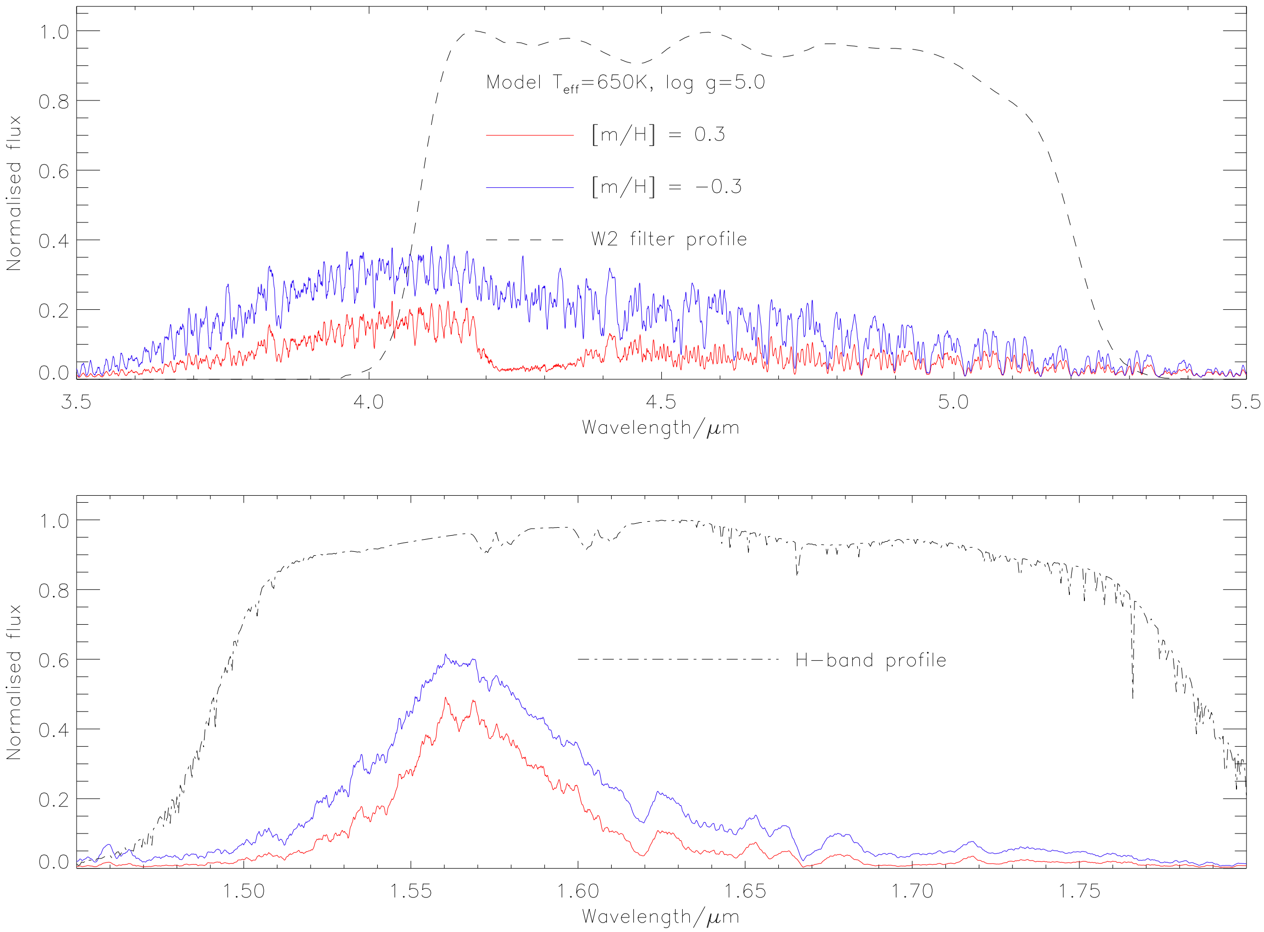

Figure 3.11: This plot shows the $W2$ filter-profile (black line) compared against BTSettl model-spectra (Allard and Freytag 2010) for [m/H]= +0.3 and for [m/H]= −0.3. Each model is for $T_{\mathrm{eff}} = 650\,\mathrm{K}$ and $\log g = 5.0$. The only difference between the models is metallicity, and as can be seen this has had a significant effect on flux.

3.5.4 Simulating unresolved binarity

In this section, I consider whether or not an object can be made into a red outlier by adding an unresolved binary companion. This will allow us to assess whether or not the colours of objects such as ULAS J1416+1348B can be purely due to binarity.

I examine the possible impact of unresolved binarity on mid-infrared colour by making

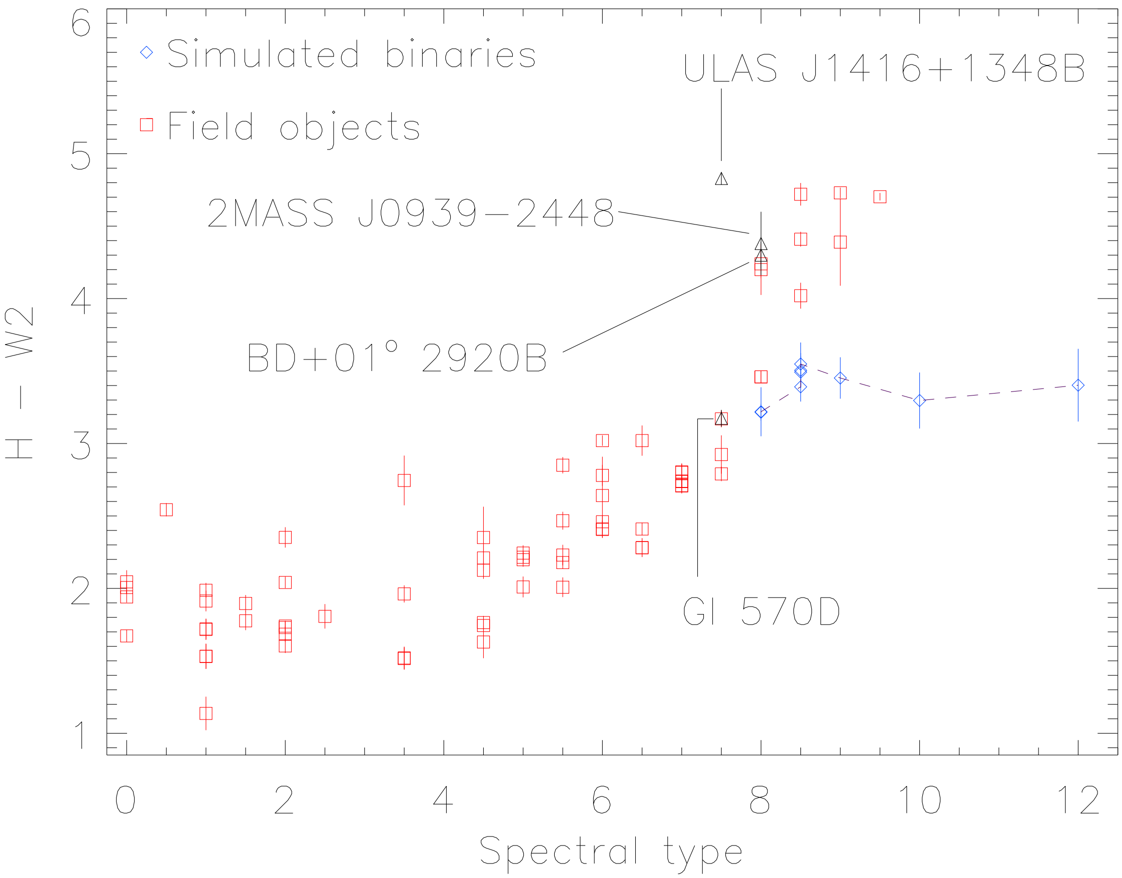

Figure 3.12: A plot showing the $H-W2$ colours for a set of background objects and a set of simulated binaries (blue asterisks). In the case of the simulated binaries, the spectral type shown here is that of the cooler companion. The combined spectrum - cooler companion plus Gliese 570D - is expected to be earlier than the types plotted here. As the spectral typing is done in the near-infrared, it is dominated by the T7 component and thus the combined binaries' types will vary little from that value.

a set of fake binaries, so as to see whether or not it is possible to create a very red colour without any input from surface gravity or metallicity. For the simulated binaries, I used the T dwarf Gl 570D (Geballe *et al.* 2001) as the primary object; this T7.5 dwarf is considered to have solar metallicity and its near- and mid-infrared colours are normal for its type. Consequently, it shows no sign of any inherent abnormality and as such makes for a good benchmark for comparative purposes.

For convenience, I assume the simulated binary system to be located a distance of 10 parsecs, hence allowing us to work with absolute magnitudes.

Using Gl 570D's parallax of 171.4±0.9 mas (Dupuy and Liu 2012), I find absolute mag-

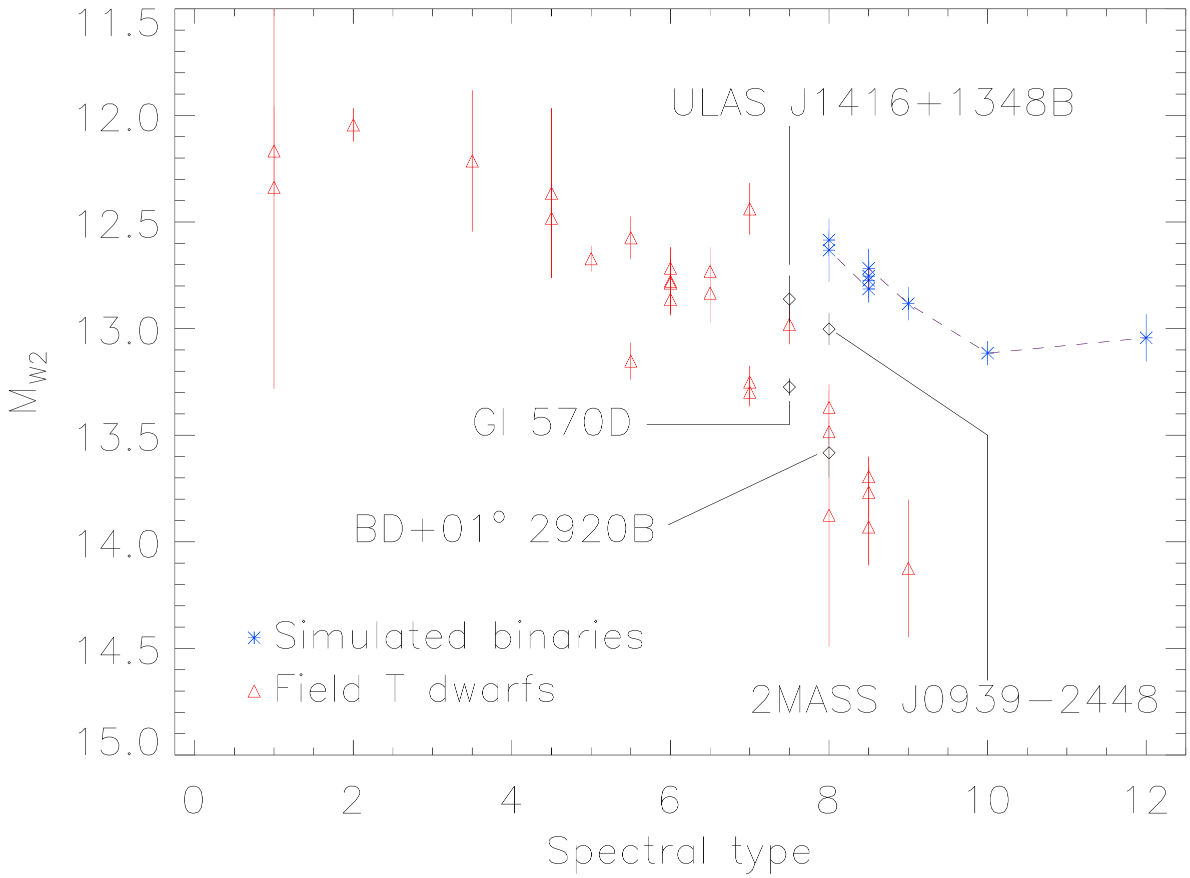

Figure 3.13: A plot showing the overall M_{W2} magnitudes of the simulated binaries (blue asterisks). In the case of the simulated objects, the shown spectral type refers to the spectral type of the cooler companion. Gliese 570D itself has also been marked, as have the three red $H-W2$ objects. BD+01^{o} 2920B clearly lies some way below the unresolved binary track, whereas 2MASS J0939-2448 and ULAS J1416+1348B lie much closer to the binary track.

nitudes such that M_J=15.9875±0.1256, M_H=16.4475±0.1138 and M_{W2}=13.2775±0.1153. (Our errors account for both inherent error on J, H and $W2$ photometry and also error in the parallax; the errors were estimated through a MonteCarlo process with 10000 iterations, using the standard deviation of the set of resultant magnitudes as the error and the median value as the absolute magnitude. I quote the numbers here to a high number of significant figures so as to avoid introducing rounding-errors into the subsequent computations.)

Using the same method, I also compute absolute magnitudes for T- and Y-dwarfs from Kirkpatrick *et al.* (2012); see Table 3.7. I base the simulated companions on a set of real objects rather than theoretical models, so as to ensure that the resulting data is as model-independent as possible.

I then convert the magnitudes for both objects into physical fluxes, using a Vega spectrum (Mountain *et al.* 1985), with a blackbody tail added for the wavelengths beyond 5.0μm. (The blackbody tail was calculated for Vega's effective temperature and was scaled to match the end of the observed flux distribution.) With both Gl 570D and the companion now having physical fluxes, it is possible to simply add the two together to simulate an unresolved binary. From these fluxes I then recover observed absolute magnitudes for the simulated binary; these magnitudes are shown in Table 3.7.

With these absolute magnitudes, a plot was made showing the $W2$ magnitude against spectral type; this is shown in Figure 3.13; the blue asterisks represent the simulated binaries, and for them the spectral type is that of the cooler companion. As can be seen, the binaries appear brighter than the field T dwarfs, although for later spectral types, they are not very much brighter than the T7-8 region. This would seem to suggest that progressively cooler, fainter companions will be overshadowed by a warmer, brighter primary.

In addition, I present a set of synthetic $H-W2$ and $J-W2$ colours for these objects. The data is shown in Table 3.8 and the $H-W2$ colour is plotted against spectral type in Figure 3.12. I find that the synthetic binaries' colours do not redden significantly with increasingly spectral type; it appears that the intrinsic faintness of a Y-dwarf companion is enough that its contribution will be overwhelmed even in the mid-infrared. Consequently, this strongly suggests that the colours of ULAS J1416+1348B can not be solely down to unresolved binarity, and that there must be an input from composition and/or surface gravity.

3.5.5 Summary and the Role of Surface Gravity

2MASS J0939-2448 appears to be an unresolved binary; it is brighter in M_J than the other two red outliers and is also brighter than other T8 dwarfs in M_{W2}. However, its somewhat-bluer mid-infrared colours and its narrower Y-band (as compared to BD+01^o 2920B and ULAS J1416+1348B) suggest that it is higher-metallicity than the other two red outliers. Furthermore, of the three objects, it is the most luminous; this is also consistent with it being an unresolved binary.

BD+01^o 2920B shows no sign of overbrightness in M_J and M_{W2}, which argues against

Table 3.7: Absolute mid-infrared magnitudes for late-type objects.

Object	Type	M_J	M_H	M_{W2}	$J-W2$	$H-W2$
Gl 570D	T7.5	16.0±0.1	16.4±0.1	13.3±0.1	2.7±0.1	3.2±0.1
Ross 458C	T8.0	16.37±0.04	16.67±0.06	13.40±0.06	3.27±0.08	2.97±0.07
2MASSI J0415-0935	T8.0	16.56±0.04	16.8±0.18	13.50±0.04	3.3±0.1	3.06±0.06
ULAS J0034-0052	T8.5	17.6±0.1	18.0±0.1	14.0±0.1	4.0±0.2	3.6±0.2
Wolf 940B	T8.5	17.8±0.1	18.4±0.1	13.8±0.1	4.5±0.2	3.9±0.2
ULAS J1335+1130	T8.5	17.83±0.07	18.18±0.07	13.80±0.08	4.4±0.1	4.0±0.1
CFBDS J0059-0114	T8.5	18.08±0.06	18.3±0.07	13.70±0.07	4.6±0.1	4.4±0.09
UGPS J0722-0540	T9.0	18.5±0.3	18.9±0.3	14.2±0.3	4.7±0.5	4.3±0.5
WISEP J0410+1502	Y0.0	20.3±0.4	20.1±0.4	15.3±0.4	4.9±0.5	5.1±0.5
WISEPA J1828+2650	Y2.0	24.0±0.4	23.3±0.3	14.8±0.3	8.5±0.4	9.2±0.5

Absolute $J-$, $H-$ and $W2$-magnitudes for Gliese 570D (Geballe *et al.* 2001) and T- and Y-dwarfs from Kirkpatrick *et al.* (2012). Errors have been calculated through a Monte Carlo procedure using the errors in parallactic distances and the errors in the photometry for all objects. The objects have been ordered by decreasing M_J-magnitude.

Table 3.8: Overall mid-infrared colours for simulated binaries.

Companion	Type	M_J	M_H	M_{W2}	$J-W2$	$H-W2$
Ross 458C	T8.0	15.41±0.08	15.80±0.03	12.58±0.05	2.82±0.09	3.22±0.06
2MASSI J0415-0935	T8.0	15.49±0.08	15.85±0.08	12.6±0.1	2.9±0.2	3.2±0.2
ULAS J0034-0052	T8.5	15.78±0.09	16.20±0.08	12.81±0.06	3.0±0.1	3.4±0.1
Wolf 940B	T8.5	15.80±0.06	16.28±0.09	12.77±0.08	3.05±0.1	3.5±0.1
ULAS J1335+1130	T8.5	15.8±0.2	16.25±0.08	12.75±0.07	3.1±0.2	3.5±0.1
CFBDS J0059-0114	T8.5	15.84±0.04	16.3±0.1	12.72±0.09	3.1±0.1	3.5±0.1
UGPS J0722-0540	T9.0	15.9±0.1	16.3±0.1	12.88±0.08	3.0±0.1	3.5±0.1
WISEP J0410+1502	Y0.0	15.97±0.04	16.4±0.2	13.11±0.06	2.85±0.07	3.3±0.2
WISEPA J1828+2650	Y2.0	15.99±0.04	16.4±0.2	13.0±0.1	2.9±0.1	3.4±0.3

Overall mid-infrared colours for the simulated binary systems, assuming that the named object is paired with Gliese 570D. The spectral type column refers to the type of the putative cooler companion. As can be seen, the colours of the unresolved system are being dominated by the hotter, brighter component, hence the surprising reversal in colours at late type. This result implies that unresolved binarity cannot be the only input to the red colours of ULAS J1416+1348B. The unresolved binaries are presented in order of M_J-magnitude.

any unresolved binarity. Its companion star BD+01^o 2920A is known to be of subsolar metallicity and this is consistent with the object's red mid-infrared colours. Its redness is therefore likely down to metallicity and/or surface gravity effects (see Figure 3.11 for an example of theoretical predictions of this phenomenon). Of the three objects, this one is the least luminous, which again seems consistent with it being a single object.

ULAS J1416+1348B appears to represent something of an intermediate case between the other outliers. It is brighter in M_J and M_{W2} than BD+01^o 2920B, and more luminous, but it is not as bright as 2MASS J0939-2448. This could be consistent with unresolved binarity, however the magnitudes' error-ranges come close to overlapping, so it does not stand out as clearly as a binary candidate as 2MASS J0939-2448. The Y-band of ULAS J1416+1348B suggests that it is lower-metallicity than that of 2MASS J0939-2448, but it does not look substantially-different from that of BD+01^o 2920B, thus suggesting the two objects are of similar colour. It is likely that composition is playing a strong role in the colours of ULAS J1416+1348B. However, its mid-infrared colours are much redder than even those of BD+01^o 2920B, thus indicating that an additional factor as well as metallicity is at work. Our simulated unresolved binaries suggest that binarity cannot redden colours enough to account for this extra offset, so even if ULAS J1416+1348B is an unresolved binary, this is likely not the explanation. It would appear that a third process is at work as well in this object.

Figure 3.11 may hint at an explanation. The $W2$ filter is particularly-sensitive to the redward tail of the $\sim 4.0\mu$m flux peak, hence $W2$ magnitudes will be strongly affected by absorption in this region.

One physical difference between ULAS J1416+1348B and BD+01^o 2920B that could explain their difference in colours is surface gravity. To examine the possible role of surface gravity in mid-infrared colours, I consider the predictions made by the BTSettl model-set. Figure 3.14 shows two 650 K models, both for solar metallicity. As can be seen, the $\sim 4.0\mu$m flux peak is in the same place and roughly the same height, however a large amount of flux has been redistributed into the redward tail. As this region is also located where the $W2$ filter is most sensitive, this demonstrates that surface gravity alone may have a substantial effect on observed colours.

To further investigate the possible role of surface gravity, I consider two 650 K models as shown in Figure 3.14, one with $\log g = 5.5$ (orange line) and one with $\log g = 4.5$ (green line). This represents something of a limiting case, as the differences in surface gravity

Figure 3.14: This plot shows two model spectra, both for $T_{\rm eff} = 650\,$K and [m/H]= 0.0, but one with $\log g = 5.5$ (orange line) and one with $\log g = 4.5$ (green line). Also plotted is the $W2$ filter, which has been scaled against its point of maximum transmission. As can be seen, surface gravity has little effect on the position and height of the $\sim 4.0\mu$m flux-peak, but it does have a substantial effect on flux in the flux tail beyond 4.0μm. As this region corresponds to the area of maximum sensitivity for $W2$, this change in flux will have an appreciable effect on mid-infrared colours.

and metallicity are very large. In particular, the higher surface gravity model is probably more extreme than reality, as Saumon and Marley (2008) suggest that $\log g = 5.36$ is the highest physically-attainable value for any T dwarf. However, the trend is clear enough; a combination of low metallicity and high surface gravity (which would lead to blue colours in the near-infrared) redistributes a large amount of flux into the mid-infrared, completely changing both the height of the 4.0μm peak and also the shape of the redward tail.

So as to quantify this observation, I derive synthetic colours for these two spectra. For the high-gravity, low-metallicity model, I find $H - W2 = 4.07$, whereas for the low-gravity, high-metallicity case I find that $H - W2 = 3.29$, or a $\sim 0.8\,$mag difference. By contrast the

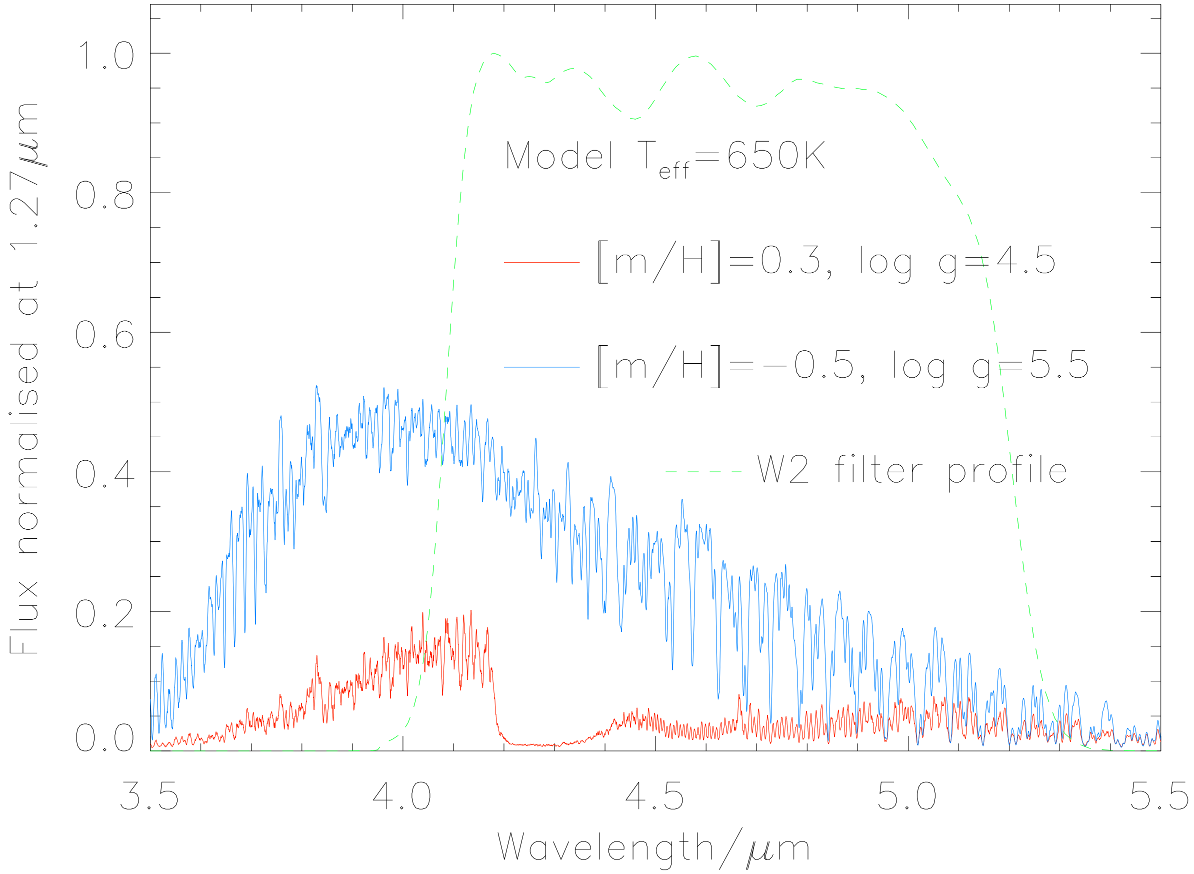

Figure 3.15: A plot showing two BTSettl models, both for 650 K, one with [m/H]= 0.3 and $\log g = 4.5$ (red line) and the other with [m/H]= −0.5 and $\log g = 5.5$ (blue line). As can be seen, in the low-metallicity, high-surface gravity case, a substantial amount of flux is redistributed to the mid-infrared. This shows that $W2$ magnitudes are not independent of metallicity and surface gravity, and even for a given effective temperature, substantial variations in colour may occur.

difference between the colours of ULAS J1416+1348B and BD+01^o 2920B is ~ 0.53 mag (see Table 3.2). Thus it is plausible that the difference in colour between them could be accounted for if ULAS J1416+1348B is a higher-gravity object than BD+01^o 2920B.

Figure 3.15 only deals with $T_{\rm eff} = 650$ K BTSettl models. To generalise this analysis further, I computed synthetic colours for the model set as a whole. The results are shown in Figure 3.16. The model predictions are clear that for any given effective temperature, a higher surface gravity and lower metallicity object will display a redder $H - W2$ than a lower surface gravity, higher metallicity object. The colour trend in the mid-infrared - redder colours with higher $\log g$ and lower metallicity - is essentially the opposite of that

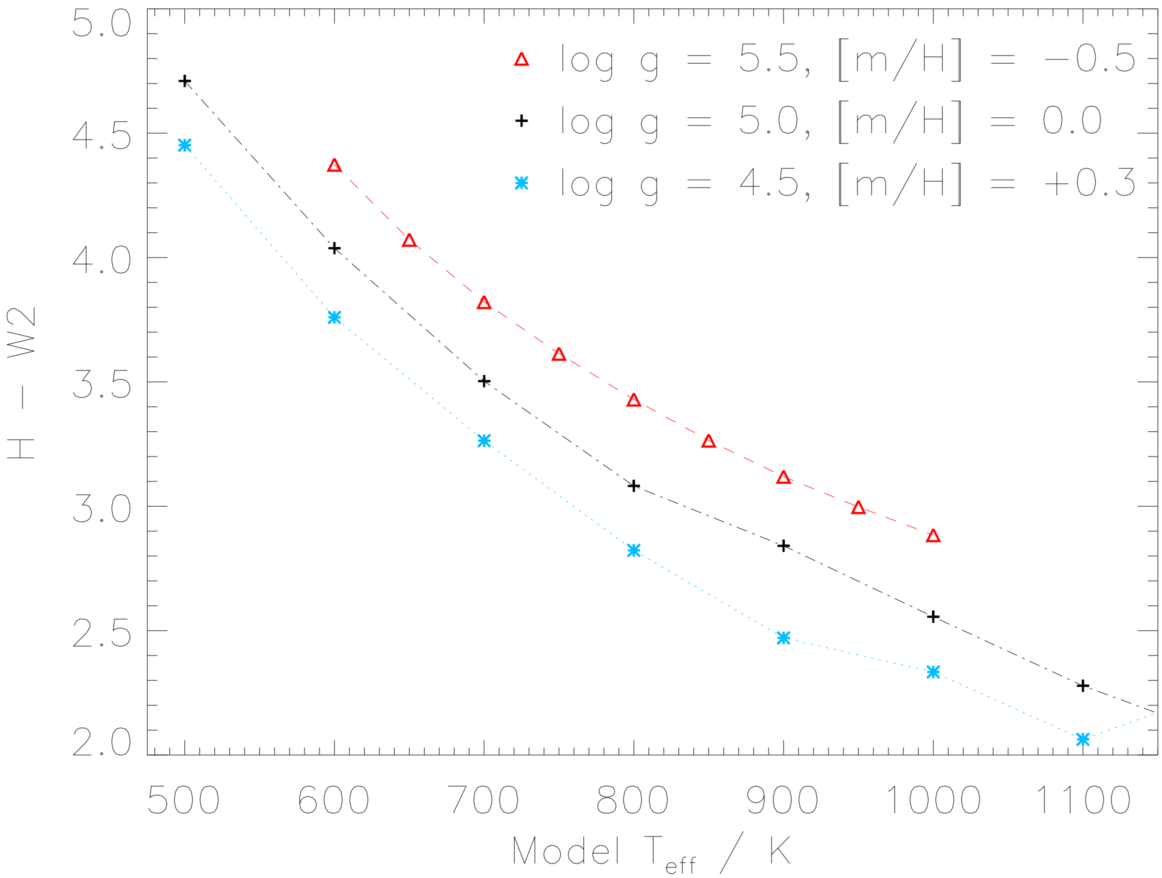

Figure 3.16: A plot showing a series of the 2011 BTSettl models and their trends in $H-W2$. Effective temperatures have been plotted up to 1100 K. Red triangles represent the case where $\log g = 5.5$ and [m/H]$= -0.5$. Black crosses represent the case whereby $\log g = 5.0$ and [m/H]$= 0.0$. Blue stars show the case in which $\log g = 4.5$ and [m/H]$= +0.3$. The red case represents the combination of characteristics which would be expected to produce the bluest near-infrared colours; it can be seen here that the predicted trend in the mid-infrared is the opposite, as the colours are much redder in $H - W2$ than for the other two tracks.

in the near-infrared, where that combination would lead to bluer colours.

Chapter 4

New Candidates and Further Follow-up of Existing Objects

4.1 Newly-Selected Candidates

Subsequent to my earlier work, T dwarf discovery efforts have continued. Consequently I have undertaken more selections. The products of these selections fall into two loose groups. The first consists of three new objects selected from the LAS by the $H-K < -0.2$ colour criterion. The second are a group of objects selected from the work of Smith *et al.* (2013). These objects were selected through their proper motions, as not all of them currently have K-band photometry.

I will describe the selections from Smith *et al.* (2013) next, then discuss the remaining three objects.

In addition, this chapter will also present some further spectroscopic follow-up for ULAS J1233+1219, ULAS J1319+1209 and ULAS J0926+0835.

4.1.1 Selections based on UKIDSS second-epoch data

The work of Smith *et al.* (2013) has recently become available. In particular, this work also includes a catalog of brown dwarfs with proper motions based on UKIDSS second epoch data. Consequently I sought to select candidate metal-poor T dwarfs from this catalog, based in this case on their proper motions. I looked for halo candidates by comparing the V, U kinematics of the Smith *et al.* (2013) objects against Equation 2.1.

Smith *et al.* (2013) select T dwarf candidates using a variation on the technique used in Burningham *et al.* (2010a). This method involves a set of photometric criteria such that an object must meet the conditions that $J - H < 0.1$, $J - K < 0.1$ and either $z - J > 2.5$ or that the UKIDSS object have no SDSS counterpart within 2 arcseconds of its position. Proper motions were then derived for objects that met these photometric criteria. (Table 4.1 provides a summary of the photometry of all of the newly-selected objects.)

With this data, I present Figure 4.1, a V, U plot for objects from the UKIDSS LAS with proper motions. $V_{\mathrm{rad}} = 0\,\mathrm{km\,s^{-1}}$ is assumed for these objects, and distances have been estimated using the spectrophotometric relationships from Marocco *et al.* (2010). To account for the non-zero but unknown radial velocities of these objects, I compute the V, U components as they would be for $V_{\mathrm{rad}} = \pm 100\,\mathrm{km\,s^{-1}}$; these are the red dashed lines in Figure 4.1. The selected objects are shown on the plot as red diamonds; the error-bars represent the V, U errors. These errors have been computed through a Monte Carlo procedure, taking into account the error in the distance estimates and the measured errors on the proper motions. (The Monte Carlo uses 10000 iterations per object, with offsets created by multiplying the object error with a random number as outputted by the IDL routine RANDOMN, a function which yields one or more Gaussian-distributed numbers with a mean of zero and a standard deviation of one.)

The range of $\pm 100\,\mathrm{km\,s^{-1}}$ was chosen as Chiba and Beers (2000) note that the 2σ velocity dispersion in W for thin and thick disc stars together is $94\,\mathrm{km\,s^{-1}}$. Consequently, a W greater than $94\,\mathrm{km\,s^{-1}}$ excludes all but $\sim 5\%$ of all disc stars. I rounded this value to $100\,\mathrm{km\,s^{-1}}$ for convenience.

Table 4.1: Photometry for the new candidates.

Object	Type	Y	J	H	K	$Y-J$	$J-H$	$H-K$	$J-K$
2MASS J003451.98+052306.8	T6.5	16.213±0.007	15.140±0.004	15.58±0.01	16.07±0.03	1.073±0.008	−0.44±0.01	−0.50±0.05	−0.93±0.03
ULAS J025409.58+022358.7	T8.0	17.0±0.01	15.916±0.009	16.29±0.02	16.73±0.05	1.08±0.01	−0.38±0.02	−0.44±0.06	−0.82±0.05
ULAS J032553.13+042540.1	T6.0	17.17±0.01	16.00±0.01	16.26±0.01	16.52±0.04	1.70±0.01	−0.26±0.01	−0.26±0.04	−0.52±0.04
ULAS J032920.22+043024.5	T5.0	18.67±0.05	17.50±0.03	17.88±0.07	18.17±0.19	1.17±0.06	−0.38±0.08	−0.3±0.2	−0.7±0.2
ULAS J092906.75+040957.7	T7.0	17.89±0.01	16.87±0.01	17.24±0.01	17.61±0.02	1.02±0.01	−0.37±0.01	−0.37±0.02	−0.73±0.02
ULAS J095047.28+011734.3	T8.0	18.9±0.03	18.02±0.03	18.4±0.03	18.85±0.07	0.88±0.04	−0.38±0.04	−0.45±0.08	−0.83±0.08
ULAS J105134.32-015449.8	T6.0	18.85± 0.03	17.75±0.02	18.07±0.02	18.27±0.04	1.10±0.04	−0.32±0.03	−0.20±0.04	−0.52±0.04
ULAS J115718.02-013923.9	T5.0	19.34±0.06	18.18±0.02	18.65±0.03	18.93±0.1	1.16±0.06	−0.47±0.04	−0.3±0.1	−0.75±0.1
ULAS J134940.81+091833.3	T7.0	20.51±0.03	19.16±0.03	19.06±0.03	19.37±0.04	1.35±0.04	0.10±0.04	−0.31±0.05	−0.21±0.05
ULAS J144901.91+114711.4	T5.5	18.35±0.04	17.36±0.02	17.73±0.07	18.1±0.1	0.99±0.04	−0.37±0.07	−0.4±0.1	−0.8±0.1
ULAS J154427.34+081926.6	T3.5	19.8±0.05	18.53±0.03	18.49±0.03	18.73±0.03	1.27±0.06	0.04±0.04	−0.24±0.04	−0.20±0.04
ULAS J234228.97+085620.1	T6.5	17.41±0.02	16.37±0.01	16.73±0.03	16.98±0.06	1.04±0.04	−0.36±0.03	−0.25±0.07	−0.61±0.06
ULAS J115338.74-014724.1	T6.0	19.1±0.03	17.59±0.02	17.97±0.02	17.82±0.02	1.51±0.04	−0.38±0.03	0.15±0.03	−0.23±0.03
ULAS J120621.08+101802.9	T6.0	20.6±0.3	19.1±0.2	19.53±0.09	-	1.5±0.4	−0.43±0.09	-	-
ULAS 130303.54+001627.70	T5.5	20.2±0.2	19.02±0.03	19.49±0.09	20.1±0.2	1.2±0.2	−0.47±0.09	−0.6±0.2	−1.1±0.2
ULAS J223728.91+064220.1	T6.5	19.79±0.08	18.78±0.05	19.23±0.04	19.94±0.18	1.01±0.09	−0.45±0.06	−0.7±0.2	−1.2±0.2

Summary of types, magnitudes and near-infrared colours for the new metal-poor/halo candidates. All magnitudes are on the MKO system.
The top section of this table shows all the objects that pass the $H-K<-0.2$ test.
The bottom section shows objects that have passed the kinematic selection, but which may not have full $YJHK$ coverage,
or those which do not pass the $H-K$ test, but are notable for their kinematics.

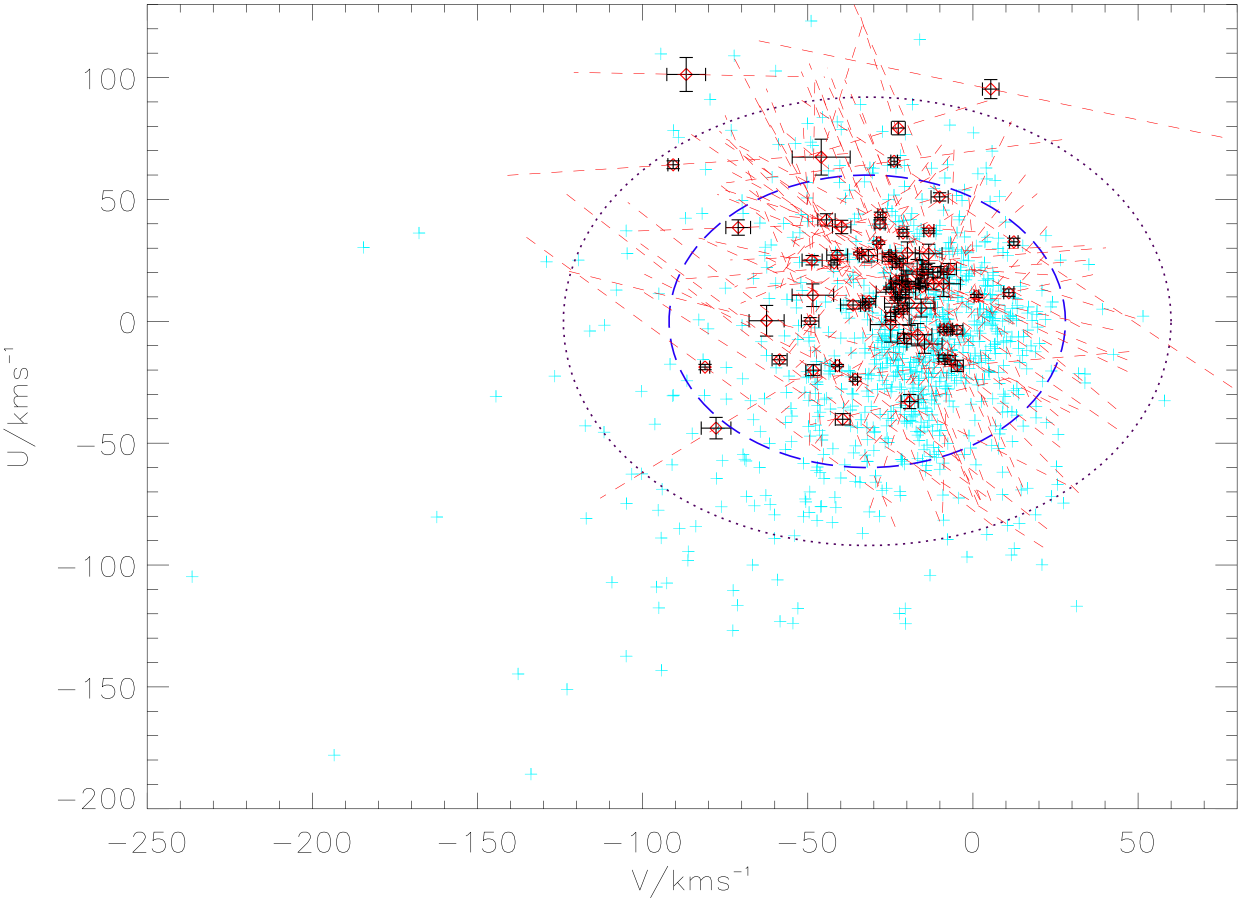

Figure 4.1: This plot shows the V and U-components for UKIDSS objects from Smith *et al.* (2013). These are the points with error bars in black; the red dashed lines show the ±100 km s^{-1} radial velocity lines for each object. The blue crosses show objects from Soubiran *et al.* (2008), plotted here as a source of comparison. The blue dashed and purple dotted ellipses respectively show the 1- and 2σ disc velocity ellipsoids.

In Table 4.3 and Table 4.2, I provide summaries of the kinematics of all metal-poor and halo-candidate objects as selected to date. Figure 4.1 reveals two new halo T dwarf candidates, ULAS J1206+1018 and ULAS J2237+0642. It also shows two objects that are outliers with respect to the 1σ disc velocity ellipsoid; these are ULAS J1153-0147 and ULAS J1303+0016.

4.1.2 The First Three New Objects

Prior to the work of Smith *et al.* (2013), I repeated the $H-K$ selection from Murray *et al.* (2011). In the time following the publication of the paper, the CDSWG T dwarf

Table 4.2: Kinematics for the halo candidates derived from Smith *et al.* (2013).

Object	$V_{\mathrm{tan}}/\mathrm{km\,s^{-1}}$	$U/\mathrm{km\,s^{-1}}$	$V/\mathrm{km\,s^{-1}}$
ULAS J1206+1018	122±9	101±7	−87±6
ULAS J2237+0642	88±4	95±4	5±3
ULAS J1153-0147	107±2	64±2	−91±2
ULAS J1303+0016	95±5	−44±5	−78±4

This table shows the V and U components for several possible new halo candidates selected from Smith *et al.* (2013). The top two objects are 2σ-candidates on Figure 4.1 and the bottom two are 1σ outliers.

Table 4.3: Kinematics for the pre-Smith *et al.* (2013) candidates.

Object	$V_{\mathrm{tan}}/\mathrm{km\,s^{-1}}$	$U/\mathrm{km\,s^{-1}}$	$V/\mathrm{km\,s^{-1}}$
ULAS J0325+0425	18.6±4.8	18.2±2.9	0.1±4.3
ULAS J0329+0430	104.4±15.8	−32.5±8.6	71.4±14.5
ULAS J0842+0936	42.5±55.4	38±3	−1.0±44.0
ULAS J0926+0835	212.5±101.3	62±40	−140±46
ULAS J0958-0039	16.3±22.3	3±27	−3±27
ULAS J1012+1021	87.89±32.02	−1±11	−87±17
ULAS J1018+0725	39.4±20.6	−16±10	5±9
ULAS J1233+1219	62.1±72.2	−11±45	45±45
ULAS J1303+0016	70.2±74.4	−20±44	−68±45
ULAS J1319+1029	191.7±66.9	183±37	−92±29
ULAS J1320+1029	13.2±24.6	0±51	−21±52
ULAS J1501+0822	50.7±65.2	12±52	−61±63
Hip 73786B	86.7±24.6	−48±7	−75±4
ULAS J2320+1448	47.51±14.08	55±10	−20±3
ULAS J2342+0856	15.73±5.04	12.6±2.3	−23.9±3.9

Summary of kinematics for all previously-selected blue objects from UKIDSS, and three objects that were selected prior to the work of Smith *et al.* (2013). (These three are ULAS J0325+0425, ULAS J0329+0430 and ULAS J2342+0856.)

sample had grown, and it was thus possible that more new candidates could be found. Repeating the $H - K < -0.2$ selection did indeed identify three new candidate metal-poor T dwarfs. These objects are ULAS J032553.13+042540.1, ULAS J032920.22+043024.5 and ULAS J234228.97+085620.1. These objects were selected solely through their near-infrared colours; proper motions for them were derived later.

I will now summarise their properties in turn.

The first of the newly-selected objects is ULAS J0325+0425. A literature search revealed that this object had already been observed in the SDSS, and was published in Chiu *et al.* (2006). As this object has a published spectrum, it was possible to plot it against spectral standards to investigate its properties. The results are shown in Figure 4.2.

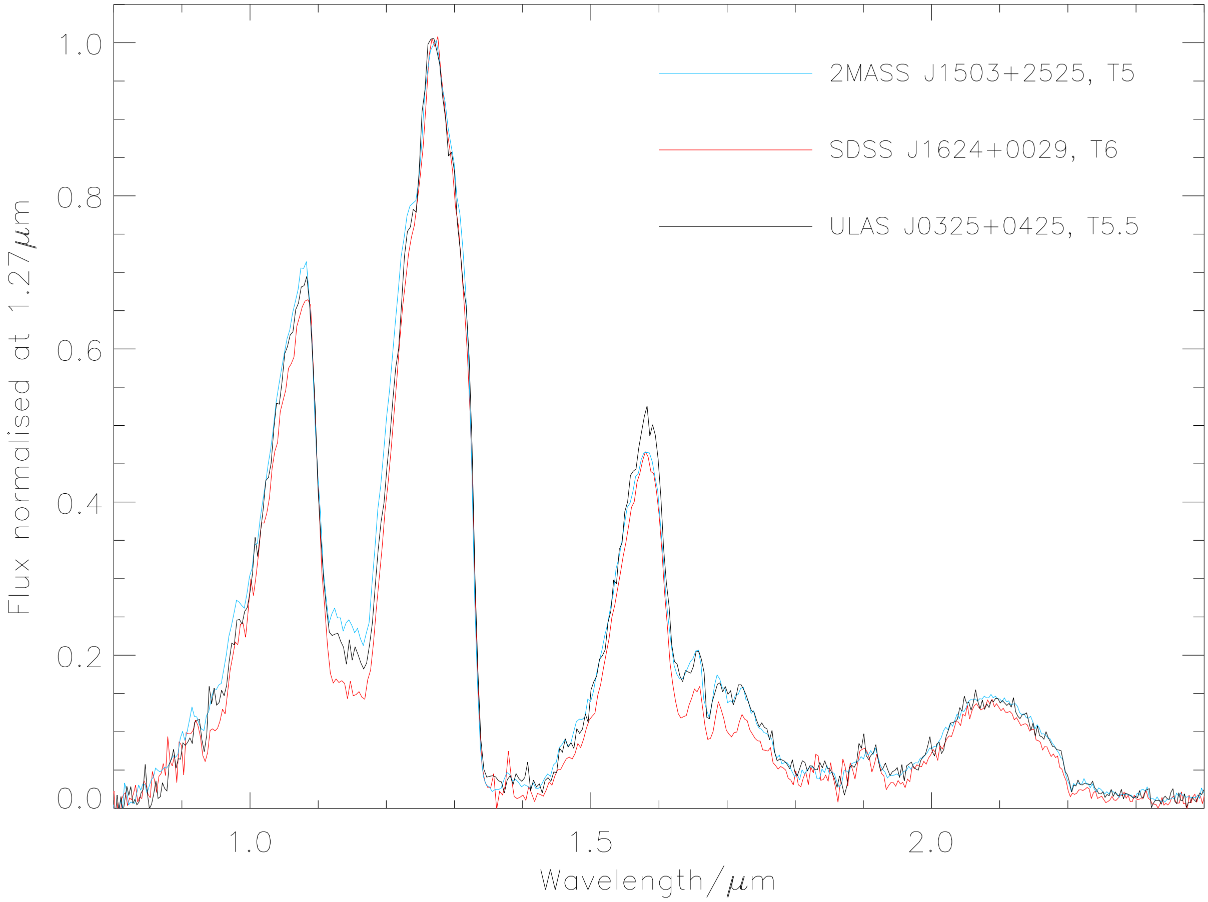

Figure 4.2: ULASJ032553.13+042540.1 was originally identified in the SDSS by Chiu *et al.* (2006), who assigned it a spectral type of T5.5. Here that spectrum is shown, plotted against the T5 and T6 spectral standards 2MASS J1503+2525 and SDSS J1624+0029 (Burgasser *et al.* 2006a). As can be seen, it does not show any evidence of significant K-band suppression or much broadening in the Y-band relative to the standards, and thus is unlikely to be significantly metal-poor.

SDSS J0325+0425 was typed by Chiu *et al.* (2006) as a T5.5; in Figure 4.2 it does not show evidence of enhanced CIA H_2 absorption in the K-band, nor does it show significant broadening in the Y-band. This object has $H - K = -0.26 \pm 0.04$. Although this is blue enough to meet the selection criteria, it is not substantially blue relative to other objects. A likely interpretation for this object is that it is not particularly metal-poor.

In addition I measured a proper motion for SDSS J0325+0425, using a UKIDSS LAS J-band image and a z-band SDSS image. The UKIDSS image was taken on 21/10/2008, the SDSS image on 14/12/2004, thus providing a ∼3.9 yr baseline. The object was found to have an FWHM of 3.74 pixels in UKIDSS and 4.0 pixels in SDSS. 26 reference stars were identified in both images, leading to a transform in GEOMAP with $\frac{1}{2}$ RMS= 0.137 in the x axis and $\frac{1}{2}$ RMS= 0.104 in the y. From the SDSS to the UKIDSS image, the object was found to have shifted by $x_{\text{shift}} = 0.2981\,\text{px}$ and $y_{\text{shift}} = 2.1137\,\text{px}$. Factoring in the pixel scale of ~ 0.39 arcseconds per pixel, this revealed a motion of ~ 0.1175" in x and ~ 0.8333 in y.

Using the epoch difference, and considering the directions of motion, the right ascension proper motion component is $29.8\,\text{mas}\,\text{yr}^{-1}$ and the declination component is $211.5\,\text{mas}\,\text{yr}^{-1}$, leading to an overall value of $213.6\,\text{mas}\,\text{yr}^{-1}$.

By considering the images' signal-to-noise ratios for the object, and the centroiding accuracy, errors of ± 43 and $\pm 42\,\text{mas}\,\text{yr}^{-1}$ are found, respectively.

Using the spectral type/absolute magnitude relations of Marocco *et al.* (2010), I estimated a distance of $18.4 \pm 3.1\,\text{pc}$ for this object. With the above values, this leads to a tangential velocity of $V_{\text{tan}} = 21 \pm 6\,\text{km}\,\text{s}^{-1}$.

This object has subsequently been selected in WISE, where it was revealed to have $H - W2 = 2.41 \pm 0.05$, which is average for its type.

The proper motions for the other two objects were calculated in exactly the same way as for ULAS J0325+0425. I summarise the relevant details of these calculations, and their results, in Table 4.4 and also in Table 4.5. Next, I will briefly discuss the colours and photometry of ULAS J0329+0430 and ULAS J2342+0856.

Table 4.4: Dates, baselines, sources and other details of the images for the three $H - K$ objects.

Object	UKIDSS *J* date	Second epoch date	Baseline (yr)	Source (2nd epoch)	x RMS	y RMS	n_{ref}
ULAS J0325+0425	21/10/2008	14/12/2004	3.90	SDSS z	0.137	0.104	26
ULAS J0329+0430	24/09/2008	12/10/2005	2.95	SDSS z	0.13	0.107	24
ULAS J2342+0856	24/09/2008	16/09/2006	2.02	SDSS z	0.115	0.098	16

This table shows the relevant details used to calculate the proper motions and errors for these objects. n_{ref} is the number of reference stars used in each image. The transformations were done into the UKIDSS *J*-band image in every case.

Table 4.5: Proper motions and tangential velocities for the three new $H-K$ selected objects.

Object	Distance (pc)	$\mu_{\alpha cos\delta}$ ($\mathrm{mas\,yr^{-1}}$)	μ_{δ} ($\mathrm{mas\,yr^{-1}}$)	V_{tan} ($\mathrm{km\,s^{-1}}$)
ULAS J0325+0425	18.4±3.1	30±43	212±42	21±6
ULAS J0329+0430	39±4	111±60	−546±61	104±16
ULAS J2342+0856	15±5	128±40	−143±42	16±5

Distances, proper motions and tangential velocities for the three objects selected through $H-K$ from UKIDSS (prior to the release of the Smith et al catalogue).

Table 4.6: Mid-infrared colours for new objects.

Object	Type	H	$W2$	$H-W2$
ULAS J025409.58+022358.70	T8.0	16.29±0.02	12.74±0.03	3.56±0.04
ULAS J032553.13+042540.10	T5.5	16.24±0.01	13.8±0.05	2.41±0.05
ULAS J092906.75+040957.70	T7.0	17.24±0.01	14.23±0.06	3.01±0.06
ULAS J095047.28+011734.30	T8.0	18.4±0.03	14.48±0.06	3.92±0.07
ULAS J123327.45+121952.20	T4.0	18.28±0.06	15.6±0.1	2.7±0.1
ULAS J144901.91+114711.40	T5.5	17.73±0.07	14.84±0.07	2.9±0.1
ULAS J154427.34+081926.60	T3.5	18.49±0.03	16.0±0.2	2.5±0.2
ULAS J223728.91+064220.10	T6.5	19.23±0.04	15.5±0.1	3.8±0.1

Summary of the $H-W2$ colours for the new objects, and also ULAS J1233+1219 and ULAS J0325+0425, which now have WISE $W2$ magnitudes.

The next object, ULAS J0329+0430, is another blue object selected from UKIDSS DR8. This object has $H-K=-0.3\pm0.2$ and an estimated spectral type of T5. A literature search found no evidence of pre-discovery. This object could not be definitively matched with anything in the WISE catalog.

ULAS J2342+0856 is one more blue object was identified from the new coverage in DR8; this is ULAS J234228.97+085620.10. This object has an estimated type of T6.5 and a $H-K=-0.25\pm0.07$. A literature search does not find any evidence of prior discovery. It was not identifiable in WISE either.

The new objects are shown in relation to our existing $H-K$ selections in Figure 4.3.

The near-infrared colours of the candidates are shown in Table 4.1 and the mid-infrared magnitudes are shown in Table 4.6 (where available). Their $H-W2$ colours are plotted against type in Figure 4.4.

In Figure 4.4, one of the new objects appears somewhat redder than typical for objects of its type. This is ULAS J2237+0642, with $H-W2=3.8\pm0.1$, as opposed to ~ 2.5 as a typical value for T6.5 objects. This object also shows rather extreme near-infrared colours in Table 4.1, with $J-K=-1.2\pm0.2$, which in fact makes it the bluest $J-K$

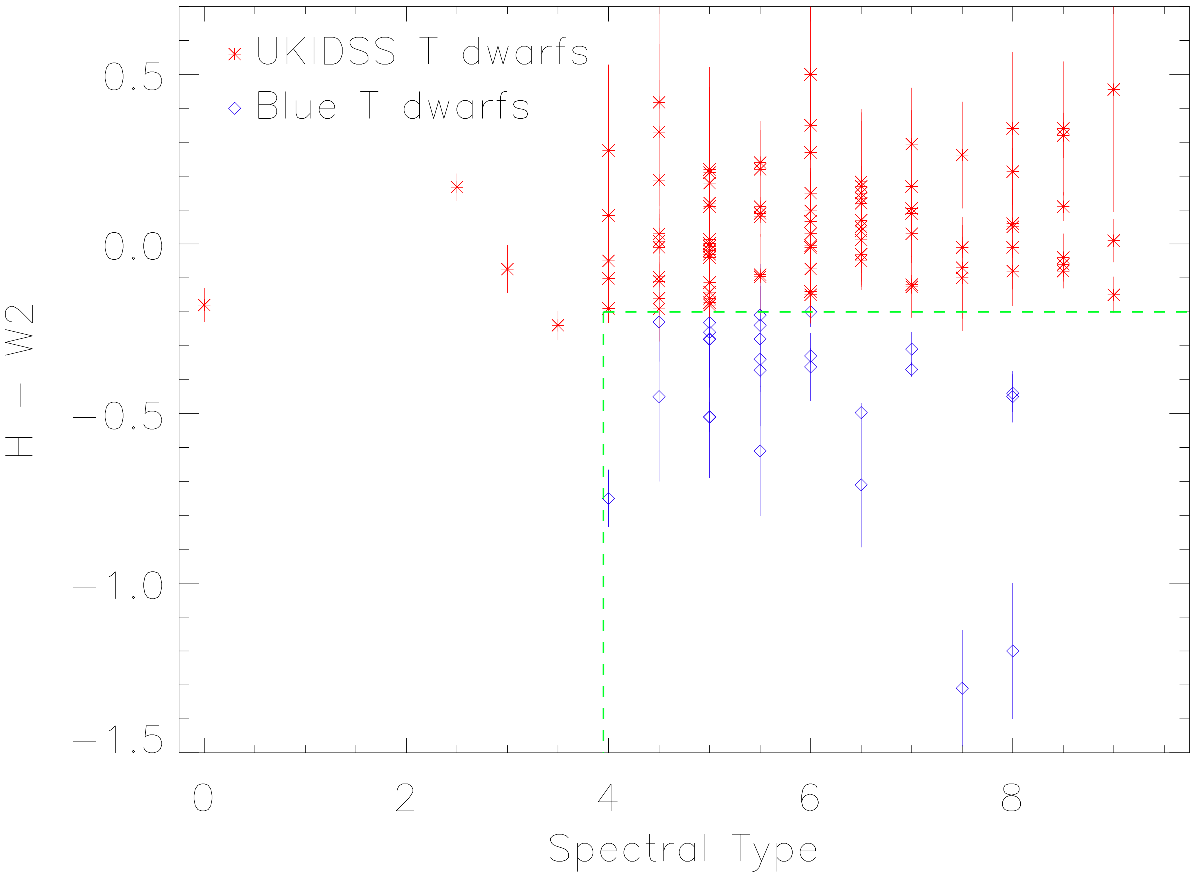

Figure 4.3: This plot shows spectral type vs $H - K$ for both the existing selections and my new objects. The edge of the selection box for spectral type has been moved to ~3.95 for clarity; as before, the selection is spectral type ≥ T4. Selected objects are shown as blue diamonds.

object in the new selection. It is noteworthy that this object was also selected as a halo candidate on Figure 4.1.

4.2 Subaru spectra

In addition to the new selections described above, recent work has also involved further follow-up of several of my previous objects.

Followup H and K band spectra were taken for ULAS J1233+1219 and ULAS J1319+1209 using IRCS on the Subaru telescope. The full JHK spectrum of ULAS J1233+1219 is presented in Figure 4.5 and that of ULAS J1319+1209 in Figure 4.6.

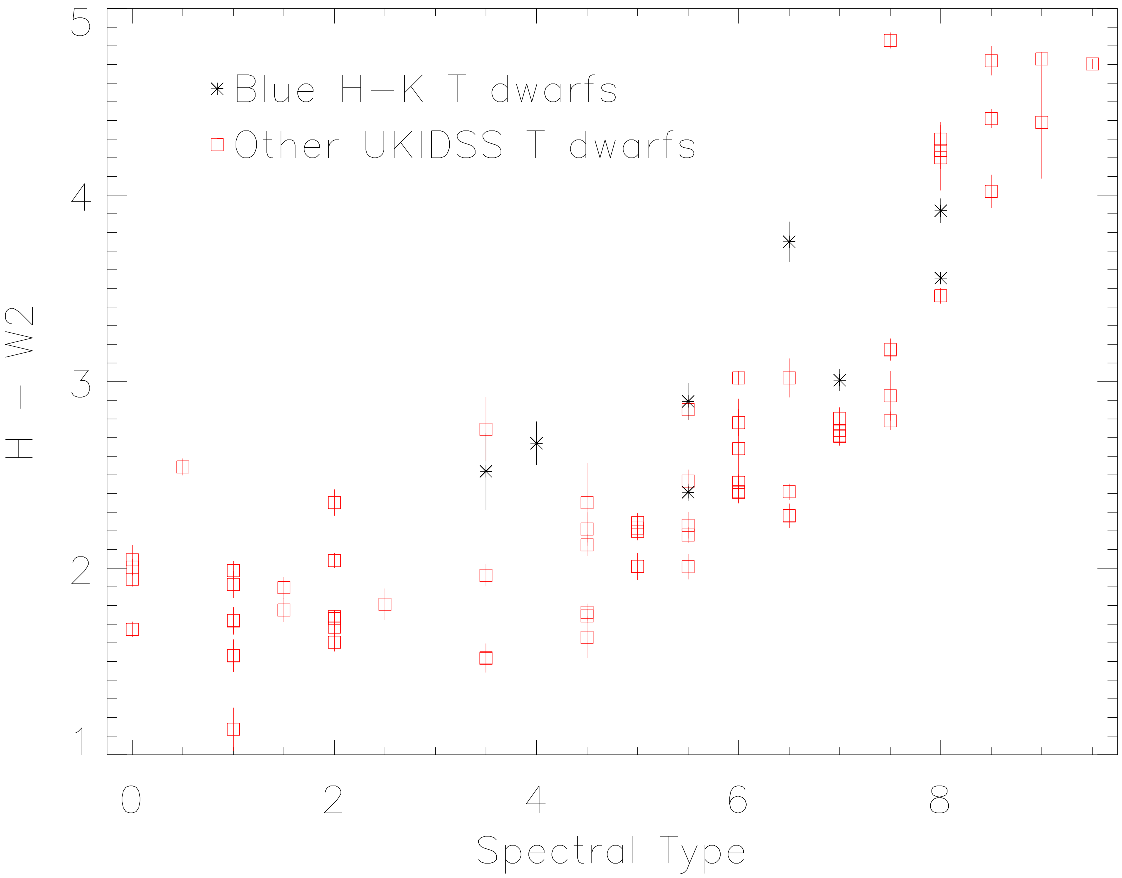

Figure 4.4: This plot shows spectral type vs $H - W2$ for the new objects. Also shown are the set of objects plotted in Figure 3.5.

4.2.1 Subaru Observations

The Infrared Camera and Spectrograph (IRCS; see Kobayashi *et al.* 2000; Tokunaga *et al.* 1998) is an instrument mounted on the 8-metre Subaru telescope at the Mauna Kea Observatory. IRCS uses two 1024x1024 ALADDIN III CCD chips. These units are sensitive between $0.9 - 5.6\mu$m. IRCS has both an imaging and a spectroscopic mode.

Many of the objects in this work lack HK spectra; consequently, IRCS's HK grism mode was used to gain spectroscopy of the bluest object in the Murray *et al.* (2011) selection and also the two halo candidates.

4.2.2 ULAS J1233+1219

ULAS J1233+1219 was observed on the night of 06/04/2010. The air mass at the start of the observations was 1.009" and the slit width used was 0.31" on the HK grism. Along with the science target, the F5v star HD 112694 was observed, to serve as a telluric standard. The science observations consisted of 16 240 second individual exposures. Flat-fields were taken at the start of the night to correct for defects within the instrument itself.

The resultant data were combined into images with IRAF. During the observations an ABBA dither pattern was used; these AB pairs were subtracted using the IRAF routine IMARITH. The resultant images were combined through median stacking using the routine IMCOMBINE.

This process was duplicated for the telluric standard.

Subsequently, sky residuals are removed from the difference-imaged pairs through an IDL routine. The object spectrum is then identified within the FITS file and this section is readout as a 2D spectrum. Wavelength calibration is done at this point, using the arc spectra taken on the night. To control for bad pixels and cosmic rays, pixels that are $\geq 3\sigma$ outliers relative to their neighbours are interpolated out.

Next, the spectrum is flux-calibrated using the standard star and its blackbody temperature. Also at this stage, telluric features are interpolated out; these are identified in the target spectrum through their presence in the standard spectrum. The tellurically-corrected object spectrum is then multiplied against the standard star's to finish the flux calibration.

Lastly, the object spectrum is read out into a plain-text form. For ULAS J1233+1219, this resulting spectrum can be seen in Figure 4.5.

Perhaps surprisingly given its near-infrared colours, this object has proven not to be a $H - W2$ outlier in Figure 4.4, having only $H - W2 = 2.7 \pm 0.1$, which makes it fairly average for a T4. It does appear to be toward the red end of the distribution, though. Given than its near-infrared colours are suggestive of low metallicity and high surface gravity, its mid-infrared colours may be an indication that composition and gravity have less of an impact on $H - W2$ at higher effective temperatures.

4.2.3 ULAS J1319+1209

ULAS J1319+1209 was also observed on IRCS. It too was observed on the HK grism mode, with 16 individual 240-second exposures. The air mass was 1.012" and the 0.31" slit was used. The standard for this object was the A0v star HD 121880.

Data reduction was performed using the procedure described for ULAS J1233+1219.

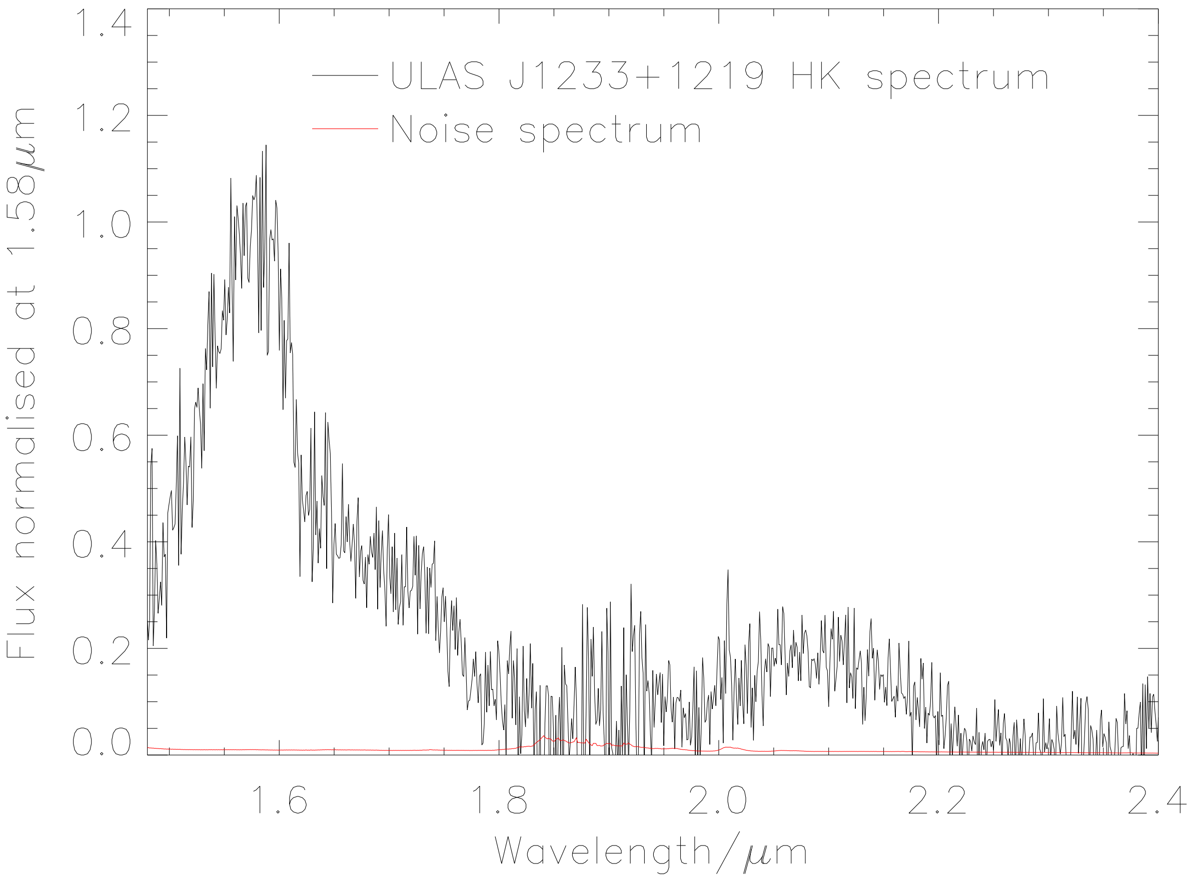

Figure 4.5: This plot shows JHK Subaru IRCS spectrum for ULAS J1233+1219. The object spectrum has been normalised to the H-band peak at 1.58μm.

The resulting spectrum can be seen in Figure 4.6.

ULAS J1233+1219's fields in WISE have been contaminated by a nearby star, and consequently the object is not resolved on its own.

4.2.4 ULAS J0926+0835

ULAS J0926+0835 was also observed, on 07/04/2010. The air mass at the start of the observations was 1.181" and the 0.31" slit was used. The standard star for this object was the A1v star 37 Cancri. Once more, sixteen 240-second individual science exposures were taken. The data reduction followed the method outlined for the previous objects.

The resulting spectrum can be seen in Figure 4.7.

ULAS J0926+0835 does not appear to be detected in WISE; there is a $W1$ source located close to the object's position, but this $W1$ source is not detected in any other

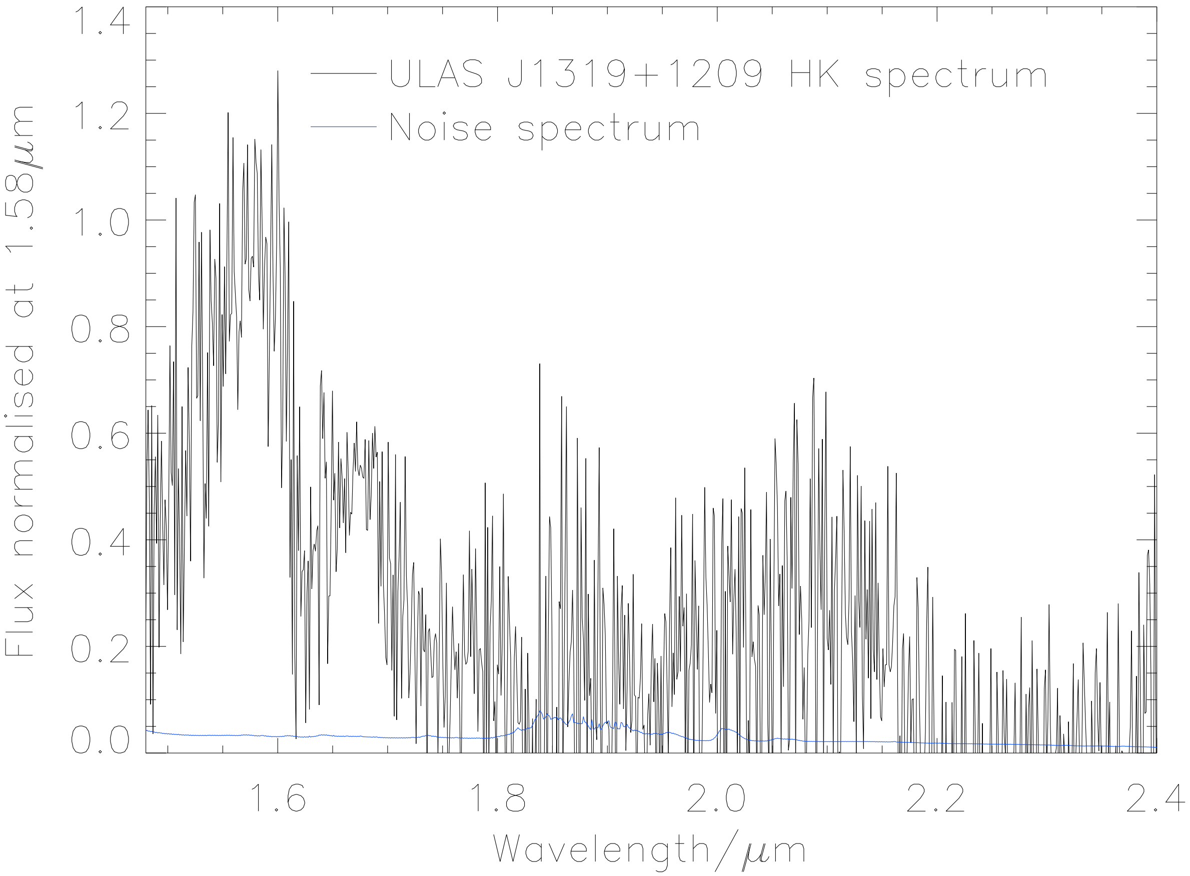

Figure 4.6: This plot shows the HK Subaru IRCS spectrum for ULAS J1319+1209. The object spectrum has been normalised the to the H-band peak at 1.58μm.

bands. T dwarfs are much fainter in $W1$ than $W2$, so the absence of a $W2$ detection makes it unlikely that this source is ULAS J0926+0835.

4.2.5 Analysis

The existing J-band discovery spectra were combined with the Subaru HK bands for these three objects; the resultant spectra are shown in Figure 4.8. The spectra were combined by weighting them by magnitude.

Using these spectra, I repeat the spectral typing undertaken in Murray *et al.* (2011). The results of this are shown in Table 4.7. Once more, we neglect the CH_4-K index, due to the great differences between these objects K-bands and those of the spectral standards. (The values for CH_4-K are still shown in the results, for completeness.) The exercise confirms the existing spectral types for ULAS J1233+1219 and ULAS J0926+0835, although

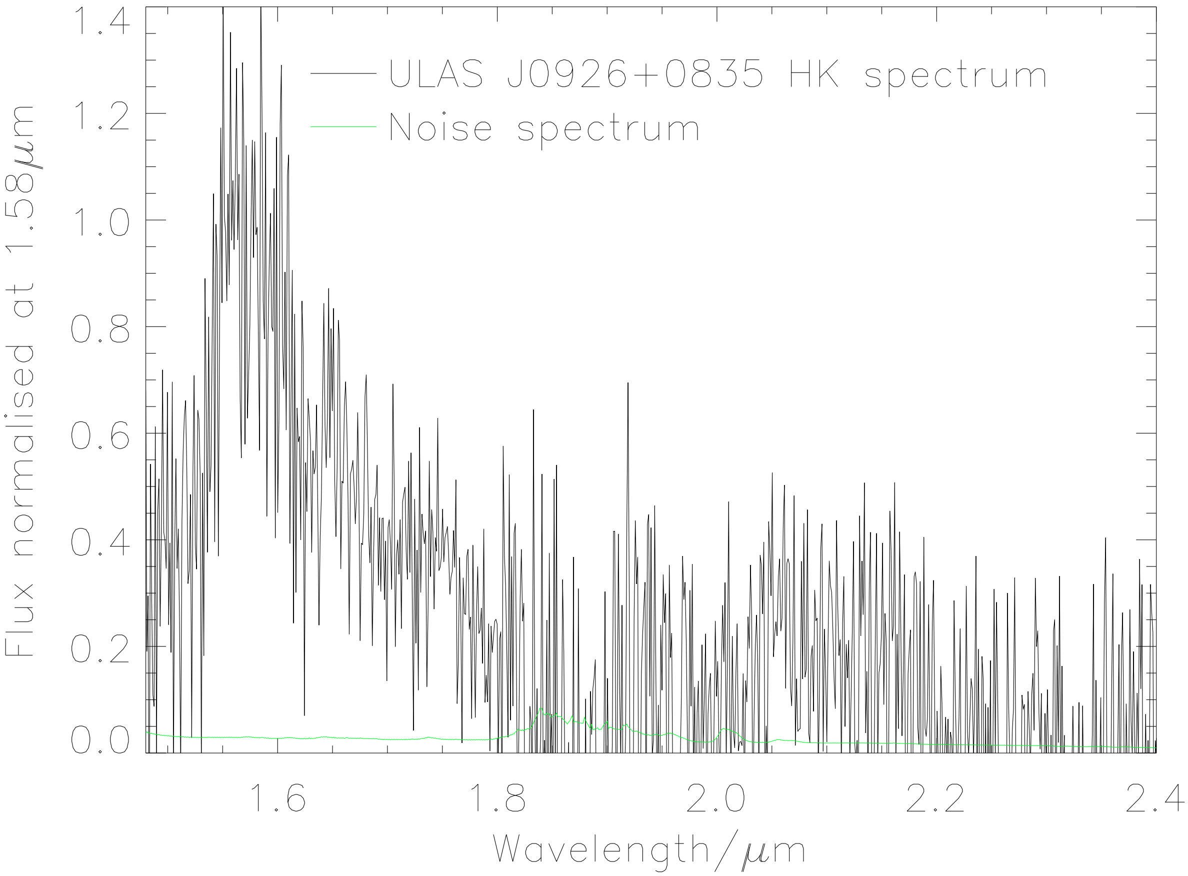

Figure 4.7: This plot shows the HK Subaru IRCS spectrum for ULAS J0926+0835. The object spectrum has been normalised the to the H-band peak at 1.58μm.

here ULAS 1319+1219 is found to be 0.5 subtypes earlier than Table 2.3. (However, the returned value is still consistent with the error on the values from Table 2.3.) The apparently-negative value for ULAS 1319+1219's $CH_4 - K$ is an artifact of the poor signal-to-noise of the K-band portion of this object's spectrum, an unsurprising result given that $K_{\mathrm{mko}} = 19.4 \pm 0.1$ for this object.

Figure 4.9 shows the object spectra along with the T4 spectral standard 2MASSI J2254+3123 and the T5 standard 2MASS J1503+2525 (Burgasser *et al.* 2006a) where appropriate. ULAS J0926+0835 and ULAS J1233+1219 show K-band suppression relative to the standards, as expected. Perhaps surprisingly, ULAS J1319+1209 actually appears somewhat enhanced in its H-band and not significantly-suppressed in its K-band. The H-band enhancement may not be physical, however; the object's H-band magnitude is 19.2 ± 0.2 mag, a value with a significant error. If the actual magnitude were toward the

Table 4.7: Subaru objects and their spectral typing.

Object	Ratio	Value	Type
ULAS J0926+0835	H_2O-J	0.32±0.02	T4/T5
	CH_4-J	0.53±0.02	T3/T4
	H_2O-H	0.389±0.006	T4
	CH_4-H	0.615±0.006	T3
	CH_4-K	0.20±0.01	T5
		Median type:	T4
ULAS J1233+1219	H_2O-J	0.365±0.007	T4
	CH_4-J	0.528±0.008	T3
	H_2O-H	0.443±0.002	T3
	CH_4-H	0.443±0.002	T5
	CH_4-K	0.133±0.005	T6/T7
		Median type:	T4
ULAS 1319+1219	H_2O-J	0.233±0.009	T5
	CH_4-J	0.322±0.006	T6
	H_2O-H	0.512±0.007	T2
	CH_4-H	0.530±0.007	T4
	CH_4-K	-0.16±0.01	≥T7
		Median type:	T4.5

This table summarises the spectral ratios of the new Subaru spectra. Objects are typed using the system of Burgasser *et al.* (2006a).

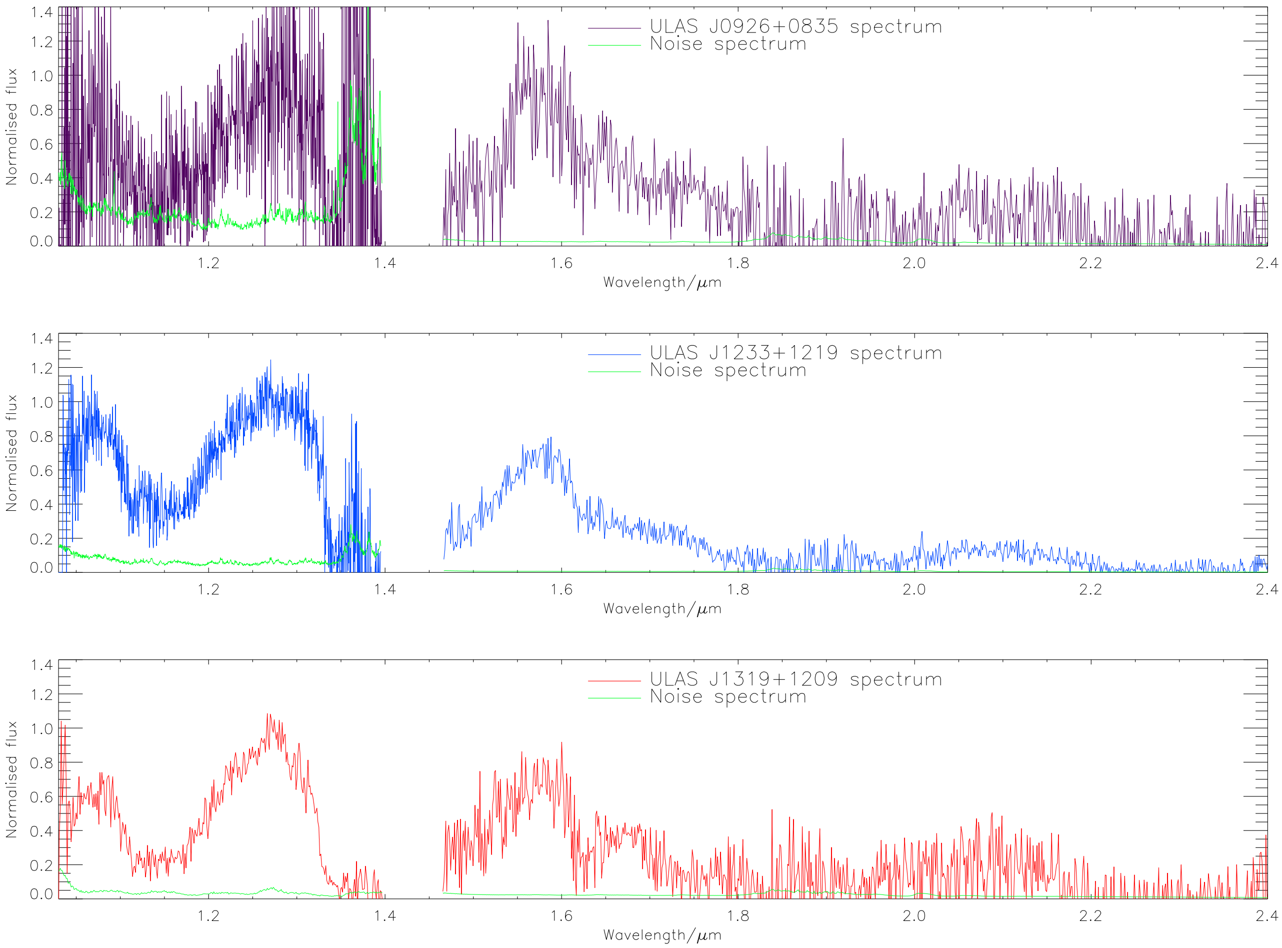

Figure 4.8: This plot shows the *JHK* spectra for ULAS J0926+0835 (top, purple line), ULAS J1233+1219 (middle, blue line) and ULAS J1319+1209 (red line). The error spectra for each are shown in green. Each spectrum has been normalised to the *J*-band peak.

lower end of the range, then the apparent enhancement would disappear. This issue could be clarified through additional follow-up photometry. With regards to the object's *K*-band, this region has an overall signal-to-noise of ∼6.7 between 1.9 and 2.2μm, compared to ∼14.3 for ULAS J1233+1219.

4.3 Chapter Summary

I present several new candidate objects, with photometry, proper motions, *U* and *V* kinematics estimates and, where available, spectra. In addition I present three new *HK* spectra, which in turn have allowed full *JHK* spectroscopy for three blue T dwarfs, and this has also enabled full spectral typing for these objects.

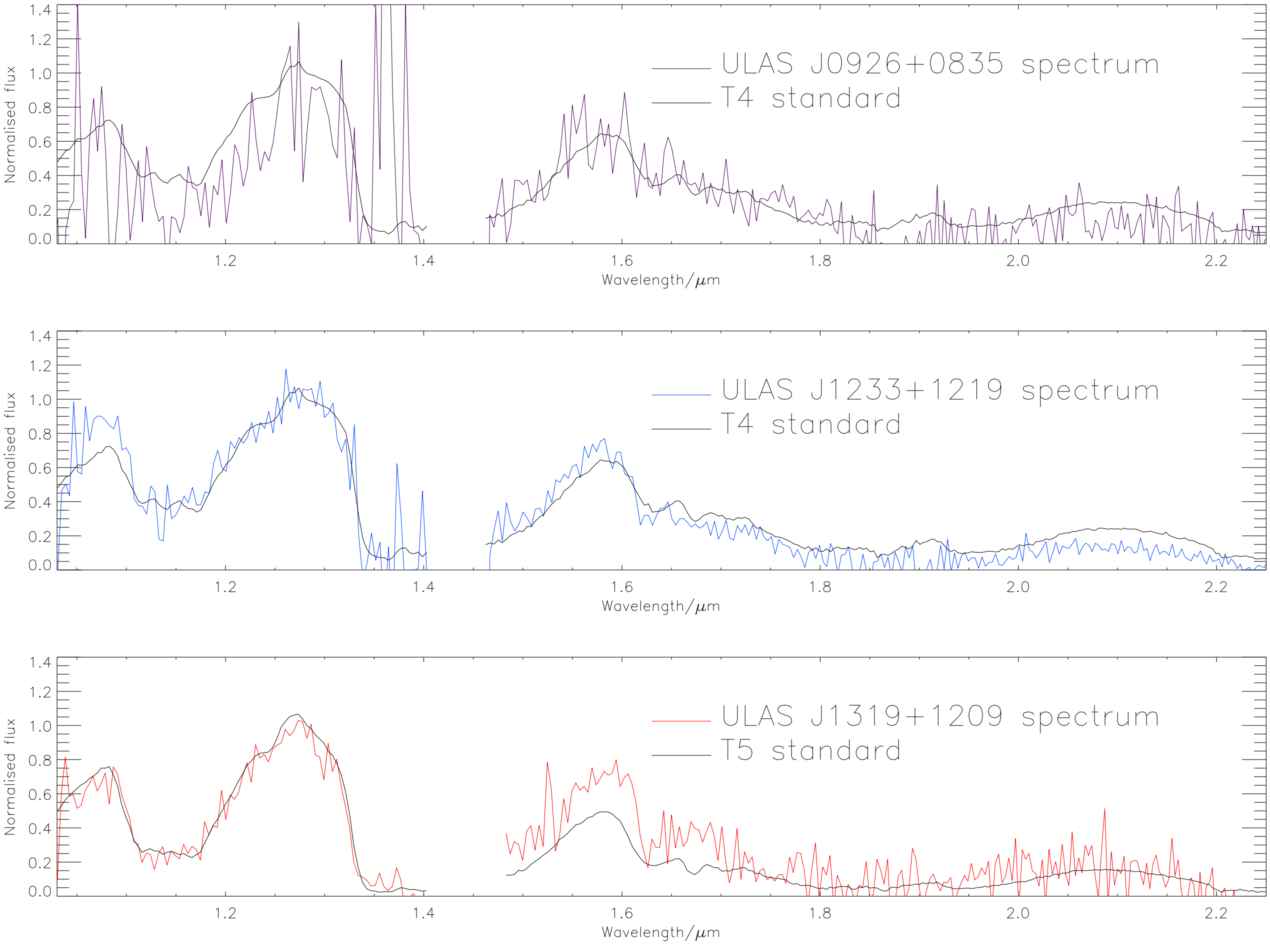

Figure 4.9: This plot shows the three IRCS spectra along with the T4 standard 2MASSI J2254+3123 and the T5 standard 2MASS J1503+2525 (Burgasser *et al.* 2006a). All spectra are normalised to the *J*-band peak, and the IRCS spectra have been splined onto the wavelength scale of the standards.

Chapter 5

Conclusions and Future Work

5.1 Objects and models

Figure 5.1 compares the predicted $H-W2$ colour against the measured colours from WISE for objects in Kirkpatrick *et al.* (2011) and also my selected T dwarfs (those for which $W2$ photometry is available).

Figure 5.2 shows the predictions made by the Burrows models for $H-K$, as compared both to field T dwarfs and to binary benchmarks.

Figure 5.2 and Figure 5.1 show a reasonable agreement between the model predictions and the observed T dwarf colours. However, this does not seem to be the case for the BTSettl model sets.

Figure 5.3 compares the predicted $H-W2$ colours from the BTSettl models, as compared to actual T dwarfs. As can be seen, the BTSettl models are consistently predicting colours that appear to be around ∼0.5 to 1.0 magnitudes too blue.

Figure 5.4 shows the BTSettl models and their colour predictions for the near-infrared. At low $\mathrm{T_{eff}}$s, the models predict colours that are too blue. This problem is particularly bad for low metallicities, and seems to worsen as the metallicity declines. This is also true for even only moderately-subsolar metallicities. This appears to suggest that there still remain problems with the modeling of opacities in low-metallicity atmospheres.

Perhaps surprisingly, the more recent model-set (BTSettl) actually appear to be worse at reproducing the colours of observed objects. Both sets, BTSettl and Burrows, seem to have a tendency to predict colours that are too blue in the near-infrared. However, the BTSettl set seems to be the worst of the two. The problems are particularly acute for

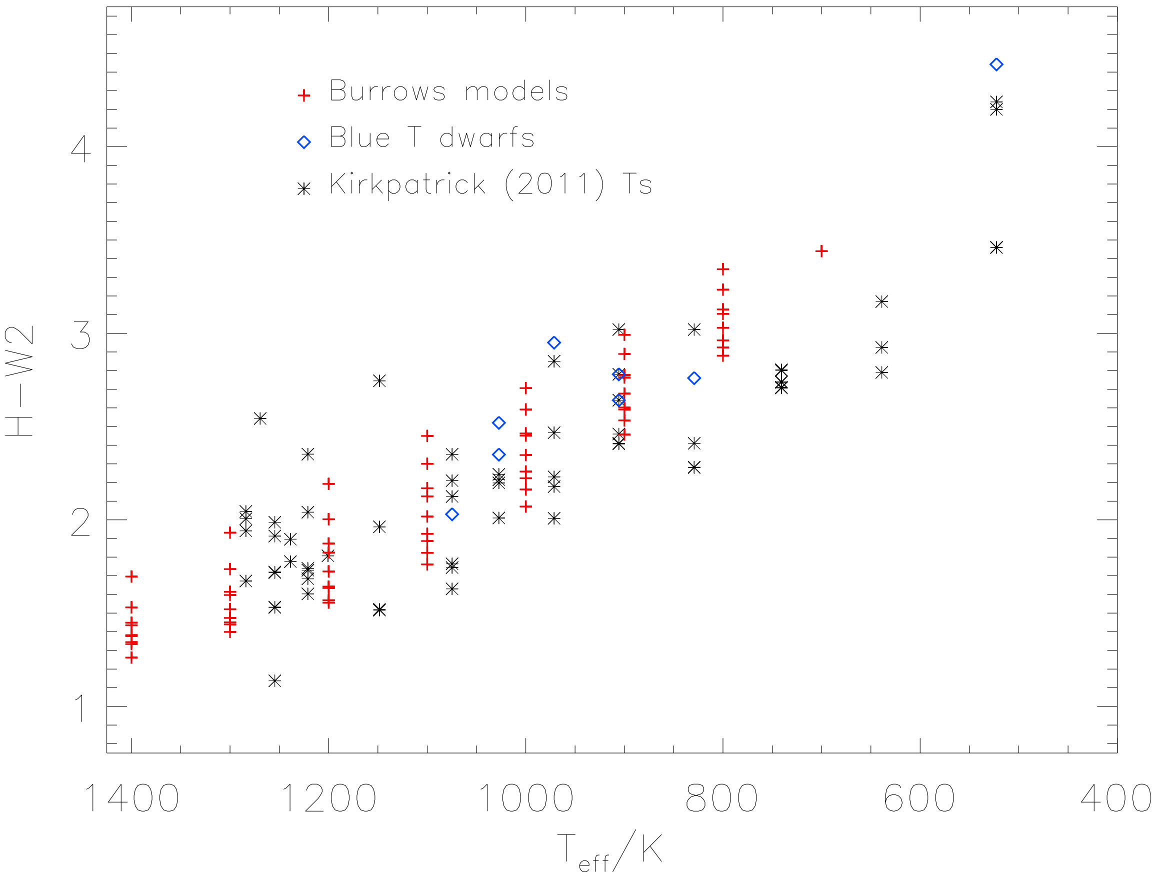

Figure 5.1: A plot showing the mid-infrared colour-predictions for the Burrows models as compared to objects from Kirkpatrick *et al.* (2011).

subsolar metallicities.

In the mid-infrared, the BTSettl models seem to report average-seeming colours for subsolar metallicity, and very blue ones for supersolar metallicity. This also suggests that in the mid-infrared, the predicted colours are all too blue. (Decreasing metallicity should redden $H - W2$, therefore one would expect subsolar metallicity objects to have redder-than-average colours, rather than being merely in the vicinity of the field objects.) These failures of prediction emphasize the need for an expanded census of metal-poor T dwarfs; there clearly are deficiencies in our understanding of the behaviour of low-metallicity atmospheres.

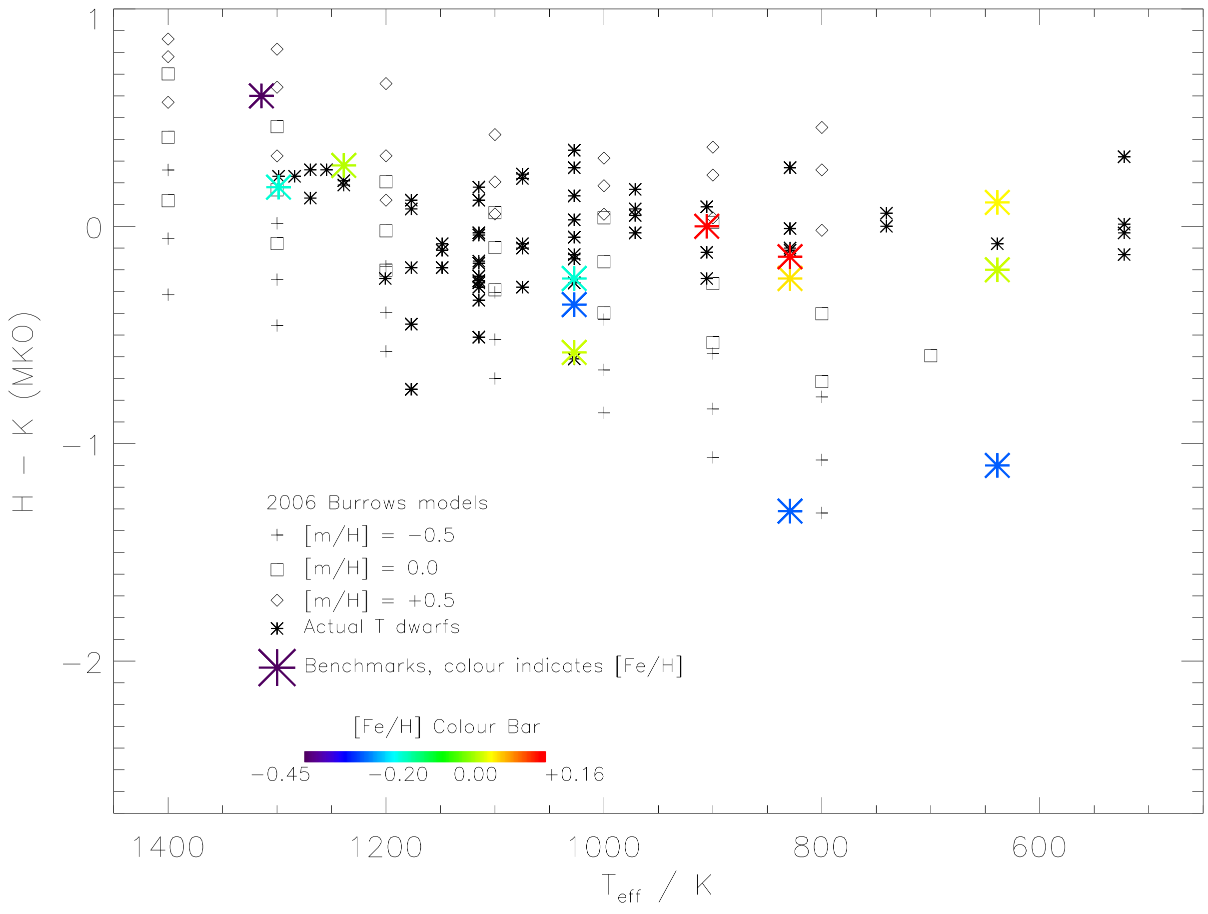

Figure 5.2: A plot showing the $H - K$ colour-predictions for the Burrows models as compared to real objects and binary benchmarks with known metallicities.

5.2 Contamination, biases and completeness

In this section I consider some limiting factors concerning near-infrared surveys and their use in my work. One common source of contamination in near-infrared surveys is M dwarfs which have scattered into the selection area (Burningham *et al.* 2013). This is due to errors on their photometry; a measured value wrong by ∼2- or 3σ is rare in practice, but there are a very large number of red dwarfs; they constitute around ∼75% of all stars. Therefore, even a rare event will occur with some regularity in a sufficiently-large sample.

This is one issue that my work is not strongly-affected by; although candidates are initially selected on the basis of colours, even low-resolution near-infrared J-band spectra are adequate to discriminate between T and M dwarfs. (This is on account of the extremely non-blackbody fluxes exhibited by T dwarfs.) Although some of the candidates derived

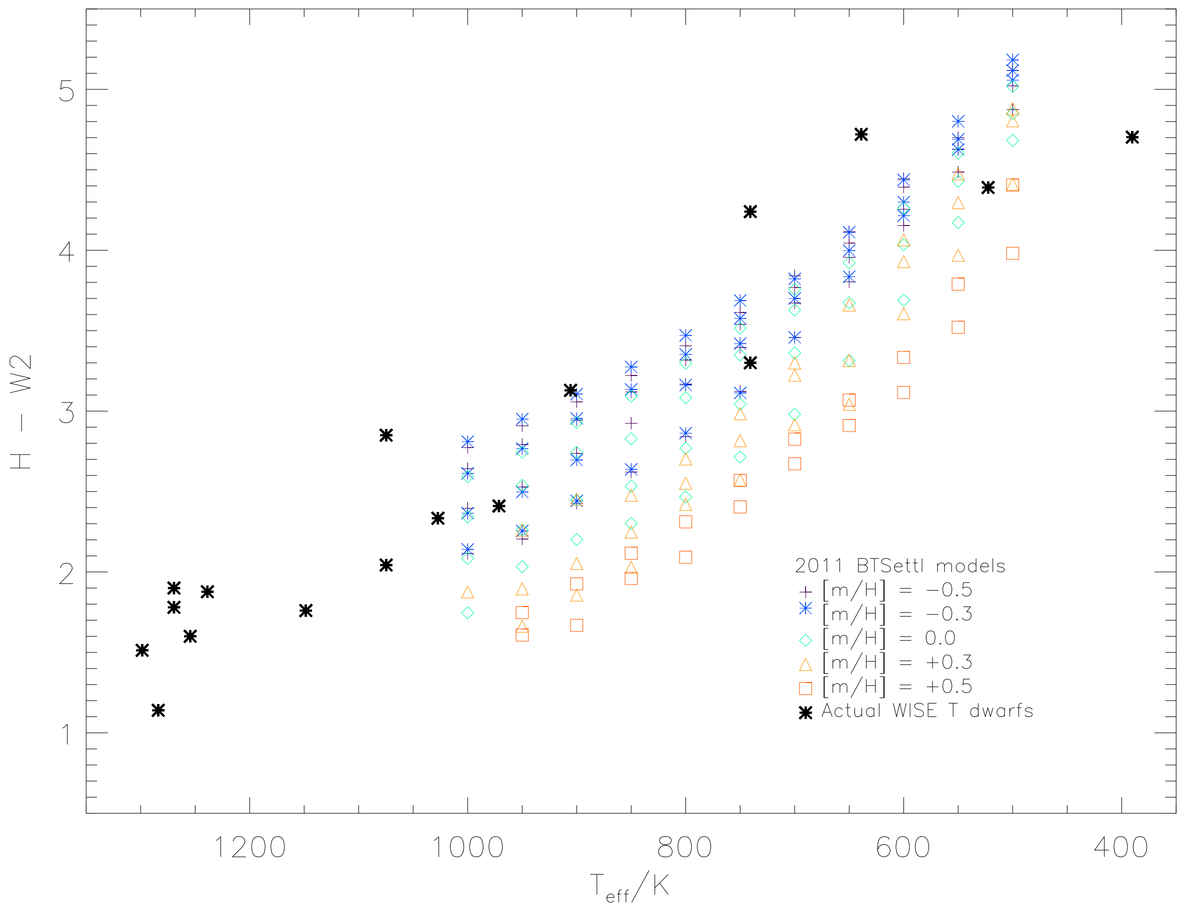

Figure 5.3: A plot showing the mid-infrared colour-predictions for the BTSettl models as compared to real T dwarfs.

from the Smith *et al.* (2013) results do not yet have *JHK* spectra, it will be possible in the future to determine whether or not they are M dwarfs that have photometrically-scattered into our selections.

Another common problem in near-infrared sky surveys is cross-talk. This phenomenon is caused when a too-bright star saturates the CCD chip, resulting in a spill-over of free electrons onto neighbouring regions of the chip. This in turn creates spurious images at these locations. To control for this factor, all images used in my work have been visually inspected for the characteristic donut-shape associated with cross-talk. Any fields that have been subject to this have been disregarded. Also, objects with non-UKIDSS second epoch proper motions are very unlikely to be down to cross-talk; UKIDSS cross-talk would logically not be present in non-UKIDSS second epoch images.

With regard to completeness, in previous work (Murray 2009), I found that the Large

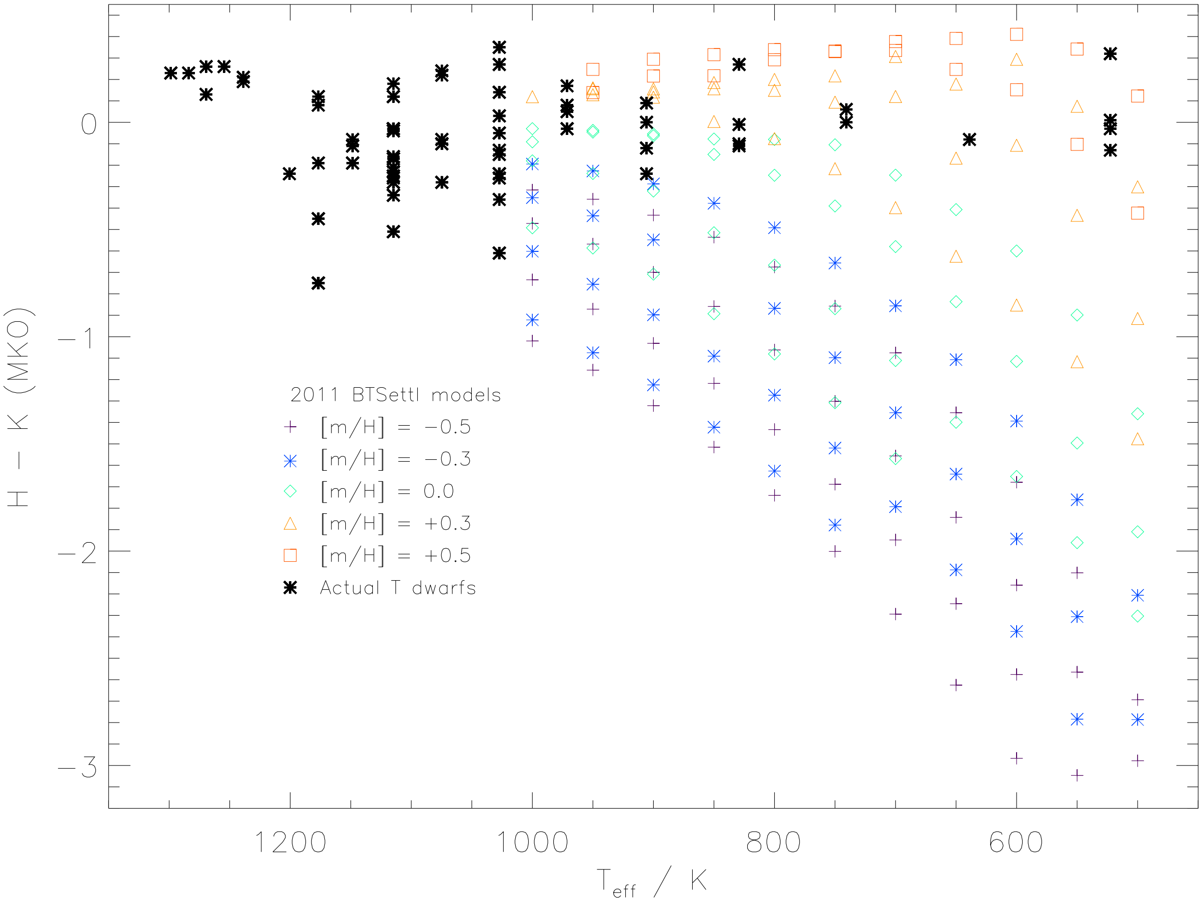

Figure 5.4: A plot showing the $H - K$ colour-predictions for the BTSettl models as compared to real T dwarfs.

Area Survey is complete to around magnitude of $J = \sim 18.2$, after which a turnoff occurs and the survey finds fewer objects. (Theoretically, the 5σ detection limit for the LAS is J=19.6.) Consequently, for objects fainter than this, there is a reasonable likelihood that the LAS will not contain them. Since it seems likely that halo T dwarfs will tend to old, and thus faint, this is a known problem. Also, in practice, this imposes an effective volume-limit on our searches.

Perhaps surprisingly, there is also another problem. Based on my earlier work, I also note that the LAS saturates at magnitudes brighter than $J \sim 13.0$. Luhman (2013) report the discovery of WISE J104915.57531906.1AB, an L-T brown dwarf pair located as close as ∼2 pc from the Sun. Due to their remarkable closeness, these objects have near-infrared magnitudes as bright as $J = 10.68 \pm 0.05$. Consequently, an object such as these would not be properly-detected in the UKIDSS LAS, due to saturation.

One does not expect overly-bright T dwarfs to be a frequent problem, but the existence of the difficulty must be acknowledged nonetheless.

An additional limitation is objects with very high proper motions. This is particularly an issue where epoch differences between first and second images are large. In this case, a very high proper motion object may in fact have moved far enough between fields that it is no longer easily-recognisable, and consequently there may be a risk of falsely discarding the original image as spurious.

A further problem with any survey-based work comes from objects that, through bad positioning on the sky, are unresolved with other objects. There is in fact one such case in my work, namely the ULAS J1416+1348AB binary, where the T dwarf is unresolved from the L dwarf in WISE.

There are two more basic limitations to this work. The first is that the LAS covers a restricted region of the sky, less than 4000 square degrees. Consequently, if a halo T dwarf happened to be located outside of the selection footprint, then it will not be detected. Also, I use a type-restriction requiring objects to be of types later than T4 (to minimise colour uncertainties caused by the L-T transition). However, since there are halo L dwarfs, it seems reasonable to suppose that there can also be halo T0-T4 dwarfs as well; any such objects will not be selected by this work.

5.3 Expectation values for halo T dwarfs

In the Introduction I presented a basic estimate of one range of possible numbers for halo and thick disc brown dwarfs, based on the number of objects present in existing surveys. To recap, this was ∼1254 thin disc brown dwarfs, ∼27 thick disc brown dwarfs and ∼1 halo brown dwarf. DwarfArchives records 918 L dwarfs, 355 T dwarfs and 15 Y dwarfs at the current time. If we assume that this was to split in the above ratios, then one would expect to find 898 thin disc L dwarfs, 19 thick disc L dwarfs and 1 halo L dwarf. For the T dwarfs, one would expect 347 thin disc objects, 7 thick disc objects and less than 1 halo T dwarf. The Y dwarfs would consist entirely of thin disc objects. (The numbers have been rounded to unity, as this is only a very rough estimate.)

Taken at face value, this would suggest that there are not many halo T dwarfs to be found. However, there may be some observational evidence to suggest that these estimates are overly-pessimistic. Zhang *et al.* (2013) report that there already exist 7 confirmed L subdwarfs, to which they have added 3 new confirmed objects, and are examining another

51 candidates. If even only some of these are subsequently confirmed, then the number would easily exceed the above expectation value. A boost in the number of L subdwarfs would also seem to imply a proportionate boost in the number of T subdwarfs as well, as L-type brown dwarfs eventually evolve into T-type brown dwarfs.

5.4 New surveys

In this section, I present some ideas for new surveys to identify possible halo brown dwarfs.

In the current financial climate, sadly it seems rather unlikely that a new instrument could be funded solely to look for brown dwarfs. However it is possible that data from existing and upcoming surveys could be used to look for halo candidates. Although its primary focus is on solar system objects, nonetheless the Pan-STARRS survey is also covering the entire sky down to a limiting magnitude of g_{P1} ∼24. As the survey will be repeatedly covering the entire sky, it should also be able to identify high proper motion objects, such as halo brown dwarfs. Pan-STARRS is somewhat limited for T dwarfs, however, as it is aimed more at objects that are brightest in the optical. Pan-STARR's longest-wavelength band is the Y_{P1}-band filter, which has a limiting magnitude of 20.1 (Dupuy and Liu 2009). T dwarfs are brightest at the J-band, and Pan-STARR's completeness-turnover point will presumably be somewhat shallower than magnitude 20.1 anyway. However, a Pan-STARRS search perhaps based on the $z_{P1} - Y_{P1}$ colour and a suitable proper motion criterion may be able to reveal at least some nearby objects.

Another tool that could be used for this purpose is ESA's GAIA satellite. GAIA will be taking a full sky survey with the intention of mapping all objects down to the 20th magnitude. It will also be determining the distances and space velocities for all these objects, allowing for an actual kinematically-based search. A GAIA-based search may be more promising than Pan-STARRS, as it may be possible to select objects directly on the basis of their kinematics. Also, with parallactic distances it may be possible to derive a set $T_{\rm eff}$/kinematics selection criteria.

Futhermore, there is a a large amount of data currently available in the form of the WISE all-sky releases. A photometric search based on mid-infrared criteria could reveal new objects, and would also be sensitive to cooler/older objects.

Lastly, perhaps building on the Smith *et al.* (2013) kinematics and proper motions work, I would also suggest a UKIDSS-based search for T0-T4 halo candidates.

5.5 Summary of overall results

In this work, a set of candidate metal-poor brown dwarfs are presented. These objects are selected from the UKIDSS LAS using a colour cut of $H - K \leq -0.2$ One of these is the binary companion to LHS 3020, a known metal-poor star (Cenarro *et al.* 2007). This object is important as it confirms that our selection technique is sensitive to metal-poor objects.

Using second-epoch imaging from UKIRT and other sources, we determine proper motions for these objects. The orientation of the LAS is out of the galactic plane; consequently the W component of the UVW space motions for LAS objects is dominated by radial velocity. Therefore we were able to constrain U and V components, even in the absence of radial velocity data. From this, we find that ULAS J0926+0835 has $U = 62 \pm 40\,\mathrm{km\,s^{-1}}$ and $V = -140 \pm 46\,\mathrm{km\,s^{-1}}$, values which make it a candidate halo T dwarf. Another object, ULAS J319+1209, was also identified as a halo candidate. These results were published in Murray *et al.* (2011).

An investigation into the mid-infrared properties of several T dwarfs is also presented. These objects are interesting both due to their extreme colours and also because they may serve as templates for the behaviour of low-metallicity objects such as halo T dwarfs. The investigation detailed here supports the conclusion of Burgasser *et al.* (2008b) that 2MASS J0939-2448 is an unresolved binary. We also support the conclusion that BD+01^o 2920B is a single object. With regards to possible binarity, ULAS J1416+1348B seems to represent an intermediate case between the two other objects.

I present new medium-resolution spectra of 2MASS J0939-2448 and ULAS J1416+1348B. The comparison of Y-bands between these objects and BD+01^o 2920B suggests that 2MASS J0939-2448 has a higher metallicity than the other two, whereas ULAS J1416+1348B is likely to be comparable to that of BD+01^o 2920B. This seems to suggest that an additional factor may be at work in the $H - W2$ colour of ULAS J1416+1348B, as this object is substantially-redder than BD+01^o 2920B, despite equivalent metallicities.

I investigated whether unresolved binarity could be driving the colours of ULAS J1416+1348B, by simulating binaries. I found that the colours do not substantially redden as the unresolved companion cools beyond about T9; this suggests that unresolved binarity alone is not enough to account for the object's $H - W2$.

I also present a radial velocity for ULAS J1416+1348B, as derived from its FIRE spectrum. This velocity is consistent to within the error with the Bowler *et al.* (2010)

value for SDSS J1416+1348A, thus confirming that the two objects are a binary pair. With the parallax measurement to be presented in Murray *et al.* (2013; in press), I derive a luminosity for ULAS J1416+1348B, finding it to be $(6.9 \pm 0.7) \times 10^{20}$ W, or $\log_{10}$ $(L_{\rm obj}/L_{\odot}) = -5.74{\pm}0.04$.

In addition, I provide a further set of candidate metal-poor T dwarfs, drawn from the data from Smith *et al.* (2013). Using these I highlight several more objects with unusual combinations of colours and kinematics. Where available, spectra are presented. I also provide further follow-up for existing objects and their properties.

5.6 Future Work

Future developments for this work include seek moderate- and high-resolution spectroscopy for the halo candidates, and carrying on searching for and identifying new candidate objects.

In addition we will undertake to fit spectral models to the Subaru spectra, in the hope of identifying plausible ranges of metallicity, surface gravity and temperature for these objects.

Chapter 6

Papers based on this work

6.1 First-author papers

Several portions of this work have been submitted and/or published in peer-reviewed journals.

The Introduction was derived from those of Murray *et al.* (2011) and Murray et al. (*MNRAS*; submitted).

Chapter 2 has been published as Murray *et al.* (2011).

Chapter 3 has been submitted to *MNRAS* for publication in 2013.

6.2 Supplementary-author papers

In addition, the research summarised in this thesis has also contributed to several other publications. These are, in order of date:

Pinfield *et al.* (2012);

Burningham *et al.* (2011);

Day-Jones *et al.* (2011);

Burningham *et al.* (2010b);

Burningham *et al.* (2010a);

and Burningham *et al.* (2009).

REFERENCES

Abel, T., Bryan, G. L., and Norman, M. L. (2002). The Formation of the First Star in the Universe. *Science*, **295**, 93–98.

Aguilar, M., Alberti, G., Alpat, B., Alvino, A., Ambrosi, G., Andeen, K., Anderhub, H., Arruda, L., Azzarello, P., Bachlechner, A., and et al. (2013). First Result from the Alpha Magnetic Spectrometer on the International Space Station: Precision Measurement of the Positron Fraction in Primary Cosmic Rays of 0.5-350 GeV. *Physical Review Letters*, **110**(14), 141102.

Alcock, C., Allsman, R. A., Alves, D. R., Axelrod, T. S., Becker, A. C., Bennett, D. P., Cook, K. H., Dalal, N., Drake, A. J., Freeman, K. C., Geha, M., Griest, K., Lehner, M. J., Marshall, S. L., Minniti, D., Nelson, C. A., Peterson, B. A., Popowski, P., Pratt, M. R., Quinn, P. J., Stubbs, C. W., Sutherland, W., Tomaney, A. B., Vandehei, T., and Welch, D. (2000). The MACHO Project: Microlensing Results from 5.7 Years of Large Magellanic Cloud Observations. ApJ, **542**, 281–307.

Allard, F. and Freytag, B. (2010). Brown Dwarf Model Atmospheres Based on Multi-Dimensional Radiation Hydrodynamics. *Highlights of Astronomy*, **15**, 756–756.

Allard, F., Homeier, D., and Freytag, B. (2011). Model Atmospheres From Very Low Mass Stars to Brown Dwarfs. In C. Johns-Krull, M. K. Browning, and A. A. West, editors, *16th Cambridge Workshop on Cool Stars, Stellar Systems, and the Sun*, volume 448 of *Astronomical Society of the Pacific Conference Series*, page 91.

Allard, N. F., Allard, F., Hauschildt, P. H., Kielkopf, J. F., and Machin, L. (2003). A new model for brown dwarf spectra including accurate unified line shape theory for the Na I and K I resonance line profiles. A&A, **411**, L473–L476.

Allen, P. R., Koerner, D. W., Reid, I. N., and Trilling, D. E. (2005). The Substellar Mass Function: A Bayesian Approach. ApJ, **625**, 385–397.

Aller, K. M., Kraus, A. L., Liu, M. C., Burgett, W. S., Chambers, K. C., Hodapp, K. W., Kaiser, N., Magnier, E. A., and Price, P. A. (2013). A Pan-STARRS + UKIDSS Search for Young, Wide Planetary-mass Companions in Upper Scorpius. ApJ, **773**, 63.

Asplund, M., Grevesse, N., Sauval, A. J., and Scott, P. (2009). The Chemical Composition of the Sun. ARA&A, **47**, 481–522.

Bahcall, J. N. (1984). K giants and the total amount of matter near the sun. ApJ, **287**, 926–944.

Baraffe, I., Chabrier, G., Barman, T. S., Allard, F., and Hauschildt, P. H. (2003). Evolutionary models for cool brown dwarfs and extrasolar giant planets. The case of HD 209458. A&A, **402**, 701–712.

Barbier-Brossat, M. and Figon, P. (2000). Catalogue général de vitesses radiales moyennes pour les étoiles galactiques. Mean radial velocities catalog of galactic stars. A&AS, **142**, 217–223.

Basri, G., Marcy, G. W., and Graham, J. R. (1996). Lithium in Brown Dwarf Candidates: The Mass and Age of the Faintest Pleiades Stars. ApJ, **458**, 600.

Bate, M. R. (2005). The dependence of the initial mass function on metallicity and the opacity limit for fragmentation. MNRAS, **363**, 363–378.

Bensby, T., Feltzing, S., and Lundström, I. (2003). Elemental abundance trends in the Galactic thin and thick disks as traced by nearby F and G dwarf stars. A&A, **410**, 527–551.

Bochanski, J. J., Hennawi, J. F., Simcoe, R. A., Prochaska, J. X., West, A. A., Burgasser, A. J., Burles, S. M., and et al. (2009). MASE: A New Data-Reduction Pipeline for the Magellan Echellette Spectrograph. PASP, **121**, 1409–1418.

Bochanski, J. J., Burgasser, A. J., Simcoe, R. A., and West, A. A. (2011). FIRE Spectroscopy of the Ultra-cool Brown Dwarf, UGPS J072227.51-054031.2: Kinematics, Rotation and Atmospheric Parameters. AJ, **142**, 169.

Boffin, H. M. J., Watkins, S. J., Bhattal, A. S., Francis, N., and Whitworth, A. P. (1998). Numerical simulations of protostellar encounters - I. Star-disc encounters. MNRAS, **300**, 1189–1204.

Borysow, A., Jorgensen, U. G., and Zheng, C. (1997). Model atmospheres of cool, low-metallicity stars: the importance of collision-induced absorption. A&A, **324**, 185–195.

Bowler, B. P., Liu, M. C., and Dupuy, T. J. (2010). SDSS J141624.08+134826.7: A Nearby Blue L Dwarf From the Sloan Digital Sky Survey. ApJ, **710**, 45–50.

Burgasser, A. J. (2004). T Dwarfs and the Substellar Mass Function. I. Monte Carlo Simulations. ApJS, **155**, 191–207.

Burgasser, A. J., Kirkpatrick, J. D., Brown, M. E., Reid, I. N., Gizis, J. E., Dahn, C. C., Monet, D. G., and et al. (1999). Discovery of Four Field Methane (T-Type) Dwarfs with the Two Micron All-Sky Survey. ApJ, **522**, L65–L68.

Burgasser, A. J., Wilson, J. C., Kirkpatrick, J. D., Skrutskie, M. F., Colonno, M. R., Enos, A. T., Smith, J. D., and et al. (2000). Discovery of a Bright Field Methane (T-Type) Brown Dwarf by 2MASS. AJ, **120**, 1100–1105.

Burgasser, A. J., Kirkpatrick, J. D., Brown, M. E., Reid, I. N., Burrows, A., Liebert, J., and et al (2002). The Spectra of T Dwarfs. I. Near-Infrared Data and Spectral Classification. ApJ, **564**, 421–451.

Burgasser, A. J., Kirkpatrick, J. D., Liebert, J., and Burrows, A. (2003). The Spectra of T Dwarfs. II. Red Optical Data. ApJ, **594**, 510–524.

Burgasser, A. J., McElwain, M. W., Kirkpatrick, J. D., Cruz, K. L., Tinney, C. G., and Reid, I. N. (2004). The 2MASS Wide-Field T Dwarf Search. III. Seven New T Dwarfs and Other Cool Dwarf Discoveries. AJ, **127**, 2856–2870.

Burgasser, A. J., Burrows, A., and Kirkpatrick, J. D. (2006a). A Method for Determining the Physical Properties of the Coldest Known Brown Dwarfs. ApJ, **639**, 1095–1113.

Burgasser, A. J., Geballe, T. R., Leggett, S. K., Kirkpatrick, J. D., and Golimowski, D. A. (2006b). A Unified Near-Infrared Spectral Classification Scheme for T Dwarfs. ApJ, **637**, 1067–1093.

Burgasser, A. J., Tinney, C. G., Cushing, M. C., Saumon, D., Marley, M. S., Bennett, C. S., and Kirkpatrick, J. D. (2008a). 2MASS J09393548-2448279: The Coldest and Least Luminous Brown Dwarf Binary Known? ApJ, **689**, L53–L56.

Burgasser, A. J., Tinney, C. G., Cushing, M. C., Saumon, D., Marley, M. S., Bennett, C. S., and Kirkpatrick, J. D. (2008b). 2MASS J09393548-2448279: The Coldest and Least Luminous Brown Dwarf Binary Known? ApJ, **689**, L53–L56.

Burgasser, A. J., Cushing, M. C., Kirkpatrick, J. D., Gelino, C. R., Griffith, R. L., Looper, D. L., Tinney, C., and et al. (2011). Fire Spectroscopy of Five Late-type T Dwarfs Discovered with the Wide-field Infrared Survey Explorer. ApJ, **735**, 116.

Burningham, B., Pinfield, D. J., Leggett, S. K., Tamura, M., Lucas, P. W., Homeier, D., Day-Jones, A., and et al. (2008). Exploring the substellar temperature regime down to ˜550K. MNRAS, **391**, 320–333.

Burningham, B., Pinfield, D. J., Leggett, S. K., Tinney, C. G., Liu, M. C., Homeier, D., West, A. A., and et al. (2009). The discovery of an M4+T8.5 binary system. MNRAS, **395**, 1237–1248.

Burningham, B., Pinfield, D. J., Lucas, P. W., Leggett, S. K., Deacon, N. R., Tamura, M., Tinney, C. G., and et al. (2010a). 47 new T dwarfs from the UKIDSS Large Area Survey. MNRAS, **406**, 1885–1906.

Burningham, B., Leggett, S. K., Lucas, P. W., Pinfield, D. J., Smart, R. L., Day-Jones, A. C., Jones, H. R. A., and et al. (2010b). The discovery of a very cool binary system. MNRAS, pages 1952–1961.

Burningham, B., Leggett, S. K., Homeier, D., Saumon, D., Lucas, P. W., Pinfield, D. J., Tinney, C. G., Allard, F., Marley, M. S., Jones, H. R. A., Murray, D. N., Ishii, M., Day-Jones, A., Gomes, J., and Zhang, Z. H. (2011). The properties of the T8.5p dwarf Ross 458C. MNRAS, **414**, 3590–3598.

Burningham, B., Cardoso, C. V., Smith, L., Leggett, S. K., Smart, R. L., Mann, A. W., Dhital, S., Lucas, P. W., Tinney, C. G., Pinfield, D. J., Zhang, Z., Morley, C., Saumon, D., Aller, K., Littlefair, S. P., Homeier, D., Lodieu, N., Deacon, N., Marley, M. S., van Spaandonk, L., Baker, D., Allard, F., Andrei, A. H., Canty, J., Clarke, J., Day-Jones, A. C., Dupuy, T., Fortney, J. J., Gomes, J., Ishii, M., Jones, H. R. A., Liu, M., Magazzú, A., Marocco, F., Murray, D. N., Rojas-Ayala, B., and Tamura, M. (2013). 76 T dwarfs from the UKIDSS LAS: benchmarks, kinematics and an updated space density. MNRAS.

Burrows, A. and Liebert, J. (1993). The science of brown dwarfs. *Reviews of Modern Physics*, **65**, 301–336.

Burrows, A. and Sharp, C. M. (1999). Chemical Equilibrium Abundances in Brown Dwarf and Extrasolar Giant Planet Atmospheres. ApJ, **512**, 843–863.

Burrows, A. and Volobuyev, M. (2003). Calculations of the Far-Wing Line Profiles of Sodium and Potassium in the Atmospheres of Substellar-Mass Objects. ApJ, **583**, 985–995.

Burrows, A., Hubbard, W. B., Lunine, J. I., and Liebert, J. (2001). The theory of brown dwarfs and extrasolar giant planets. *Reviews of Modern Physics*, **73**, 719–765.

Burrows, A., Sudarsky, D., and Hubeny, I. (2006). L and T Dwarf Models and the L to T Transition. ApJ, **640**, 1063–1077.

Burrows, A., Heng, K., and Nampaisarn, T. (2011). The Dependence of Brown Dwarf Radii on Atmospheric Metallicity and Clouds: Theory and Comparison with Observations. ApJ, **736**, 47.

Buzzoni, B., Delabre, B., Dekker, H., Dodorico, S., Enard, D., Focardi, P., Gustafsson, B., Nees, W., Paureau, J., and Reiss, R. (1984). The ESO Faint Object Spectrograph and Camera (EFOSC). *The Messenger*, **38**, 9–13.

Carroll, B. W. and Ostlie, D. A. (1996). *An Introduction to Modern Astrophysics*.

Casali, M., Adamson, A., Alves de Oliveira, C., Almaini, O., Burch, K., Chuter, T., Elliot, J., and et al (2007). The UKIRT wide-field camera. A&A, **467**, 777–784.

Cenarro, A. J., Peletier, R. F., Sánchez-Blázquez, P., Selam, S. O., Toloba, E., Cardiel, N., Falcón-Barroso, J., and et al (2007). Medium-resolution Isaac Newton Telescope library of empirical spectra - II. The stellar atmospheric parameters. MNRAS, **374**, 664–690.

Chandrasekhar, S. (1939). *An introduction to the study of stellar structure*.

Chiba, M. and Beers, T. C. (2000). Kinematics of Metal-poor Stars in the Galaxy. III. Formation of the Stellar Halo and Thick Disk as Revealed from a Large Sample of Nonkinematically Selected Stars. AJ, **119**, 2843–2865.

Chiu, K., Fan, X., Leggett, S. K., Golimowski, D. A., Zheng, W., Geballe, T. R., Schneider, D. P., and Brinkmann, J. (2006). Seventy-One New L and T Dwarfs from the Sloan Digital Sky Survey. AJ, **131**, 2722–2736.

Cushing, M. C., Vacca, W. D., and Rayner, J. T. (2004). Spextool: A Spectral Extraction Package for SpeX, a 0.8-5.5 Micron Cross-Dispersed Spectrograph. PASP, **116**, 362–376.

Cushing, M. C., Kirkpatrick, J. D., Gelino, C. R., Griffith, R. L., Skrutskie, M. F., Mainzer, A., Marsh, K. A., and et al. (2011). The Discovery of Y Dwarfs using Data from the Wide-field Infrared Survey Explorer (WISE). ApJ, **743**, 50.

Cutri, R. M., Skrutskie, M. F., van Dyk, S., Beichman, C. A., Carpenter, J. M., Chester, T., Cambresy, L., and et al. (2003). *2MASS All Sky Catalog of point sources*.

Day-Jones, A. C., Pinfield, D. J., Napiwotzki, R., Burningham, B., Jenkins, J. S., Jones, H. R. A., Folkes, S. L., and et al. (2008). Discovery of a widely separated ultracool dwarf-white dwarf binary. MNRAS, **388**, 838–848.

Day-Jones, A. C., Pinfield, D. J., Ruiz, M. T., Beaumont, H., Burningham, B., Gallardo, J., Gianninas, A., Bergeron, P., Napiwotzki, R., Jenkins, J. S., Zhang, Z. H., Murray, D. N., Catalán, S., and Gomes, J. (2011). Discovery of a T dwarf + white dwarf binary system. MNRAS, **410**, 705–716.

Day-Jones, A. C., Marocco, F., Pinfield, D. J., Zhang, Z. H., Burningham, B., Deacon, N., Ruiz, M. T., Gallardo, J., Jones, H. R. A., Lucas, P. W. L., Jenkins, J. S., Gomes, J., Folkes, S. L., and Clarke, J. R. A. (2013). The sub-stellar birth rate from UKIDSS. MNRAS, **430**, 1171–1187.

Deacon, N. R., Liu, M. C., Magnier, E. A., Bowler, B. P., Redstone, J., Goldman, B., Burgett, W. S., and et al (2011). HIP 38939B: A New Benchmark T Dwarf in the Galactic Plane Discovered with Pan-STARRS1. *ArXiv e-prints*.

Dekker, H., Delabre, B., and Dodorico, S. (1986). ESO's Multimode Instrument for the Nasmyth focus of the 3.5 M New Technology Telescope. In D. L. Crawford, editor, *Society of Photo-Optical Instrumentation Engineers (SPIE) Conference Series*, volume 627 of *Society of Photo-Optical Instrumentation Engineers (SPIE) Conference Series*, pages 339–348.

del Peloso, E. F., da Silva, L., and Arany-Prado, L. I. (2005). The age of the Galactic thin disk from Th/Eu nucleocosmochronology. II. Chronological analysis. A&A, **434**, 301–308.

Dupuy, T. J. and Liu, M. C. (2009). Detectability of Transiting Jupiters and Low-Mass Eclipsing Binaries in Sparsely Sampled Pan-STARRS-1 Survey Data. ApJ, **704**, 1519–1537.

Dupuy, T. J. and Liu, M. C. (2012). The Hawaii Infrared Parallax Program. I. Ultracool Binaries and the L/T Transition. *ArXiv e-prints*.

Edvardsson, B., Andersen, J., Gustafsson, B., Lambert, D. L., Nissen, P. E., and Tomkin, J. (1993). The Chemical Evolution of the Galactic Disk - Part One - Analysis and Results. A&A, **275**, 101.

Evans, D. S. (1967). The Revision of the General Catalogue of Radial Velocities. In A. H. Batten & J. F. Heard, editor, *Determination of Radial Velocities and their Applications*, volume 30 of *IAU Symposium*, pages 57–+.

Fegley, Jr., B. and Lodders, K. (1996). Atmospheric Chemistry of the Brown Dwarf Gliese 229B: Thermochemical Equilibrium Predictions. ApJ, **472**, L37.

Feltzing, S. and Gustafsson, B. (1998). Abundances in metal-rich stars. Detailed abundance analysis of 47 G and K dwarf stars with [Me/H] gt 0.10 dex. A&AS, **129**, 237–266.

Frebel, A., Collet, R., Eriksson, K., Christlieb, N., and Aoki, W. (2008). HE 1327-2326, an Unevolved Star with [Fe/H]¡-5.0. II. New 3D-1D Corrected Abundances from a Very Large Telescope UVES Spectrum. ApJ, **684**, 588–602.

Fuhrmann, K. (1998). Nearby stars of the Galactic disk and halo. A&A, **338**, 161–183.

Fuhrmann, K. (2004). Nearby stars of the Galactic disk and halo. III. *Astronomische Nachrichten*, **325**, 3–80.

Geballe, T. R., Saumon, D., Leggett, S. K., Knapp, G. R., Marley, M. S., and Lodders, K. (2001). Infrared Observations and Modeling of One of the Coolest T Dwarfs: Gliese 570D. ApJ, **556**, 373–379.

Geballe, T. R., Knapp, G. R., Leggett, S. K., Fan, X., Golimowski, D. A., Anderson, S., Brinkmann, J., and et al. (2002). Toward Spectral Classification of L and T Dwarfs: Infrared and Optical Spectroscopy and Analysis. ApJ, **564**, 466–481.

Gilmore, G. and Reid, N. (1983). New light on faint stars. III - Galactic structure towards the South Pole and the Galactic thick disc. MNRAS, **202**, 1025–1047.

Gizis, J. E. (1997). M-Subdwarfs: Spectroscopic Classification and the Metallicity Scale. AJ, **113**, 806–822.

Gizis, J. E., Reid, I. N., Knapp, G. R., Liebert, J., Kirkpatrick, J. D., Koerner, D. W., and Burgasser, A. J. (2003). Hubble Space Telescope Observations of Binary Very Low Mass Stars and Brown Dwarfs. AJ, **125**, 3302–3310.

Golimowski, D. A., Leggett, S. K., Marley, M. S., Fan, X., Geballe, T. R., Knapp, G. R., Vrba, F. J., and et al. (2004). L' and M' Photometry of Ultracool Dwarfs. AJ, **127**, 3516–3536.

Gray, R. O., Corbally, C. J., Garrison, R. F., McFadden, M. T., and Robinson, P. E. (2003). Contributions to the Nearby Stars (NStars) Project: Spectroscopy of Stars Earlier than M0 within 40 Parsecs: The Northern Sample. I. AJ, **126**, 2048–2059.

Grossman, A. S. (1970). Evolution of Low-Mass Stars. I. Contraction to the Main Sequence. ApJ, **161**, 619.

Hambly, N. C., Collins, R. S., Cross, N. J. G., Mann, R. G., Read, M. A., Sutorius, E. T. W., Bond, I., and et al (2008). The WFCAM Science Archive. MNRAS, **384**, 637–662.

Haywood, M. (2001). A revision of the solar neighbourhood metallicity distribution. MNRAS, **325**, 1365–1382.

Haywood, M., Di Matteo, P., Lehnert, M., Katz, D., and Gomez, A. (2013). The age structure of stellar populations in the solar vicinity. Clues of a two-phase formation history of the Milky Way disk. *ArXiv e-prints*.

Henry, T. J., Soderblom, D. R., Donahue, R. A., and Baliunas, S. L. (1996). A Survey of Ca II H and K Chromospheric Emission in Southern Solar-Type Stars. AJ, **111**, 439–+.

Hodapp, K. W., Jensen, J. B., Irwin, E. M., Yamada, H., Chung, R., Fletcher, K., Robertson, L., and et al (2003). The Gemini Near-Infrared Imager (NIRI). PASP, **115**, 1388–1406.

Holmberg, J., Nordström, B., and Andersen, J. (2009). The Geneva-Copenhagen survey of the solar neighbourhood. III. Improved distances, ages, and kinematics. A&A, **501**, 941–947.

Irwin, M. J., Lewis, J., Hodgkin, S., Bunclark, P., Evans, D., McMahon, R., Emerson, J. P., and et al. (2004). VISTA data flow system: pipeline processing for WFCAM and VISTA. In P. J. Quinn & A. Bridger, editor, *Society of Photo-Optical Instrumentation Engineers (SPIE) Conference Series*, volume 5493 of *Society of Photo-Optical Instrumentation Engineers (SPIE) Conference Series*, pages 411–422.

Jenkins, J. S., Jones, H. R. A., Pavlenko, Y., Pinfield, D. J., Barnes, J. R., and Lyubchik, Y. (2008). Metallicities and activities of southern stars. A&A, **485**, 571–584.

Jurić, M., Ivezić, Ž., Brooks, A., Lupton, R. H., Schlegel, D., Finkbeiner, D., Padmanabhan, N., Bond, N., Sesar, B., Rockosi, C. M., Knapp, G. R., Gunn, J. E., Sumi, T., Schneider, D. P., Barentine, J. C., Brewington, H. J., Brinkmann, J., Fukugita, M., Harvanek, M., Kleinman, S. J., Krzesinski, J., Long, D., Neilsen, Jr., E. H., Nitta, A., Snedden, S. A., and York, D. G. (2008). The Milky Way Tomography with SDSS. I. Stellar Number Density Distribution. ApJ, **673**, 864–914.

King, R. R., McCaughrean, M. J., Homeier, D., Allard, F., Scholz, R.-D., and Lodieu, N. (2010). ϵ Indi Ba, Bb: a detailed study of the nearest known brown dwarfs. A&A, **510**, A99+.

Kirkpatrick, J. D., Cushing, M. C., Gelino, C. R., Griffith, R. L., Skrutskie, M. F., Marsh, K. A., Wright, E. L., Mainzer, A., Eisenhardt, P. R., McLean, I. S., Thompson, M. A., Bauer, J. M., Benford, D. J., Bridge, C. R., Lake, S. E., Petty, S. M., Stanford, S. A., Tsai, C.-W., Bailey, V., Beichman, C. A., Bloom, J. S., Bochanski, J. J., Burgasser, A. J., Capak, P. L., Cruz, K. L., Hinz, P. M., Kartaltepe, J. S., Knox, R. P., Manohar, S., Masters, D., Morales-Calderón, M., Prato, L. A., Rodigas, T. J., Salvato, M., Schurr, S. D., Scoville, N. Z., Simcoe, R. A., Stapelfeldt, K. R., Stern, D., Stock, N. D., and Vacca, W. D. (2011). The First Hundred Brown Dwarfs Discovered by the Wide-field Infrared Survey Explorer (WISE). ApJS, **197**, 19.

Kirkpatrick, J. D., Gelino, C. R., Cushing, M. C., Mace, G. N., Griffith, R. L., Skrutskie, M. F., Marsh, K. A., and et al. (2012). Further Defining Spectral Type "Y" and Exploring the Low-mass End of the Field Brown Dwarf Mass Function. ApJ, **753**, 156.

Knapp, G. R., Leggett, S. K., Fan, X., Marley, M. S., Geballe, T. R., Golimowski, D. A., Finkbeiner, D., and et al. (2004). Near-Infrared Photometry and Spectroscopy of L and T Dwarfs: The Effects of Temperature, Clouds, and Gravity. AJ, **127**, 3553–3578.

Kobayashi, N., Tokunaga, A. T., Terada, H., Goto, M., Weber, M., Potter, R., Onaka, P. M., Ching, G. K., Young, T. T., Fletcher, K., Neil, D., Robertson, L., Cook, D., Imanishi, M., and Warren, D. W. (2000). IRCS: infrared camera and spectrograph for the Subaru Telescope. In M. Iye and A. F. Moorwood, editors, *Society of Photo-Optical Instrumentation Engineers (SPIE) Conference Series*, volume 4008 of *Society of Photo-Optical Instrumentation Engineers (SPIE) Conference Series*, pages 1056–1066.

Kroupa, P., Tout, C. A., and Gilmore, G. (1990). The low-luminosity stellar mass function. MNRAS, **244**, 76–85.

Kroupa, P., Tout, C. A., and Gilmore, G. (1993). The distribution of low-mass stars in the Galactic disc. MNRAS, **262**, 545–587.

Kumar, S. S. (1963). The Structure of Stars of Very Low Mass. ApJ, **137**, 1121–+.

Lawrence, A., Warren, S. J., Almaini, O., Edge, A. C., Hambly, N. C., Jameson, R. F., Lucas, P., and et al. (2007). The UKIRT Infrared Deep Sky Survey (UKIDSS). MNRAS, **379**, 1599–1617.

Leggett, S. K., Allard, F., Dahn, C., Hauschildt, P. H., Kerr, T. H., and Rayner, J. (2000). Spectral Energy Distributions for Disk and Halo M Dwarfs. ApJ, **535**, 965–974.

Leggett, S. K., Marley, M. S., Freedman, R., Saumon, D., Liu, M. C., Geballe, T. R., and et al (2007). Physical and Spectral Characteristics of the T8 and Later Type Dwarfs. ApJ, **667**, 537–548.

Leggett, S. K., Cushing, M. C., Saumon, D., Marley, M. S., Roellig, T. L., Warren, S. J., Burningham, B., and et al. (2009). The Physical Properties of Four ˜600 K T Dwarfs. ApJ, **695**, 1517–1526.

Leggett, S. K., Albert, L., Artigau, E., Burningham, B., Delfosse, X., Delorme, P., Forveille, T., and et al. (2010). Spitzer Mid-Infrared Photometry of 500 - 750 K Brown Dwarfs. *ArXiv e-prints*.

Limber, D. N. (1958). The Structure of the M Dwarf Stars. I. ApJ, **127**, 363.

Linsky, J. L. (1969). On the Pressure-Induced Opacity of Molecular Hydrogen in Late-Type Stars. ApJ, **156**, 989–+.

Liu, M. C., Leggett, S. K., and Chiu, K. (2007). The Late-T Dwarf Companion to the Exoplanet Host Star HD 3651: A New Benchmark for Gravity and Metallicity Effects in Ultracool Spectra. ApJ, **660**, 1507–1516.

Lodieu, N., Pinfield, D. J., Leggett, S. K., Jameson, R. F., Mortlock, D. J., Warren, S. J., and et al. (2007). Eight new T4.5-T7.5 dwarfs discovered in the UKIDSS Large Area Survey Data Release 1. MNRAS, **379**, 1423–1430.

Lucas, P. W., Tinney, C. G., Burningham, B., Leggett, S. K., Pinfield, D. J., Smart, R., Jones, H. R. A., and et al. (2010). The discovery of a very cool, very nearby brown dwarf in the Galactic plane. MNRAS, **408**, L56–L60.

Luhman, K. L. (2013). Discovery of a Binary Brown Dwarf at 2pc from the Sun. ApJ, **767**, L1.

Luyten, W. J. (1979). *LHS Catalogue. Second edition.*

Mainzer, A., Cushing, M. C., Skrutskie, M., Gelino, C. R., Kirkpatrick, J. D., Jarrett, T., Masci, F., and et al. (2011). The First Ultra-cool Brown Dwarf Discovered by the Wide-field Infrared Survey Explorer. ApJ, **726**, 30–+.

Mamajek, E. E. and Hillenbrand, L. A. (2008). Improved Age Estimation for Solar-Type Dwarfs Using Activity-Rotation Diagnostics. ApJ, **687**, 1264–1293.

Manchado, A., Manchado, A., Barreto, M., Acosta-Pulido, J., Prada, F., Domínguez-Tagle, C., Correa, S., and et al (2003). LIRIS (Long-slit Intermediate Resolution Infrared Spectrograph) Project status. In J. M. Rodriguez Espinoza, F. Garzon Lopez, & V. Melo Martin, editor, *Revista Mexicana de Astronomia y Astrofisica Conference Series*, volume 16 of *Revista Mexicana de Astronomia y Astrofisica Conference Series*, pages 43–45.

Marcy, G. W. and Butler, R. P. (2000). Planets Orbiting Other Suns. PASP, **112**, 137–140.

Markevitch, M., Gonzalez, A. H., Clowe, D., Vikhlinin, A., Forman, W., Jones, C., Murray, S., and Tucker, W. (2004). Direct Constraints on the Dark Matter Self-Interaction Cross Section from the Merging Galaxy Cluster 1E 0657-56. ApJ, **606**, 819–824.

Marocco, F., Smart, R. L., Jones, H. R. A., Burningham, B., Lattanzi, M. G., Leggett, S. K., Lucas, P. W., and et al (2010). Parallaxes and physical properties of 11 mid-to-late T dwarfs. A&A, **524**, A38+.

Mashonkina, L. and Gehren, T. (2001). Heavy element abundances in cool dwarf stars: An implication for the evolution of the Galaxy. A&A, **376**, 232–247.

McCuskey, S. W. (1983). Space distribution of stars in the southern Milky Way. III - A region in Centaurus-Crux. AJ, **88**, 1175–1181.

Miller, G. E. and Scalo, J. M. (1979). The initial mass function and stellar birthrate in the solar neighborhood. ApJS, **41**, 513–547.

Monet, D. G., Levine, S. E., Canzian, B., Ables, H. D., Bird, A. R., Dahn, C. C., Guetter, H. H., and et al. (2003). The USNO-B Catalog. AJ, **125**, 984–993.

Mould, J. R. and Hyland, A. R. (1976). Infrared observations and the structure of the lower main sequence. ApJ, **208**, 399–413.

Mountain, C. M., Selby, M. J., Leggett, S. K., Blackwell, D. E., and Petford, A. D. (1985). Measurement of the absolute flux from VEGA at 4.92 microns. A&A, **151**, 399–402.

Murray, D. N. (2009). *Finding Ultracool Subdwarfs Using UKIDSS.*

Murray, D. N., Burningham, B., Jones, H. R. A., Pinfield, D. J., Lucas, P. W., Leggett, S. K., Tinney, C. G., Day-Jones, A. C., and et al. (2011). Blue not brown: UKIRT Infrared Deep Sky Survey T dwarfs with suppressed K-band flux. MNRAS, pages 376–+.

Nissen, P. E. (1999). Age and Metallicity Distributions among Galactic Disk Stars. Ap&SS, **267**, 119–128.

Oscoz, A., Rebolo, R., López, R., Pérez-Garrido, A., Pérez, J. A., Hildebrandt, S., Rodríguez, L. F., and et al. (2008). FastCam: a new lucky imaging instrument for medium-sized telescopes. In *Society of Photo-Optical Instrumentation Engineers (SPIE) Conference Series*, volume 7014 of *Society of Photo-Optical Instrumentation Engineers (SPIE) Conference Series*.

Ostriker, J. P. and Peebles, P. J. E. (1973). A Numerical Study of the Stability of Flattened Galaxies: or, can Cold Galaxies Survive? ApJ, **186**, 467–480.

Padoan, P. and Nordlund, Å. (2002). The Stellar Initial Mass Function from Turbulent Fragmentation. ApJ, **576**, 870–879.

Pauli, E.-M., Napiwotzki, R., Heber, U., Altmann, M., and Odenkirchen, M. (2006). 3D kinematics of white dwarfs from the SPY project. II. A&A, **447**, 173–184.

Perryman, M. A. C., Lindegren, L., Kovalevsky, J., Hoeg, E., Bastian, U., Bernacca, P. L., Crézé, M., and et al (1997). The HIPPARCOS Catalogue. A&A, **323**, L49–L52.

Pinfield, D. J., Burningham, B., Tamura, M., Leggett, S. K., Lodieu, N., Lucas, P. W., Mortlock, D. J., and et al. (2008). Fifteen new T dwarfs discovered in the UKIDSS Large Area Survey. MNRAS, **390**, 304–322.

Pinfield, D. J., Burningham, B., Lodieu, N., Leggett, S. K., Tinney, C. G., van Spaandonk, L., Marocco, F., and et al. (2012). Discovery of the benchmark metal poor T8 dwarf BD+01 2920B. *ArXiv e-prints*.

Reggiani, M. M. and Meyer, M. R. (2011). Binary Formation Mechanisms: Constraints from the Companion Mass Ratio Distribution. ApJ, **738**, 60.

Reid, I. N. and Hawley, S. L. (2005). *New light on dark stars : red dwarfs, low-mass stars, brown dwarfs*.

Reid, I. N., Kirkpatrick, J. D., Liebert, J., Burrows, A., Gizis, J. E., Burgasser, A., Dahn, C. C., Monet, D., Cutri, R., Beichman, C. A., and Skrutskie, M. (1999). L Dwarfs and the Substellar Mass Function. ApJ, **521**, 613–629.

Reid, I. N., Sahu, K. C., and Hawley, S. L. (2001). High-Velocity White Dwarfs: Thick Disk, Not Dark Matter. ApJ, **559**, 942–947.

Reid, I. N., Gizis, J. E., and Hawley, S. L. (2002). The Palomar/MSU Nearby Star Spectroscopic Survey. IV. The Luminosity Function in the Solar Neighborhood and M Dwarf Kinematics. AJ, **124**, 2721–2738.

Reipurth, B. and Clarke, C. (2001). The Formation of Brown Dwarfs as Ejected Stellar Embryos. AJ, **122**, 432–439.

Robin, A. C., Haywood, M., Creze, M., Ojha, D. K., and Bienayme, O. (1996). The thick disc of the Galaxy: sequel of a merging event. A&A, **305**, 125.

Robin, A. C., Reylé, C., Derrière, S., and Picaud, S. (2003). A synthetic view on structure and evolution of the Milky Way. A&A, **409**, 523–540.

Robin, A. C., Reylé, C., Derrière, S., and Picaud, S. (2004). Erratum: A synthetic view on structure and evolution of the Milky Way. A&A, **416**, 157.

Roche, P. F., Lucas, P. W., Mackay, C. D., Ettedgui-Atad, E., Hastings, P. R., Bridger, A., Rees, N. P., and et al (2003). UFTI: the 0.8 - 2.5 μm fast track imager for the UK infrared telescope. In M. Iye & A. F. M. Moorwood, editor, *Society of Photo-Optical Instrumentation Engineers (SPIE) Conference Series*, volume 4841 of *Society of Photo-Optical Instrumentation Engineers (SPIE) Conference Series*, pages 901–912.

Rubin, V. C., Thonnard, N., and Ford, Jr., W. K. (1978). Extended rotation curves of high-luminosity spiral galaxies. IV - Systematic dynamical properties, SA through SC. ApJ, **225**, L107–L111.

Salpeter, E. E. (1955). The Luminosity Function and Stellar Evolution. ApJ, **121**, 161.

Sandage, A. (1957). Observational Approach to Evolution. I. Luminosity Functions. ApJ, **125**, 422.

Santos, N. C., Israelian, G., and Mayor, M. (2004). Spectroscopic [Fe/H] for 98 extra-solar planet-host stars. Exploring the probability of planet formation. A&A, **415**, 1153–1166.

Saumon, D. and Marley, M. S. (2008). The Evolution of L and T Dwarfs in Color-Magnitude Diagrams. ApJ, **689**, 1327–1344.

Saumon, D., Bergeron, P., Lunine, J. I., Hubbard, W. B., and Burrows, A. (1994). Cool zero-metallicity stellar atmospheres. ApJ, **424**, 333–344.

Schmidt, M. (1959). The Rate of Star Formation. ApJ, **129**, 243.

Scholz, R. (2010a). Hip 63510C, Hip 73786B, and nine new isolated high proper motion T dwarf candidates from UKIDSS DR6 and SDSS DR7. A&A, **515**, A92+.

Scholz, R. (2010b). ULAS J141623.94+134836.3 - a faint common proper motion companion of a nearby L dwarf. Serendipitous discovery of a cool brown dwarf in UKIDSS DR6. A&A, **510**, L8+.

Schwarzschild, M. (1958). *Structure and evolution of the stars.*

Simcoe, R. A., Burgasser, A. J., Bernstein, R. A., Bigelow, B. C., Fishner, J., Forrest, W. J., McMurtry, C., and et al. (2008). FIRE: a near-infrared cross-dispersed echellette spectrometer for the Magellan telescopes. In *Society of Photo-Optical Instrumentation Engineers (SPIE) Conference Series*, volume 7014 of *Society of Photo-Optical Instrumentation Engineers (SPIE) Conference Series*.

Smart, R. L., Jones, H. R. A., Lattanzi, M. G., Leggett, S. K., Warren, S. J., Adamson, A. J., Burningham, B., and et al. (2010). The distance to the cool T9 brown dwarf ULAS J003402.77-005206.7. A&A, **511**, A30.

Smith, L., Lucas, P., Burningham, B., Jones, H., Smart, R., Pinfield, D., Marocco, F., and Clarke, J. (2013). The Kinematic Age of the Coolest T Dwarfs. *ArXiv e-prints*.

Soubiran, C., Bienaymé, O., Mishenina, T. V., and Kovtyukh, V. V. (2008). Vertical distribution of Galactic disk stars. IV. AMR and AVR from clump giants. A&A, **480**, 91–101.

Stamatellos, D. (2013). The formation of low-mass stars and brown dwarfs. *ArXiv e-prints*.

Stamatellos, D., Maury, A., Whitworth, A., and André, P. (2011). The lower limits of disc fragmentation and the prospects for observing fragmenting discs. MNRAS, **413**, 1787–1796.

Stephens, D. C., Leggett, S. K., Cushing, M. C., Marley, M. S., Saumon, D., Geballe, T. R., Golimowski, D. A., and et al. (2009). The 0.8-14.5 μm Spectra of Mid-L to Mid-T Dwarfs: Diagnostics of Effective Temperature, Grain Sedimentation, Gas Transport, and Surface Gravity. ApJ, **702**, 154–170.

Strauss, M. A., Fan, X., Gunn, J. E., Leggett, S. K., Geballe, T. R., Pier, J. R., Lupton, R. H., and et al. (1999). The Discovery of a Field Methane Dwarf from Sloan Digital Sky Survey Commissioning Data. ApJ, **522**, L61–L64.

Tarter, J. C. (1975). *The interaction of gas and galaxies within galaxy clusters*. Ph.D. thesis, California Univ., Berkeley.

Tinney, C. G., Burgasser, A. J., Kirkpatrick, J. D., and McElwain, M. W. (2005). The 2MASS Wide-Field T Dwarf Search. IV. Hunting Out T Dwarfs with Methane Imaging. AJ, **130**, 2326–2346.

Tody, D. (1986). The IRAF Data Reduction and Analysis System. In D. L. Crawford, editor, *Society of Photo-Optical Instrumentation Engineers (SPIE) Conference Series*, volume 627 of *Society of Photo-Optical Instrumentation Engineers (SPIE) Conference Series*, pages 733–+.

Tokunaga, A. T., Kobayashi, N., Bell, J., Ching, G. K., Hodapp, K.-W., Hora, J. L., Neill, D., Onaka, P. M., Rayner, J. T., Robertson, L., Warren, D. W., Weber, M., and Young, T. T. (1998). Infrared camera and spectrograph for the SUBARU Telescope. In A. M. Fowler, editor, *Society of Photo-Optical Instrumentation Engineers (SPIE) Conference Series*, volume 3354 of *Society of Photo-Optical Instrumentation Engineers (SPIE) Conference Series*, pages 512–524.

Tokunaga, A. T., Simons, D. A., and Vacca, W. D. (2002). The Mauna Kea Observatories Near-Infrared Filter Set. II. Specifications for a New JHKL'M' Filter Set for Infrared Astronomy. PASP, **114**, 180–186.

Tsvetanov, Z. I., Golimowski, D. A., Zheng, W., Geballe, T. R., Leggett, S. K., Ford, H. C., Davidsen, A. F., and et al. (2000). The Discovery of a Second Field Methane Brown Dwarf from Sloan Digital Sky Survey Commissioning Data. ApJ, **531**, L61–L65.

Vacca, W. D., Cushing, M. C., and Rayner, J. T. (2003). A Method of Correcting Near-Infrared Spectra for Telluric Absorption. PASP, **115**, 389–409.

Warren, S. J., Mortlock, D. J., Leggett, S. K., Pinfield, D. J., Homeier, D., Dye, S., Jameson, R. F., and et al. (2007). A very cool brown dwarf in UKIDSS DR1. MNRAS, **381**, 1400–1412.

Weis, E. W. (1993). Photometry of dwarf K and M stars. AJ, **105**, 1962–1966.

Whitworth, A. P. and Zinnecker, H. (2004). The formation of free-floating brown dwarves and planetary-mass objects by photo-erosion of prestellar cores. A&A, **427**, 299–306.

Wielen, R., Jahreiss, H., and Kruger, R. (1983). The Determination of the Luminosity Function of Nearby Stars. In A. G. D. Philip and A. R. Upgren, editors, *IAU Colloq. 76: Nearby Stars and the Stellar Luminosity Function*, pages 163–170.

Wright, E. L., Eisenhardt, P. R. M., Mainzer, A. K., Ressler, M. E., Cutri, R. M., Jarrett, T., Kirkpatrick, J. D., and et al. (2010). The Wide-field Infrared Survey Explorer (WISE): Mission Description and Initial On-orbit Performance. AJ, **140**, 1868–1881.

York, D. G., Adelman, J., Anderson, Jr., J. E., Anderson, S. F., Annis, J., Bahcall, N. A., and et al. (2000). The Sloan Digital Sky Survey: Technical Summary. AJ, **120**, 1579–1587.

Zhang, Z. H., Pokorny, R. S., Jones, H. R. A., Pinfield, D. J., Chen, P. S., Han, Z., Chen, D., and et al. (2009). Ultra-cool dwarfs: new discoveries, proper motions, and improved spectral typing from SDSS and 2MASS photometric colors. A&A, **497**, 619–633.

Zhang, Z. H., Pinfield, D. J., Burningham, B., Jones, H. R. A., Day-Jones, A. C., Marocco, F., Gomes, J., and Galvez-Ortiz, M. C. (2013). Purple dwarfs: New L subdwarfs from UKIDSS and SDSS. In *European Physical Journal Web of Conferences*, volume 47 of *European Physical Journal Web of Conferences*, page 6007.